Aalto University
School of Engineering

CHALMERS
UNIVERSITY OF TECHNOLOGY

Nordic Master Programme in Maritime Engineering

Investigation of ship vulnerability to SGISC based failure modes in different sea areas

Umair Khalid

Master's Thesis
2025

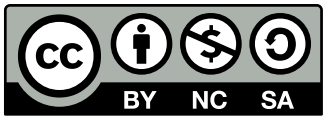

Aalto University
School of Engineering

CHALMERS
UNIVERSITY OF TECHNOLOGY

Author Umair Khalid

Title Investigation of ship vulnerability to SGISC based failure modes in different sea areas

Degree programme Maritime Engineering

Major Ship Design

Supervisors Martin Schreuder, Teemu Manderbacka

Advisors Pekka Ruponen, Daniel Lindroth

Collaborative partner NAPA

Date 17 June 2025 **Number of pages** 98 **Language** English

Abstract

This thesis investigates the vulnerability of ships to dynamic stability failure, as defined by the Second Generation Intact Stability Criteria (SGISC). The study addresses a key limitation of SGISC, which uses a standard wave scatter table based on North Atlantic data. This study aims to investigate the effect of different sea areas on the applicability of SGISC by using modern hindcast wave data. The studied sea zones are selected based on high-traffic global shipping routes for cargo and ro-ro passenger (ropax) vessels and are aligned with zones defined in the Global Wave Statistics (GWS) database. Level 2 vulnerability assessments are performed for three of the five stability failure modes within the SGISC: pure loss of stability, parametric rolling, and excessive acceleration. Four sample ships representing a large and small container ship, a bulk carrier, and a ropax vessel are studied under multiple loading conditions and wave environments using NAPA software.

The vulnerability analysis of all failure modes and sample ships revealed that the standard wave scatter table consistently gave higher vulnerability index values than the other zones studied. Based on the results, it is concluded that the standard wave scatter table (Rev.1) is suitable to use as a wave environment input for approving ships for unrestricted operations. Among all sea areas, the Pacific Ocean zones experienced the highest vulnerability to cargo ships, whereas Ropax vessels showed the highest vulnerability in the European sea areas. When comparing all sample ships, the fine-hull ropax vessel is most vulnerable to parametric rolling and pure loss of stability, whereas the bulk carrier is most susceptible to excessive acceleration due to its fuller hull form.

Keywords Ship stability, Intact Stability, SGISC, Failure modes, Wave scatter table, Vulnerability analysis

Preface

This thesis is submitted as part of the Nordic Master's Programme in Maritime Engineering at Aalto University and Chalmers University of Technology.

I am grateful to Teemu Manderbacka at Aalto University, Martin Schreuder at Chalmers, and Pekka Ruponen and Daniel Lindroth at NAPA for their valuable guidance and support throughout this work. Their expertise and answers to my questions helped me solve technical challenges, work efficiently with large datasets, and improve the quality of my thesis.

I would also like to thank Aalto University and Chalmers University of Technology for providing an excellent learning environment and practical opportunities in naval architecture and ship design. My studies at these universities have provided me useful skills and a solid foundation for my future career.

Finally, I would like to thank my wife, Tooba Imtiaz, my parents, and my loving child for their constant encouragement and support. Tooba's motivation and patience were especially important to me during this journey.

I hope this thesis contributes to safer and more efficient ship design, and inspires others working in this field.

Otaniemi, 17 June 2025

Umair Khalid

Contents

Symbols and abbreviations

Symbols

A_k	Bilge keel area
A_{WL}	Waterplane area
AP	Aft perpendicular
B	Breadth of ship
C	Roll period coefficient
C_B	Block coefficient
C_{WP}	Waterplane area coefficient
C_i	Long-term vulnerability index
C_m	Midship coefficient
C_S	Short-term vulnerability index
CR_1, CR_2	Intermediate vulnerability criteria (level 2)
d	Draft
D	Depth
Fn	Froude number
g	Acceleration due to gravity [m/s^2]
GM	Metacentric height
GM_t	Transverse metacentric height [m]
GZ	Righting lever
$H_{r,i}$	Representative wave height
H_s	Significant wave height
h_r	Vertical position above roll axis [m]
K_i	Speed scaling factor
KMT	Transverse metacentric height
L_{BP}	Length between perpendiculars [m]
L_{OA}	Overall length
m_0	Zeroth-order spectral moment [m^2·s]
N	Number of sea states
R_{EA2}	Excessive acceleration Threshold
R_{PLO}	Pure loss of stability threshold
R_{PR2}	Parametric Rolling threshold
$S_{zz}(\omega)$	Wave spectrum
T	Draft [m]
T_e	Wave enounter period
T_m	Mean wave period
T_r	Natural roll period
T_z	Zero-crossing wave period
Tr	Trim
V	Ship speed
V_s	Design speed
W_i	Weighting factor from wave scatter table
x	Longitudinal location (from AP or aft perpendicular)

z	Vertical location (keel/crew area)
β	Ship heading
Δ	Displacement
η	Wave elevation
λ	Wavelength
ϕ	Roll angle
ϕ_{max}	Maximum roll angle
ϕ_V	Angle of vanishing stability
ϕ_{SW}	Static heel angle under heeling lever
$\sigma_{LA,i}$	Std. dev. of lateral acceleration
ω	Angular frequency

Abbreviations

AHL	Alternate Hold Loading
AIS	Automatic Identification System
AP	Aft Perpendicular
BMT	British Maritime Technology
DSA	Direct Stability Assessment
DSC	Dead Ship Condition
DTC	Duisburg Test Case
EA	Excessive Acceleration
GM	Metacentric Height
GWS	Global Wave Statistics
GZ	Righting Lever
IACS	International Association of Classification Societies
IMO	International Maritime Organization
IS Code	Intact Stability Code
LC	Loading Condition
MSC	Maritime Safety Committee
OG	Operational Guidance
OL	Operational Limitation
PLS	Pure Loss of Stability
PR	Parametric Rolling
RoPax	Roll-on/Roll-off Passenger (ship)
SGISC	Second Generation Intact Stability Criteria
SR/BR	Surf-riding / Broaching
WST	Wave Scatter Table

1 Introduction

1.1 Background

Intact stability is a fundamental requirement for ships that ensures their safety from capsizing and maintaining an upright equilibrium at sea. It is an important factor in the design and safety assessment of ships that contributes to defining the design parameters and operational limitations. Historically, the evaluation of ship stability can be traced back to the work of Archimedes and development of metacentric and righting moment theories by Bouguer and Euler, respectively, in the 18th century[1]. However, the foundation of modern intact stability criteria began with the work of Rahola in the 1930s, who proposed the first intact stability criteria to ensure safety of ships at sea [2]. His work led to the introduction of the first international intact stability guidelines (IMO Res. A.167, 1968), which later formed the basis for the current intact stability criteria (IS Code 2008) [3].

Intact stability criteria, which are based on static ship assumptions, have been proven inadequate for capturing the vulnerability to dynamic stability failures encountered in actual sea states. [4]. The occurrence of dynamic failures is linked to complex interactions between ships and waves, especially under specific operating conditions [5]. The vulnerability of ships to dynamic stability failures has long been recognized as a critical issue in evaluating ship safety under realistic wave conditions and researchers have recognized the need to better understand the dynamic stability of ships[6]. This became increasingly important as ships grew larger and operating in harsher sea conditions, highlighting the shortcomings of conventional static stability methods.

In the 1970s, Paulling et al. [7] experimentally investigated ships in heavy seas and distinguished three different dynamic stability failures.Their experimental study revealed that pure loss of stability and parametric rolling occurred in following and quartering seas. They also recommended the use of statistical wave data to predict the probability of such events, emphasizing the need for probabilistic approaches for stability assessment. Chou et al.[8] investigated ship motions in extreme waves, and the capsizing phenomenon was revealed by changes in the waterplane areas in the waves. Despite the early insights, the existing intact stability code [9] at the time remained based on simple semi-empirical static assumptions and lacked the capability to evaluate dynamic stability under realistic sea conditions. In 2000, Spyrou and Papanikolaou proposed a two-level framework for a quantitative assessment of dynamic stability failures.[10]

Despite compliance with intact stability regulations, several ships experienced capsizing or faced significant losses due to dynamic stability failures under operational sea conditions during the late 20th and early 21st centuries [11][12][13]. Notable incidents, such as 59m long Oil tanker EDITH TEKROL in the Baltic Sea (1975), 4832-TEU container vessel APL China in the North Pacific (1998), 4324-TEU container vessel Maersk Carolina in the Northern Atlantic (2003), and pure car carrier vessel Cougar Ace in the North Pacific (2006) have resulted in significant loss of cargo, vessel

damage, and in some cases, loss of life. Such real-world incidents highlighted the gaps in the existing stability criteria and drew the attention of regulatory bodies and ship designers to the importance of addressing dynamic stability under realistic sea conditions.

In 2001, IMO initiated a comprehensive revision of the Intact Stability Code (IMO Res. A.749) [3]. This process led to the development of the Intact Stability (IS) Code 2008[14]. This restructured the existing framework and addressed the limitation of the weather criterion[15]. However, the weather criterion alone is no longer sufficient to fully account for the complex dynamic phenomenon arising from wave-hull interactions because it is based on semi-empirical methods [3]. In its mandatory section Part A, Section 1.2, the code highlighted that some ships may face greater risk in waves due to dynamic phenomena such as large roll angles or accelerations. The IMO also recognized the need to develop new criteria to evaluate the dynamic stability failures in sea waves[14]. Consequently, the IMO began the development of new intact stability criteria to evaluate dynamic stability using performance-based and probabilistic methods[16] [17]. Five failure modes were identified and assessed individually through a multilevel assessment structure [18]:

1. **Dead Ship Condition:** Uncontrolled roll due to combined wind and wave action in beam seas after loss of propulsion.
2. **Excessive Accelerations:** Rapid roll-induced lateral accelerations causing large inertial forces.
3. **Pure Loss of Stability:** Significant reduction in righting lever due to waterplane changes when crest aligns with midship in long following waves.
4. **Parametric Rolling:** Resonant roll motion triggered by periodic variation of transverse stability as the ship moves through longitudinal waves.
5. **Surf-Riding and Broaching:** Transition from wave-induced acceleration to loss of steering control, leading to violent yaw and large heel angles.

During the development of the SGISC, the IMO issued multiple draft versions of the criteria with methodologies for vulnerability assessment. To support their refinement, the IMO actively encouraged member states, classification societies, and researchers to perform test applications and submit feedback. Numerous studies have analyzed different ship types and failure modes, which helped to validate and improve the proposed criteria[17]. A number of test applications for multiple ship types were submitted during the development phase, evaluating the effectiveness of the Level 1 and Level 2 criteria and providing feedback to the IMO [17][19]. For example, Tompuri et al.[20] applied the draft SGISC regulations to a fast RoPax ship and highlighted the sensitivity of Level 2 results to key design inputs and guidance to operational limitation. Chung et al. [21] applied the draft SGISC to evaluate pure loss of stability and parametric rolling and found many Korean built container ships failed to meet the vulnerability criteria in case of parametric rolling. In one study, the SGISC vulnerability criteria were comprehensively evaluated using a sample of 17

ships, and the consistency between Level 1 and Level 2 assessments across all studied failure modes was found [22]. A similar study examined the consistency between Level 1 and Level 2 vulnerability criteria for three SGISC failure modes and proposed recommendations to avoid inconsistencies between the levels [23].

After years of development, the IMO released the Interim Guidelines for the Second Generation Intact Stability Criteria in 2020 (MSC.1/Circ.1627)[24]. Although the SGISC is not yet mandatory, ship designers are recommended to apply these guidelines in addition to the mandatory IS code for the safety of ships with respect to dynamic stability failure modes. The SGISC evaluation follows a multilevel assessment structure with three levels of vulnerability checks and a final step for operational measures, if needed.

- **Level 1** is the simplest and most conservative check. It uses basic formulas similar to traditional intact stability criteria. If passed, no further checks are required.
- **Level 2** applies physics-based methods and wave scatter data to assess vulnerability more accurately. Failure at this level indicates possible risks under realistic sea conditions.
- **Direct Stability Assessment (DSA)** is the most advanced level, using computational simulations or physical model tests to evaluate stability. It is time-consuming and costly but provides the most accurate results.
- If a ship fails any level, **Operational Measures** can be applied:
  - **Operational Limitations (OL)**: Restrictions on the environmental conditions in which the ship is allowed to operate, such as wave height, sea area, or season.
  - **Operational Guidance (OG)**: provides ship operation instructions with combinations of ship speed, encounter heading, and environmental conditions like wave height, wave period, and wind to avoid in order to prevent dynamic failure.

Marlantes et al. [25] studied the technical and practical aspects of implementing the interim SGISC Guidelines. Their study involved developing and validating two different assessment methods, which were then applied to four sample ships to evaluate all failure modes under Level 1 and Level 2 criteria. Recent studies have applied the SGISC Level 2 vulnerability criteria to assess the risks of ship stability under global sea conditions. Hashimoto et al. evaluated vulnerability of parametric rolling across different zones based on global traffic density and seasonal variation[26]. Bulian and Orlandi investigated the impact of environmental data on the application of the SGISC, focusing on the Mediterranean Sea [27]. They applied Level 1 and Level 2 vulnerability criteria for parametric rolling to a Ropax vessel using five different sources of environmental data, including widely used Global Wave Statistics (GWS) data [28]. This study found that the use of different environmental data sources may result in considerable differences in vulnerability assessment results. The findings

showed that the GWS data resulted in more conservative results and required strict operational limits within the SGISC framework.

The SGISC methodology for level 2 checks specifies the use of a standard wave scatter table (WST) representing the environment of the North Atlantic,taken from the IACS Rec. 34 Rev.1, which is based on visual observations from the historical British Maritime Technology database[29]. However, in 2023, the IACS released Rev.2 of the recommendation, which is based on hindcast data [30]. Several comparative studies have shown significant differences between traditional BMT data and modern hindcast sources, with the latter providing more accurate representations of real sea conditions[31][32]. A recent study [33] examined the limitations of the standard WST used in SGISC vulnerability assessments and compared it with hindcast-derived wave data for selected sea areas. The study showed notably different results using two different datasets and recommended applying the SGISC guidelines using region-specific wave statistics instead of using standard WST. A comprehensive study by MARIN on container ship accidents from the late 1990s to 2020 revealed that most high-intensity container loss incidents occurred in the Pacific Ocean[34]. These findings highlight the importance of conducting vulnerability assessments using region-specific wave statistics rather than relying solely on standard WST. Applying the SGISC with zone-based environmental data allows to capture dynamic stability failure risks across different sea areas and ship routes.

1.2 Problem Statement

The Second Generation Intact Stability Criteria (SGISC) employ a standard wave scatter table (WST) to assess the vulnerability of dynamic stability. This WST represents the North Atlantic Ocean and is derived from the BMT (British Maritime Technology) wave statistics database, which is based on visual observations with the latest observation date back in 1984 [30]. Although this region represents one of the worst sea environments, it may not necessarily be the most extreme case when evaluating dynamic stability failure modes. Importantly, once a ship passes the SGISC vulnerability check using the standard WST, it is allowed to operate globally without restrictions. However, it remains unclear whether these vessels would remain non-vulnerable even if the SGISC passed the WST based on the North Atlantic [33]. Past incidents involving dynamic stability failures in regions such as the Pacific Ocean and Northern European Seas suggest that this unchecked global applicability of SGISC may overlook critical environmental risk. Thus, there is a strong need to study the effects of different wave scatter tables as inputs for the evaluation of dynamic stability failures using the SGISC guidelines.

In recent years, wave modeling has been significantly improved and multiple sources of wave hindcast data of global seas are available which represent the waves more accurately than the BMT data[31]. Using such data can improve the accuracy of SGISC results, especially when applied to global sea areas beyond the North Atlantic. To address these limitations, the current research focuses on the following:

1. Apply SGISC vulnerability criteria using hindcast wave scatter tables for different global sea areas.
2. Investigate how SGISC results vary across different operational zones compared to standard North Atlantic WST.
3. Compare the vulnerability trends across multiple ship types, as different hull forms and loading conditions may influence SGISC results even under the same wave environment.

1.3 Research Objective and Scope

The objective of this thesis is to assess ship vulnerability to SGISC-based dynamic stability failures under global sea environments, with a particular focus on studying how different sea areas affect the outcome of SGISC vulnerability results. The scope of this study includes the following:

- Vulnerability assessment of three different ship types according to SGISC interim guidelines: - Bulk carrier - Container ship - Roåax vessel
- Application of SGISC Level 2 vulnerability criteria for three failure modes: - Pure loss of stability (PLS) - Parametric rolling (PR) - Excessive acceleration (EA)
- Vulnerability assessment of each case in different sea areas based on actual shipping routes.
- Analysis of Level 2 vulnerability results to identify key factors (hull form,loading condition and environment data) and to understand how these factors affect the probability of failure modes.

1.4 Thesis Outline

This thesis is organized into five main chapters as follows:

- Chapter 1 introduces the background, problem statement, research objectives, and the scope of the study, emphasizing the motivation for evaluating ship stability under global sea environments using the SGISC guidelines.
- Chapter 2 provides an overview of the Second Generation Intact Stability Criteria (SGISC), explains the mechanisms of critical dynamic stability failures such as parametric rolling, pure loss of stability, and excessive acceleration and discusses relevant environmental factors
- Chapter 3 describes the selection of ship types, the sources of wave data, the sea area selection, the application of SGISC vulnerability assessment methods using NAPA software

- Chapter 4 presents the results of the vulnerability assessments, highlights observed trends across different ship types and sea environments and analyzes the key influencing factors.
- Chapter 5 summarizes the key findings of the research, draws conclusions based on the analyses, and suggests directions for future work.

An appendix is included (Appendix A), which presents the wave scatter diagrams for all studied zones.

2 Second Generation Intact Stability Criteria

2.1 Multi-Level Assessment

Figure 1 shows the schematic of the SGISC criteria application used to evaluate compliance for each stability failure mode. The assessment begins with the ship design parameters, loading condition, and enviromental data as input. Based on this information, the vulnerability to five defined dynamic stability failures is checked using a sequential process that progresses through three assessment levels, followed by an operational measures stage if needed.

Although the SGISC allows a ship to be assessed at any of the three levels directly, the recommended approach is to begin with Level 1 and move sequentially to higher levels only if necessary. All three levels are treated equally in terms of compliance, if the ship is found *not vulnerable* at Level 1, it is accepted, and no further analysis is required. This avoids unnecessary complex analysis for ships that clearly meet safety margins under simplified checks.

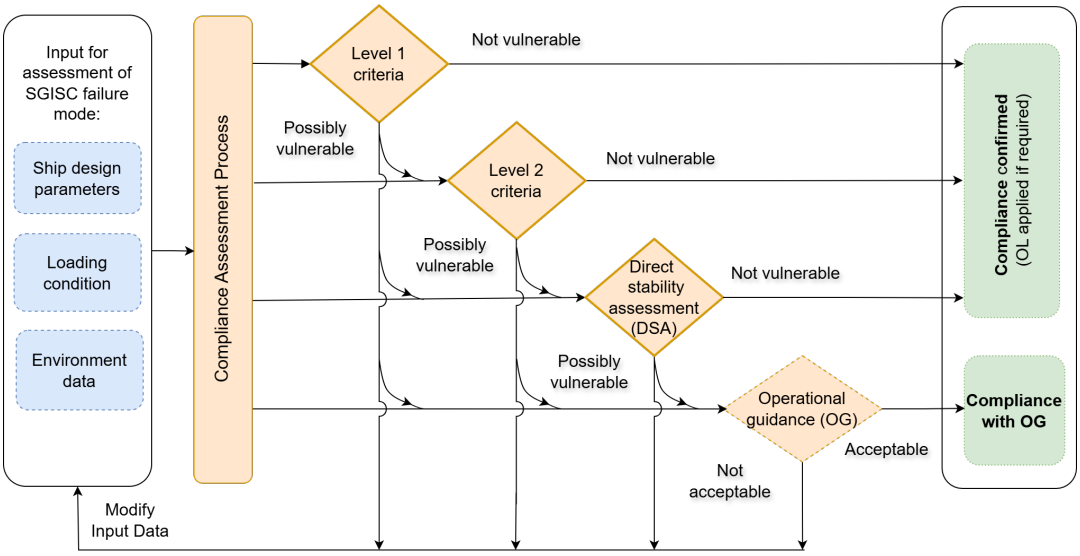

Figure 1: Schematic of the SGISC multi-level approach for vulnerability assessment [24]

Level 1: Simplified Vulnerability Criteria: Level 1 is the most basic and conservative check. It involves simple, formula-based calculations similar to those used in traditional intact stability rules. These criteria provide a quick estimation of vulnerability using limited inputs and assume large safety margins. Ships that pass Level 1 are considered safe under conventional sea conditions and no further checks are required.

Level 2: Physics-Based Vulnerability Criteria: If the ship is found *possibly vulnerable* at Level 1, it progresses to Level 2. This level applies physics-based methods and wave scatter data to assess vulnerability more accurately. Level 2 applies a probabilistic approach to calculate the likelihood of a dynamic stability failure, providing a better

reflection of real-world sea conditions. Although more accurate, it requires more data and computational effort than Level 1.

Direct Stability Assessment (DSA): If the ship still appears vulnerable after Level 2, then a DSA is performed. DSA is the most advanced method and involves numerical simulations of ship motions in waves, or experimental validation such as model testing. It aims to replicate realistic ship behavior under complex sea states and provides the most accurate results. However, it is also the most time-consuming and resource-intensive level.

Operational Measures: If the ship is found vulnerable even at DSA, it may still be accepted for operation by applying Operational Measures. These are divided into two types:

- **Operational Limitations (OL):** These restrict the environmental conditions under which the ship may operate. For example, OL may restrict sailing in specific sea areas, seasons, or wave height conditions where the ship did not meet the assessment. OL ensures compliance by avoiding the triggering conditions of vulnerability check failure.
- **Operational Guidance (OG):** This consists of ship-specific recommendations for safe navigation under different sea states. OG helps the ship master choose appropriate combinations of speed, heading, and other environment parameters(such as waves and wind) to reduce the risk of failure during voyages.

This multi-level approach ensures efficiency by prioritizing simpler checks first, reducing unnecessary complex analyses. If a ship fails any level, operational measures can still allow safe operation while maintaining compliance. This multi-tiered approach balances safety, practicality, and cost-effectiveness in modern ship stability assessments.

2.2 Stability Failure Modes in SGISC

2.2.1 Parametric Rolling

Physical Background

Parametric rolling is a complex resonant phenomenon that occurs due to periodic changes in the stability of a ship (righting moment) as she encounters waves. This type of failure typically develops in head or following seas. It is especially critical for ships with fine hull forms and large flares at the bow and stern, such as containerships and Ropax vessels. In these ship types, the waterplane area and consequently the stability varies significantly as waves pass along the hull.

The mechanism of parametric rolling depends on three primary conditions:

- **Wave Length:** The wavelength is approximately equal to the ship length, producing significant changes in the waterplane area as crests and troughs pass the hull.

- **Encounter Period:** The wave encounter period (T_e) is about half the natural roll period of the ship (T_r), creating a 2:1 resonance condition $T_e \approx \frac{1}{2}T_r$ (see Figure 3).
- **Roll Damping:** The ship's roll damping is sufficiently low; otherwise, the energy gained from the periodic stability variation will not be enough to amplify the roll motion.

As the vessel travels through head or following seas, periodic changes in stability occur due to the shifting position of wave crests and troughs along the hull. When a wave trough aligns with the midship section—where the hull is generally wall-sided—the flared bow and stern sections become more submerged, increasing the waterplane area and consequently the ship's stability. Conversely, when a wave crest passes amidships, the bow and stern are lifted, reducing the waterplane area and decreasing stability. This alternating variation in stability causes the righting moment to increase and decrease twice per roll cycle, potentially inducing roll amplification (see Figure 2). When a trough occurs as the ship is returning upright, it reinforces the motion by increasing the restoring moment. On the next half-cycle, a crest occurs as the ship is heeling, reducing stability and allowing a larger roll angle. If these events align consistently, the roll amplitude grows cycle-by-cycle. Without sufficient damping, this resonance can lead to dangerous roll angles exceeding 30° within a few cycles.

The risk of parametric rolling depends on the following critical factors:

- **Hull Form:** Ships with pronounced flare and fine underwater sections are more susceptible.
- **GM (Metacentric Height):** Lower GM means a smaller restoring moment, resulting in higher roll amplitudes and increased vulnerability to parametric rolling.
- **Damping Devices:** Bilge keels or anti-rolling tanks can mitigate parametric rolling by dissipating energy.
- **Speed and Wave Direction:** Parametric rolling typically occurs in head or following seas and becomes more likely at certain speeds that match the resonance condition. Adjusting course or speed can help to avoid resonance.

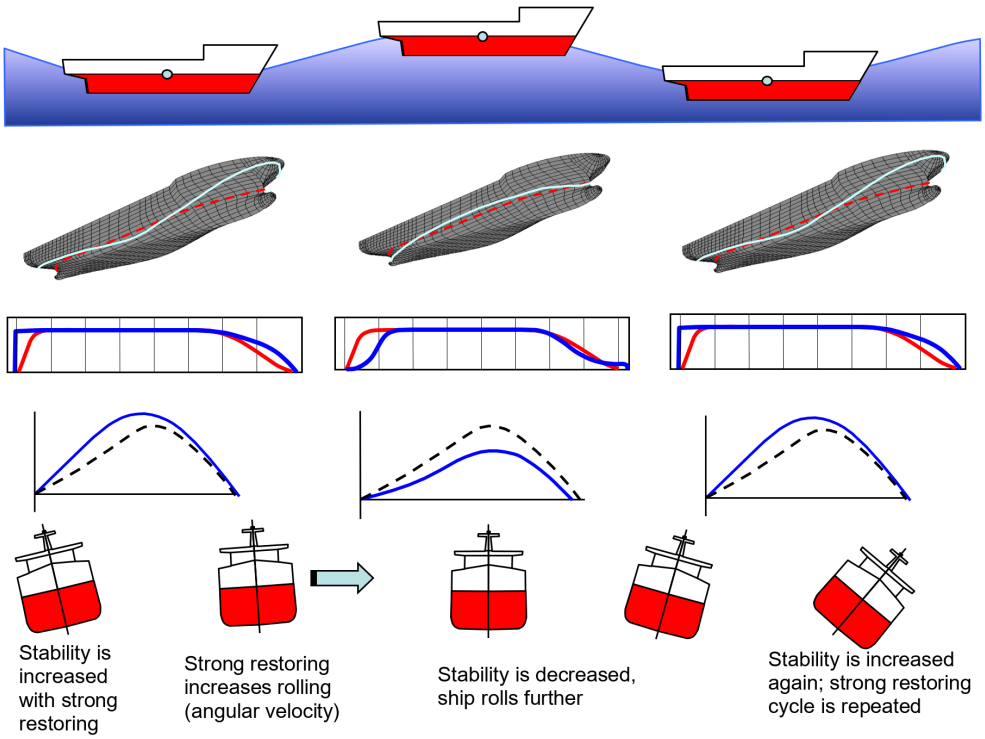

Figure 2: Illustration of the development of parametric rolling [35].

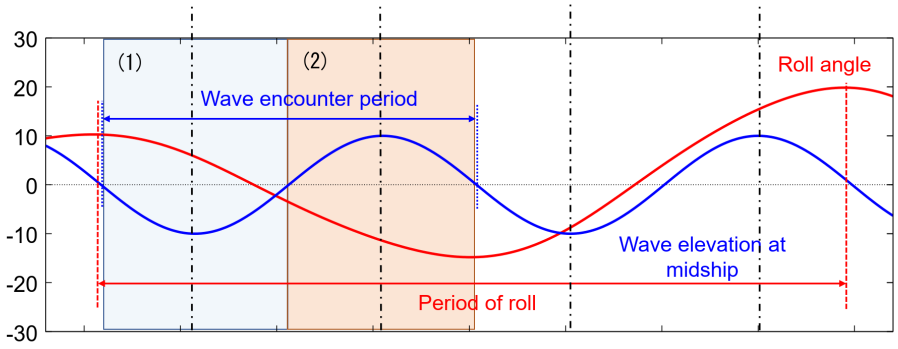

Figure 3: Relationship between the wave period and natural roll period of the ship during parametric rolling[36].

Level 2 Vulnerability Criteria

The Level 2 criterion for parametric roll is designed to estimate a ship long-term vulnerability to large roll angles in waves due to resonance caused by periodic changes in stability. The analysis considers various ship speeds, wave headings, and wave environments.

This study uses the Level 2 C2 check to assess vulnerability, and the procedure for calculating it is presented in the following paragraphs. According to the SGISC

guidelines, a ship is considered not vulnerable to parametric rolling under a given loading condition if the index value satisfies:

$$C2 \leq 0.025 \tag{1}$$

The evaluation is conducted in two main steps. Step 1 involves performing time-domain simulations to obtain the maximum roll angle under regular waves, while Step 2 applies wave scatter tables to estimate the probability of encountering excessive rolling.

The process follows the flowchart shown in Figure 4, which outlines the process step-by-step.

Step 1: Time-Domain Simulation and Preprocessing

For each heading $\beta \in \{\beta_h, \beta_f\}$ and each of the 12 Froude numbers Fn_i, the maximum roll angle $\varphi_{\max}$ is simulated in regular waves with varying wave heights. The wave height h_j is given by:

$$h_j = 0.01 \cdot j \cdot L, \quad \text{for } j = 0, 1, ..., 10 \tag{2}$$

The wavelength is taken as $\lambda = L$(Length of ship), and the simulation is carried out using a 1-degree-of-freedom (1-DOF) roll equation to calculate the maximum roll angle $\varphi_{\max}(Fn_i, h_j)$.

The Froude number for each speed V_i is defined as:

$$Fn_i = \frac{V_i}{\sqrt{gL}} \tag{3}$$

where V_i is obtained using a speed scaling factor K_i and design speed V_s :

$$V_i = V_s \cdot K_i \tag{4}$$

The speed factors K_i for the 12 speeds are:

Table 3: Values of K_i for different i

i	K_i
1	1.000
2	0.991
3	0.966
4	0.924
5	0.866
6	0.793
7	0.707
8	0.609
9	0.500
10	0.383
11	0.259
12	0.131

Step 2: Probabilistic Evaluation

The SGISC method simplifies irregular seas by using the representative wave height ($H_{r,i}$), which corresponds to the 1/3 largest effective wave height. The representative wave height $H_{r,i}$ for each sea state is calculated using Grim's effective wave approach. The calculation of $H_{r,i}$ is based on filtering the wave conditions to those within the ship's length, using H_s (significant wave height) and T_z (zero-crossing period) from the wave scatter table. A more detailed explanation of the Grim's effective wave method and its application within the SGISC framework is provided in the IMO explanatory notes on SGISC [35].

In the equation 8, it can be seen that $H_{r,i}$ mainly directly proportional to the significant wave height. As H_s increases, $H_{r,i}$ also increases, showing a strong dependence on H_s. Once the representative wave height ($H_{r,i}$) is determined for each sea state, the corresponding maximum roll angle is obtained by linear interpolation. Specifically, for each calculated $H_{r,i}$, the maximum roll angle is estimated by interpolating between the maximum roll angles computed at wave heights (h_j) in step-1.

$$H_{r,i} = 4.0043 \cdot \sqrt{m_0} \tag{5}$$

where m_0 is the zeroth-order spectral moment defined as:

$$m_0 = \int_{0.1\omega_L}^{3\omega_L} \left(\frac{\omega_L^2 \sin^2\left(\frac{\omega_L^2}{2g}\right)}{\pi^2 - \left(\frac{\omega_L^2}{2g}\right)^2} \right) S_{zz}(\omega)\, d\omega \tag{6}$$

and ω_L is defined as:

$$\omega_L = \sqrt{\frac{2\pi g}{L}} \tag{7}$$

The wave spectrum $S_{zz}(\omega)$ follows the Bretschneider wave spectrum as per SGISC guidelines:

$$S_{zz}(\omega) = \frac{H_s^2}{4\pi}\left(\frac{2\pi}{T_z}\right)^4 \omega^{-5} \exp\left[-\frac{1}{\pi}\left(\frac{2\pi}{T_z}\right)^4 \omega^{-4}\right] \tag{8}$$

If $H_{r,i} > 0.1L$, it is limited to:

$$H_{r,i} = 0.1L \tag{9}$$

For each Fn_i and wave heading, the expected roll angle is interpolated from the step-1 ($\varphi_{\max}$) using $H_{r,i}$. The short-term failure indicator $C_{S,j}$ is defined as:

$$C_{S,j} = \begin{cases} 1, & \text{if } \varphi_{H_{r,i}} > 25^\circ \\ 0, & \text{otherwise} \end{cases} \tag{10}$$

The weighted average of failures over sea states is calculated as:

$$C_2(Fn_i, \beta) = \sum_{j=1}^{N} W_j \cdot C_{S,j} \tag{11}$$

where W_j is weighting factor for the respective wave cases in the wave scatter table.

Finally, C2 is obtained by averaging over both headings and all speeds:

$$C2 = \left[\sum_{i=1}^{12} C_2(Fn_i, \beta_h) + \frac{1}{2}\left(C_2(0, \beta_h) + C_2(0, \beta_f)\right) + \sum_{i=1}^{12} C_2(Fn_i, \beta_f)\right] \Big/ 25 \tag{12}$$

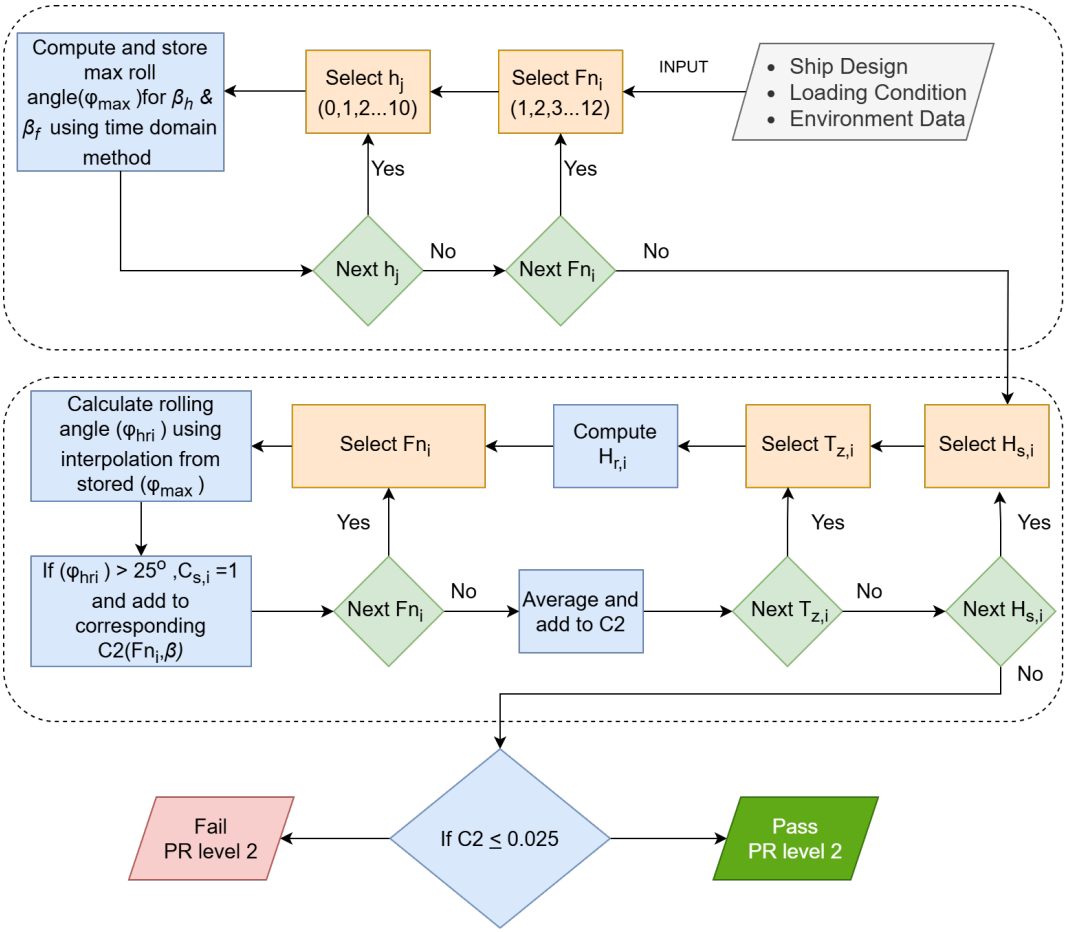

Figure 4: Flowchart for parametric rolling Level 2 Check 2 vulnerability criteria

2.2.2 Pure Loss of Stability

Physical Background

Pure loss of stability is a dangerous phenomenon where a ship experiences a sudden and significant reduction in stability due to wave-induced changes in the submerged hull shape. This occurs when the speed of ship is close to the wave celerity. When the wave crest stays longer at midship, it increases the risk of losing stability and makes the ship more vulnerable to capsizing.

When a wave crest is located close to the midship section, the narrow underwater parts of the bow and stern rise out of the water, which reduces the waterplane area (see Figure 5). Consequently, the metacentric height (GM) decreases, reducing the righting moment and increasing the risk of capsizing. This situation is considered the most critical for pure loss of stability.

The risk of pure loss of stability depends on the following critical factors:

- **Hull Form:** Ships with flared bow and stern (e.g., container ships) show larger GZ variation. Ships with more wall-sided hulls (e.g., tankers) are less affected.

- **Wave Length:** Risk is highest when the wave length is close to the ship's length.
- **Speed:** In following seas, if the speed of ship matches wave speed, the crest stays longer at midship, increasing the probability of pure loss of stability. It is important to note that this effect is not a concern for slow ships (Fn < 0.24), since the waves overtake the ship quickly and the condition of reduced stability at the wave crest does not persist long enough to cause failure.

In conclusion, the pure loss of stability arises from wave-induced changes in the submerged geometry of the ship. By understanding how wave crests and troughs alter the waterplane area and righting lever, naval architects and operators can identify the conditions that may lead to the loss of transverse stability and take preventive measures through design and operational choices.

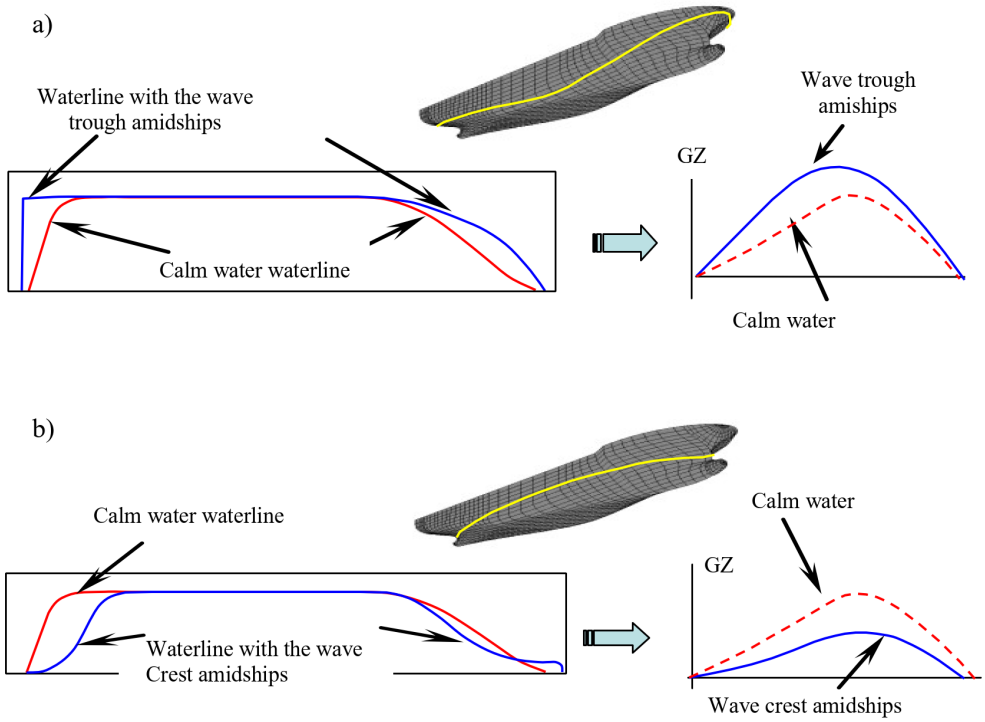

Figure 5: Ship stability variation due to waterplane changes with (a) a wave trough and (b) a wave crest located amidships. [22]

Level 2 Vulnerability Criteria

The following steps describe the Pure Loss Level 2 (PL2) assessment method for vulnerability evaluation under SGISC guidelines:

1. Prepare the ship input data including hull geometry, tank arrangement, loading conditions, and free surface moment effects.
2. Define the standardized set of wave heights h_i ranging from $0.01L$ to $0.1L$, where L is the ship length.

3. For each wave height h_i, assume wave length equal to ship length ($\lambda = L$).
4. For each h_i, simulate different wave crest positions along the ship from $0.4L$ aft to $0.5L$ forward of midships.
5. At each crest location, compute the quasi-static righting arm (GZ) curve.
6. From each GZ curve, determine and store the minimum angle of vanishing stability (φ_V) and the maximum angle of equilibrium (φ_{SW}) for each h_i. Both angles are illustrated in Figure 6.

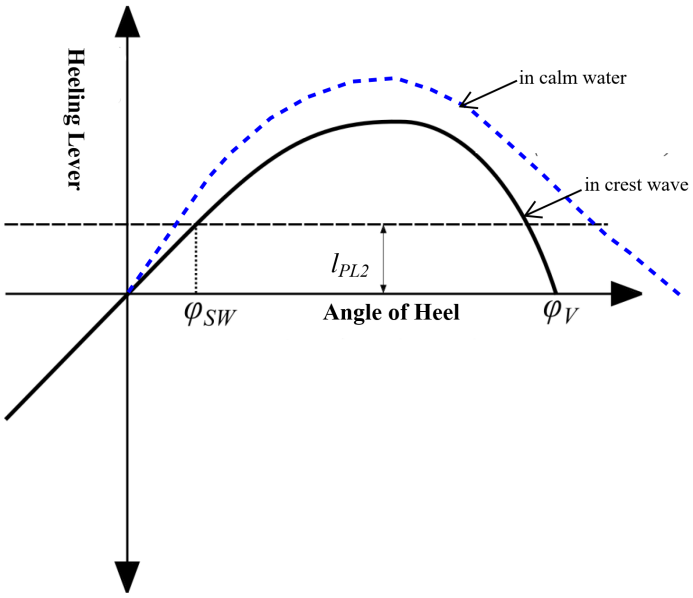

Figure 6: Pure loss of stability GZ curve characteristics used for Level 2 vulnerability assessment.

7. The angle of heel, φ_{SW}, is compued under the action of the heeling lever l_{PL2}, which is calculated as:

$$l_{PL2} = 8(H_i/\lambda)\, dFn^2 \quad , \tag{13}$$

where H_i is the effective wave height, λ is the wavelength, d is mean draft of ship and Fn is the difference in Froude number.

8. Construct curves of φ_V and φ_{SW} as functions of wave height h_i.
9. Obtain the environmental sea state data: significant wave heights $H_{s,j}$, zero-crossing periods $T_{z,j}$, and associated probabilities W_i.
10. For each sea state ($H_{s,j}$, $T_{z,j}$), compute the effective wave height H_i as the 3% highest wave height.
11. Using H_i, interpolate from the stored curves to find corresponding φ_V and φ_{SW}.

12. Evaluate Criterion 1 (C_{1i}) for each sea state:

$$C_{1i} = \begin{cases} 1, & \text{if } \varphi_V < 30^\circ \\ 0, & \text{otherwise} \end{cases}$$

13. Evaluate Criterion 2 (C_{2i}) for each sea state:

$$C_{2i} = \begin{cases} 1, & \text{if } \varphi_{SW} > 15^\circ \text{ for passenger ships or } 25^\circ \text{ for other ship types} \\ 0, & \text{otherwise} \end{cases}$$

14. Compute the vulnerability indices CR_1 and CR_2 by weighted summation over all sea states:

$$CR_1 = \sum_{i=1}^{N} W_i C_{1i} \tag{14}$$

$$CR_2 = \sum_{i=1}^{N} W_i C_{2i} \tag{15}$$

14. Compare the maximum of CR_1 and CR_2 to the threshold value 0.06:
    - If $\max(CR_1, CR_2) \leq 0.06$, the ship passes the PL2 criterion.
    - Otherwise, the ship fails the PL2 criterion.

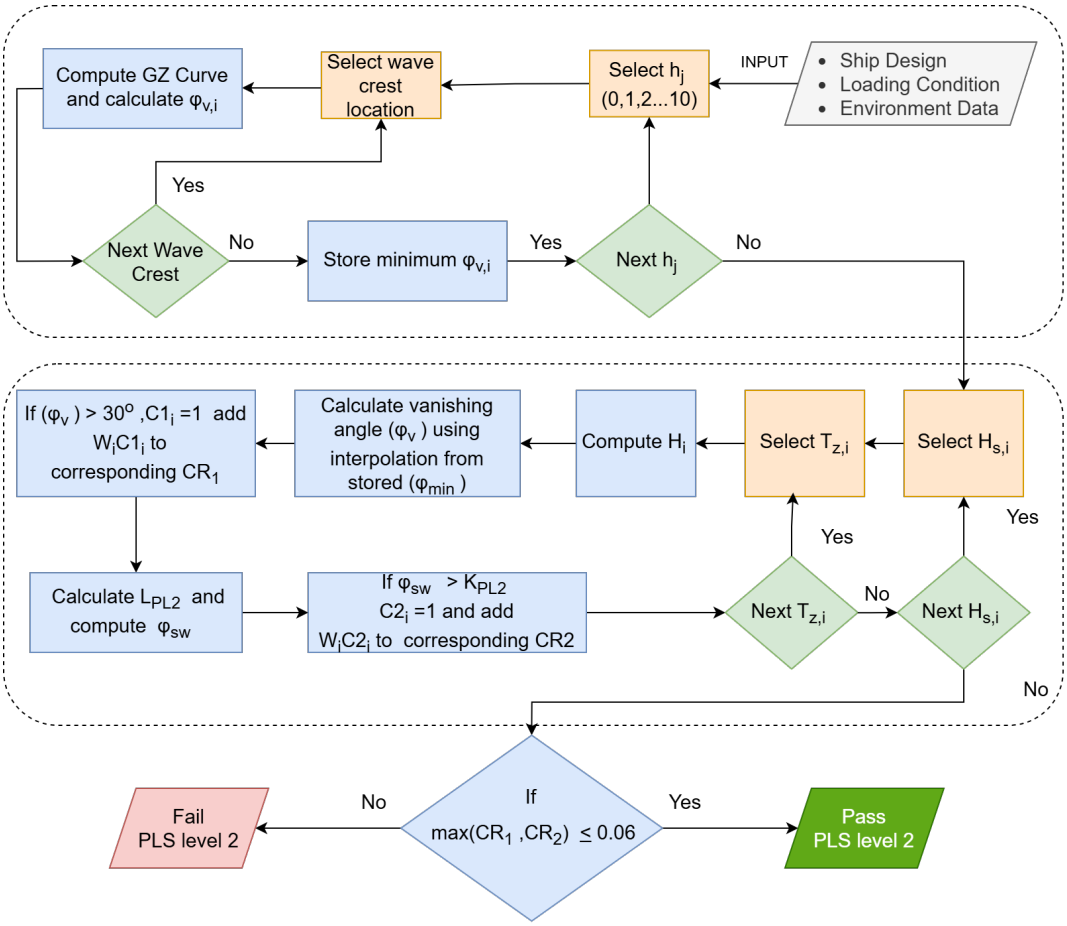

Figure 7: Flowchart for pure loss of stability Level 2 vulnerability criteria

2.2.3 Excessive Acceleration

Physical Background

Excessive acceleration is a stability failure that happens when people or objects on a ship are exposed to large inertial forces during roll motion. This mainly affects people located higher up in the ship because they travel a longer distance in the same amount of time, leading to higher speeds and stronger accelerations. As the ship rolls, the point farther from the roll axis must move faster to complete the motion in the same period (See Figure 8). This creates higher lateral accelerations at those points. When the metacentric height (GM) is low, the roll period becomes longer and accelerations are smaller. But with higher GM, the roll is faster and acceleration is greater, increasing the risk.

Inertial forces in the horizontal direction are more dangerous than vertical ones. They can make people lose balance, fall, or be thrown against furniture or bulkheads. This is especially important for the safety of crew and passengers in spaces like lounges, bridges, or upper decks. The effects of acceleration are commonly evaluated using indices like Motion Sickness Incidence (MSI) or Motion Induced Interruptions (MII),

which track the impact on comfort and safety. These are particularly relevant for passenger vessels like cruise ships or RoPax ferries.

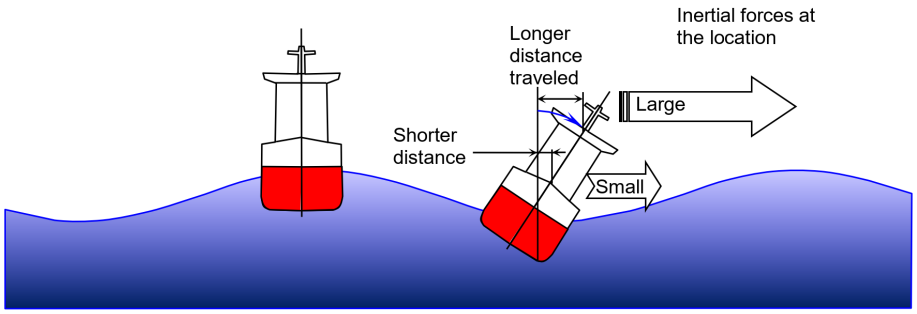

Figure 8: Illustration of ship stability failure due to excessive accelerations[35].

Level 2 Vulnerability Criteria

According to the SGISC guidelines, a ship is considered not vulnerable to excessive acceleration in a given loading condition if the long-term probability index C satisfies the following criterion:

$$C \leq R_{EA2} \tag{16}$$

where $R_{EA2} = 0.00039$ is the limiting value. The long-term index C is computed from the weighted sum of short-term probabilities over all sea states:

$$C = \sum_{i=1}^{N} W_i \cdot C_{S,i} \tag{17}$$

Here:

- N: number of short-term sea states,
- W_i: occurrence probability of sea state i (from wave scatter table),
- $C_{S,i}$: short-term failure index in sea state i.

The short-term failure index $C_{S,i}$ is defined as:

$$C_{S,i} = \exp\left(-\frac{R_2^2}{2\sigma_{LA,i}^2}\right) \tag{18}$$

where:

- $R_2 = 9.81\ \text{m/s}^2$: threshold lateral acceleration,

- $\sigma_{LA,i}$: standard deviation of lateral acceleration in sea state i.

The lateral acceleration variance is given by:

$$\sigma^2_{LA,i} = \frac{3}{4} \sum_{j=1}^{N_f} \left[a_y^2(\omega_j) \cdot S_{zz}(\omega_j) \cdot \Delta\omega \right] \tag{19}$$

with:

- ω_j: wave frequency,
- $\Delta\omega$: frequency interval,
- $S_{zz}(\omega_j)$: wave spectrum,
- $a_y(\omega_j)$: lateral acceleration RAO.

The lateral acceleration Response Amplitude Operator (RAO) is computed as:

$$a_y(\omega_j) = k_L \cdot \left(g + h_r \cdot \omega_j^2 \right) \cdot \varphi_a(\omega_j) \tag{20}$$

where:

- k_L: coupling factor,
- h_r: vertical position above roll axis,
- $\varphi_a(\omega_j)$: roll RAO amplitude.

The roll RAO is given by:

$$\varphi_a(\omega_j) = \left(\varphi_r(\omega_j)^2 + \varphi_i(\omega_j)^2 \right)^{0.5} \tag{21}$$

where φ_r and φ_i are the real and imaginary parts of the RAO, respectively.

The guidelines also offer a simplified method to compute $\varphi_a(\omega_j)$, based on the Froude–Krylov assumption and a linearized single-degree-of-freedom model, to estimate the real and imaginary components of roll response. The process follows the flowchart shown in Figure 9.

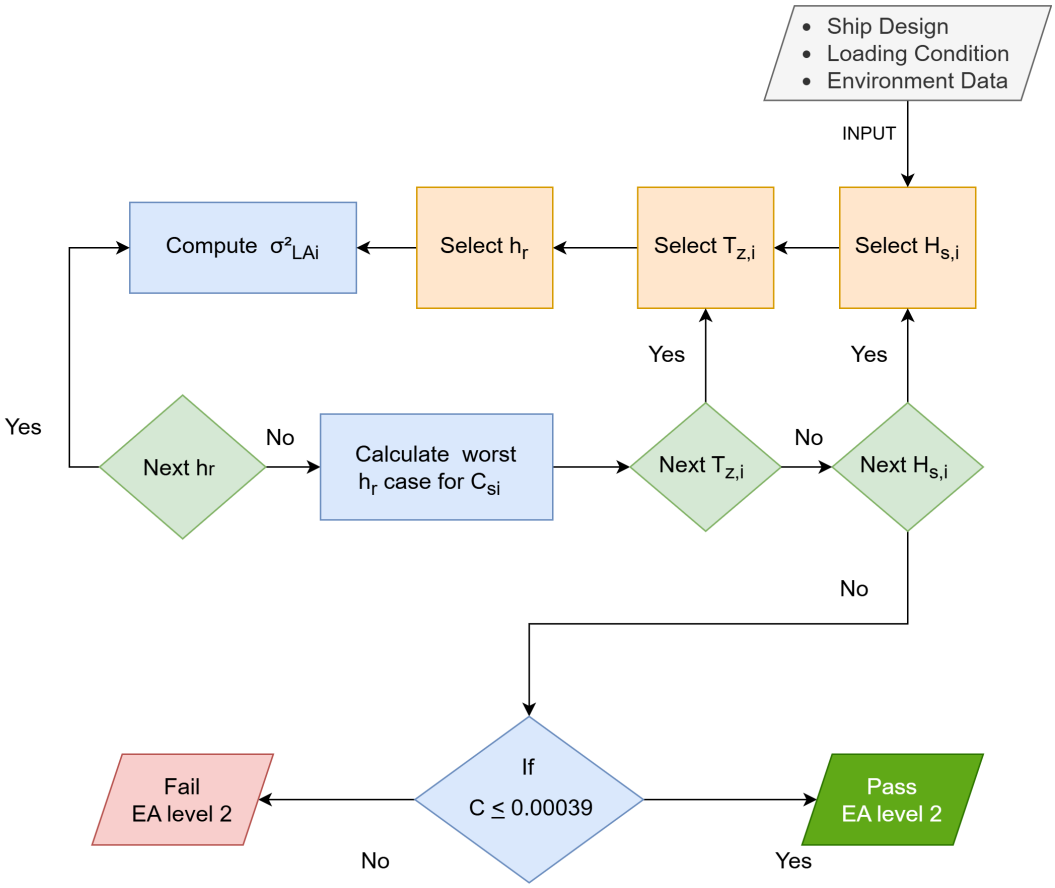

Figure 9: Flowchart for excessive acceleration Level 2 vulnerability criteria

2.3 Environmental Data

In the standard SGISC Interim Guidelines, the evaluation of ship vulnerability to dynamic failure modes makes use of a long-term environmental characterization based on a wave scatter table. This standard wave scatter table is adopted from IACS Recommendation No. 34/Rev.1[29], which defines the number of occurrences W_{ij} corresponding to each combination of significant wave height H_s and average zero-crossing wave period T_z, over 100,000 observations. Wave scatter data table describe the wave data of the North Atlantic, covering areas 8,9,15 and 16, as defined in Global Wave Statistics as shown in Figure 10 .

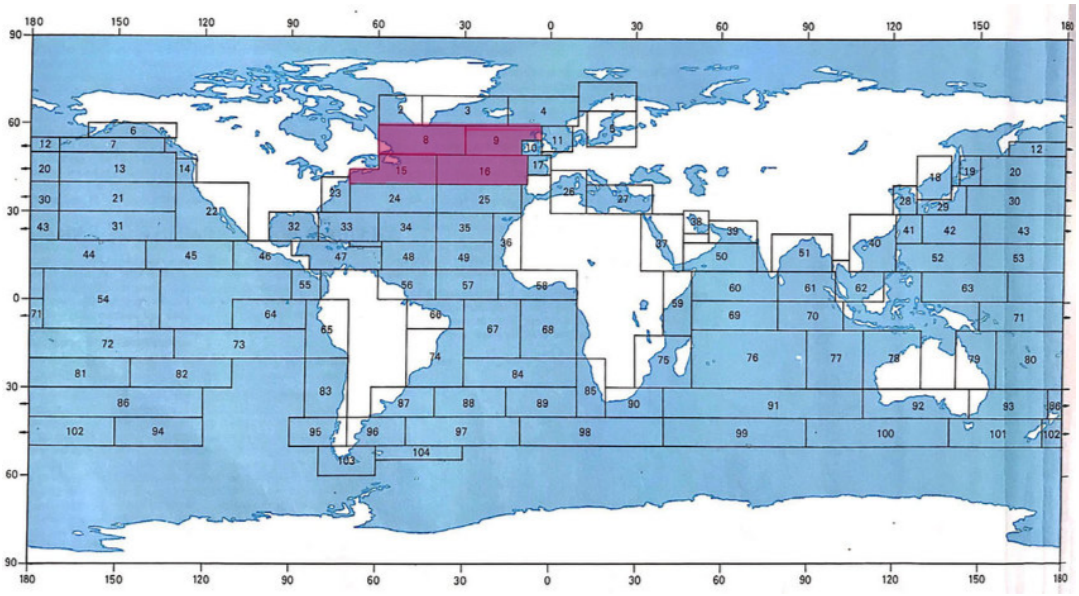

Figure 10: Global Wave Statistics zones map highlighting the North Atlantic zones [8,9,15,16] corresponding to IACS Recommendation No. 34 /Rev.1 [28].

The standard wave scatter table, presented in Table4, is recommended by SGISC to use for Level 2 vulnerability assessment of all failure modes.

Table 4: Wave scatter table IACS Rev.1[29]

Number of occurrences: 100 000 / T_z (s) = average zero-crossing wave period / H_s (m) = significant wave height																
$H_s \downarrow \backslash T_z \rightarrow$	3.5	4.5	5.5	6.5	7.5	8.5	9.5	10.5	11.5	12.5	13.5	14.5	15.5	16.5	17.5	18.5
0.5	1.3	133.7	865.6	1186.0	634.2	186.3	36.9	5.6	0.7	0.1	0.0	0.0	0.0	0.0	0.0	0.0
1.5	0.0	29.3	986.0	4976.0	7738.0	5569.7	2375.7	703.5	160.7	30.5	5.1	0.8	0.1	0.0	0.0	0.0
2.5	0.0	2.2	197.5	2158.8	6230.0	7449.5	4860.4	2066.0	644.5	160.2	33.7	6.3	1.1	0.2	0.0	0.0
3.5	0.0	0.2	34.9	695.5	3226.5	5675.0	5099.1	2838.0	1114.1	337.7	84.3	18.2	3.5	0.6	0.1	0.0
4.5	0.0	0.0	6.0	196.1	1354.3	3288.5	3857.5	2685.5	1275.2	455.1	130.9	31.9	6.9	1.3	0.2	0.0
5.5	0.0	0.0	1.0	51.0	498.4	1602.9	2372.7	2008.3	1126.0	463.6	150.9	41.0	9.7	2.1	0.4	0.1
6.5	0.0	0.0	0.2	12.6	167.0	690.3	1257.9	1268.6	825.9	386.8	140.8	42.2	10.9	2.5	0.5	0.1
7.5	0.0	0.0	0.0	3.0	52.1	270.1	594.4	703.2	524.9	276.7	111.7	36.7	10.2	2.5	0.6	0.1
8.5	0.0	0.0	0.0	0.7	15.4	97.9	255.9	350.6	296.9	174.6	77.6	27.7	8.4	2.2	0.5	0.1
9.5	0.0	0.0	0.0	0.2	4.3	33.2	101.9	159.9	152.2	99.2	48.3	18.7	6.1	1.7	0.4	0.1
10.5	0.0	0.0	0.0	0.0	1.2	10.7	37.9	67.5	71.7	51.5	27.3	11.4	4.0	1.2	0.3	0.1
11.5	0.0	0.0	0.0	0.0	0.3	3.3	13.3	26.6	31.4	24.7	14.2	6.4	2.4	0.7	0.2	0.1
12.5	0.0	0.0	0.0	0.0	0.1	1.0	4.4	9.9	12.8	11.0	6.8	3.3	1.3	0.4	0.1	0.0
13.5	0.0	0.0	0.0	0.0	0.0	0.3	1.4	3.5	5.0	4.6	3.1	1.6	0.7	0.2	0.1	0.0
14.5	0.0	0.0	0.0	0.0	0.0	0.1	0.4	1.2	1.8	1.8	1.3	0.7	0.3	0.1	0.0	0.0
15.5	0.0	0.0	0.0	0.0	0.0	0.1	0.1	0.4	0.6	0.7	0.5	0.3	0.1	0.0	0.0	0.0
16.5	0.0	0.0	0.0	0.0	0.0	0.0	0.2	0.2	0.2	0.2	0.1	0.1	0.1	0.0	0.0	0.0

3 Research Methodology

3.1 Selection of Ship Types

Dynamic stability failures under the Second Generation Intact Stability Criteria (SGISC) strongly depend on hull form, ship size and loading conditions. The selection of ship types for this study is driven by two key factors: historical incidence of dynamic stability failures and representation of diverse hull forms and operational characteristics. The study focuses on four vessels: two container ships (Duisburg Test Case [DTC] and D-Container), a bulk carrier (D-Bulker), and a RoPax vessel (D-RoPax). These ship types are chosen because of their known potential vulnerability[22] to SGISC-based failure modes, their prominence in global shipping, and the availability of data for analysis. Table 5 lists main particulars of the ships in their design loading conditions.

Table 5: Main particulars of the sample ships

Main Dimension	Symbol	Unit	DTC	D-Container	D-Bulker	D-Ropax
Overall length	L_{OA}	m	390.5	196.6	224	221.5
Length b/w perpendiculars	L_{BP}	m	355	185	215	207
Maximum breadth	B	m	51	32	36	36
Depth	D	m	30	20	21	14
Design Draft	d	m	14.5	9	15	7.2
Waterplane area	A_{WL}	m^2	15,254	4,733	7,312	7,432
Displacement	Δ	t	178,101	33,612	101,633	31,855
Block coefficient	C_b	-	0.66	0.61	0.85	0.58
Midship coefficient	C_m	-	0.98	0.97	0.99	0.82
Bilge keel area	A_k	m^2	54.6	30.4	34.4	34
Design speed	V_s	kn	25	21	14	22
Froude number	F_n	-	0.41	0.36	0.17	0.33

The main parameters listed in Table 5, including the overall length, beam, draft, displacement, and block coefficient, are important factors affecting the dynamic stability of each vessel and vulnerability to different SGISC failure modes.

Speed of the ship is a critical parameter that significantly influences vulnerability, especially parametric rolling and pure loss of stability. Recently, the design speeds of ships have been reduced to lower fuel consumption and comply with Energy Efficiency Design Index (EEDI) regulations[37]. For the DTC model, the design speed of 25 knots is used, as specified in the reference benchmark study [38]. For the D-Container model, a design speed of 21 knots is selected based on current propulsion trends in container vessels of comparable size [37]. The D-Bulker model represents a typical Panamax bulk carrier with high block coefficient. A design speed of 14 knots is selected which matches the typical design speeds for such vessels[39][40] . Finally, for the D-RoPax vessel, design speed of 22 knots is used, aligning with average speed documented in recent studies on RoPax vessels [41] [42].

Roll damping has a strong influence on dynamic stability, making the bilge keel a key

consideration in this study. The dimensions of the bilge keel significantly affect the roll motion characteristics, and thus the result of the vulnerability to failure modes. The length and width of the keel for the DTC model are obtained from an original benchmark study [38]. To ensure consistent roll damping effects across all ship models, the same bilge keel length-to-ship length ratio with width of 0.4 m are assumed. Since actual bilge keel dimensions are only available for the DTC model, this configuration was adopted for all sample ships with varying lengths. The bilge keel area for each vessel is listed in Table 2, and the bilge keel area-to-length ratio is set same for all ships based on the DTC reference, in order to approximate equivalent roll damping effect. This assumption allows for a more consistent basis of comparison in the SGISC vulnerability assessments, but actual damping effects may vary in real ships.

Natural roll period is a important parameter in evaluating dynamic stability and is directly used in SGISC vulnerability assessments. The SGISC guidelines refer to IS Code 2008, which estimates the roll period using a formula that depends on the metacentric height GM, and a coefficient C. The general formula of the roll period estimation is given below:

$$T_r = \frac{2 \cdot C \cdot B}{\sqrt{GM}} \tag{22}$$

However, this method has been shown to be less accurate for longer ships [43]. To improve the estimation accuracy, a new formulation of the coefficient C is recently proposed by the Japanese delegation and submitted to IMO (MSC108/INF.7) [44]. This offers a more accurate estimation of the rolling period for a wide variety of ships [43]. Ruponen et al. [45] present a comparison of both estimation methods along with model test reference values of multiple ships. Based on these findings, this study adopts the new coefficient formula proposed by the Japanese delegation, which is used in the main roll period formula (Equation 22). The new formulation for the coefficient is given below in Equation 23:

$$C = 0.3437 + 0.0240\frac{B}{d} \tag{23}$$

Here, B is the breadth and d is the draft of the ship.

3.1.1 Container Ships

Container vessels are crucial for global shipping because of their dominant role in transporting manufactured goods internationally. The significance of container ships has increased in recent years, particularly with the design evolution and rapid increase in the number of Ultra-Large Container Vessels (ULCVs). In 2008, ULCVs represented only approximately 1% of the global container capacity, which had increased to over 15% by 2023. This trend continues to increase, as evidenced by the significant proportion (43% in terms of TEU capacity) of current container vessel orders [37]. However, it has also increased the risk of dynamic stability failures owing

to pronounced bow flare, fine hull forms, and large deck stowage areas that amplify dynamic interactions with waves. Recent maritime accidents involving Ultra-Large Container Vessels, such as MSC Zoe (2019), ONE Apus (2020) and Maersk Essen (2021), also highlight the vulnerability of large container vessels[34].

Due to different size categories and operational parameters, two container vessel models are selected for this study: a large container vessel and a smaller feeder-type container vessel. Duisburg Test Case (DTC), a 14,000 TEU post-Panamax benchmark model, is selected to represent this critical ULCV class, with its publicly available hull form and relevant data[38]. Figures 11 and 12 show the 3D hull form and hull sections of the DTC ship, respectively.

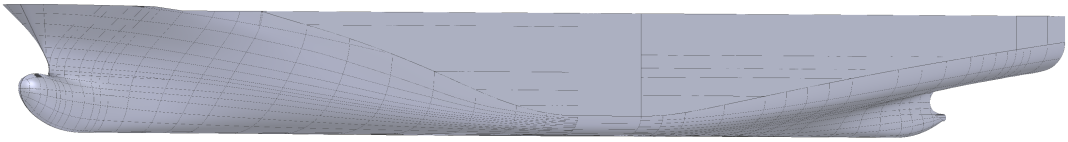

Figure 11: 3D view of the DTC hull form.

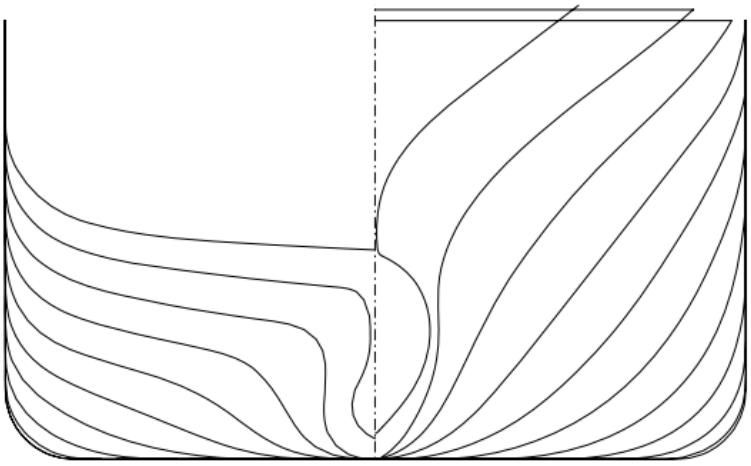

Figure 12: Hull Sections of DTC ship model [38]

Two loading conditions (LC-1 and LC-2) are analyzed, with GM values of 4.57 m and 1.37 m, respectively, to capture a range of operational conditions. The main particulars of both loading conditions are listed in Table 6. Because the benchmark study of the DTC model only provides the hull geometry without any superstructure details, a comparable ship profile was required to estimate the highest location required for excessive acceleration vulnerability assessment. The ONE APUS container ship, which has a principal dimension nearly the same as that of the DTC model, is used as a reference. The bridge of the ONE APUS, where crew operations take place, is identified as the highest point onboard. The vertical position from the keel and horizontal distance from the aft perpendicular are measured and applied to the DTC

model. Figure 13 shows the general arrangement of the ONE APUS container ship used for this purpose.

Table 6: Loading conditions of Duisburg Test Case

Parameter	Symbol	LC-1	LC-2
Mean Draft	T_m [m]	12.0	14.0
Trim	Tr [m]	0	0
Displacement Volume	∇ [m^3]	136683	165980
Metacentric Height	GM_t [m]	4.57	1.37
Block Coefficient	C_B [-]	0.63	0.65
Natural Roll Period	T_r [s]	21.3	37.6
Vertical Location of Crew Area	z [m]	60	
Longitudinal Crew Location from AP	x [m]	218	

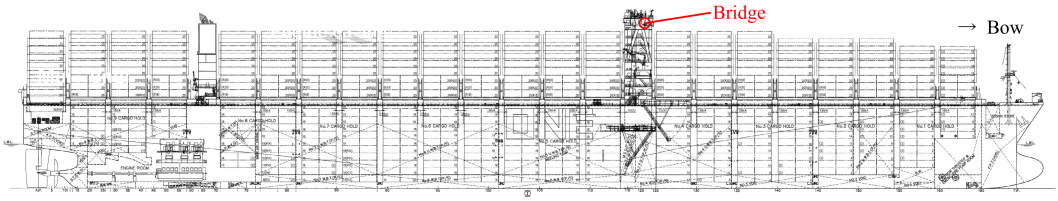

Figure 13: General Arrangement plan of One APUS Container Ship [46]

The smaller container vessel (D-container) represents the feeder ship category, which constitutes the largest portion (38%) of the global container fleet[37]. With a length of 196 m and block coefficient of 0.61, its hull form is different from the DTC model, allowing comparisons of vulnerability across segments of different sizes. The vulnerability assessment of two different models allows the study to effectively cover various sizes found in current container shipping industry. The model is taken from NAPA software demo ships library. Figure 14 and 15 shows 3D model and hull sections of the D-Container respectively.

Figure 14: 3D view of the D-Container hull form.

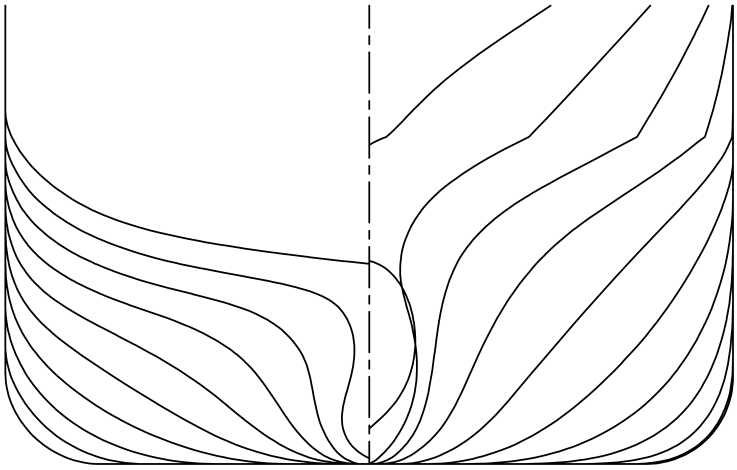

Figure 15: Hull sections of D-Container ship model

Two loading conditions with GM=6.57m and GM=1.83m are studied, representing the ballast and fully loaded conditions respectively. Main particulars of both loading conditions are given in Table 7. For the D-Container ship, the full vessel geometry, including the superstructure, is available from the NAPA demo library. Therefore, the highest location for evaluating excessive acceleration is directly identified at the bridge position. The vertical and longitudinal coordinates of this point, measured from the keel and aft perpendicular respectively, are provided in Table 7. Figure 16 shows the profile view of the D-Container ship with the selected EA calculation point.

Table 7: Loading conditions of D-Container ship

Parameter	**Symbol**	**LC-1**	**LC-2**
Mean Draft	T_m [m]	8.0	8.9
Trim	Tr [m]	0	0
Displacement Volume	∇ [m^3]	27953	32112
Metacentric Height	GM_t [m]	6.57	1.83
Block Coefficient	C_B [-]	0.59	0.60
Natural Roll Period	T_r [s]	11.0	20.4
Vertical Location of Crew Area	z [m]	41	
Longitudinal Crew Location from AP	x [m]	56	

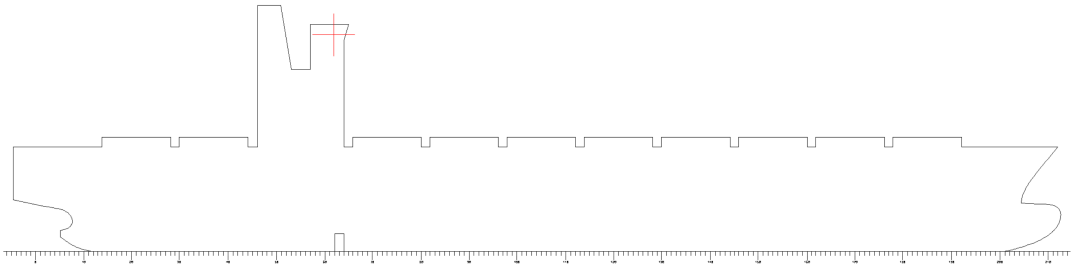

,

Figure 16: Profile view of D-Container ship with EA calculation point.

3.1.2 Bulk Carrier

Bulk carriers represent a major segment of the global merchant fleet,accounting for approximately 43% of the global fleet in terms of tonnage [39]. The bulk carrier used in this study represents a Panamax-size bulk carrier, which is the most common category among bulk carrier types [47]. A studied ship model, referred to as D-Bulker, is derived from the NAPA demo ship library. With an overall length of 224 m and a high block coefficient of 0.86, the hull features a full hull form, typical for bulk carriers. Such vessels generally have higher metacentric height (GM) in fully loaded conditions compared to container ships due to their fuller hull geometry and vertically lower cargo weight distribution. Figure 17 and Figure 18 present the 3D view and the body plan (hull sections) of the D-Bulker, respectively.

Figure 17: 3D view of the D-Bulker hull form.

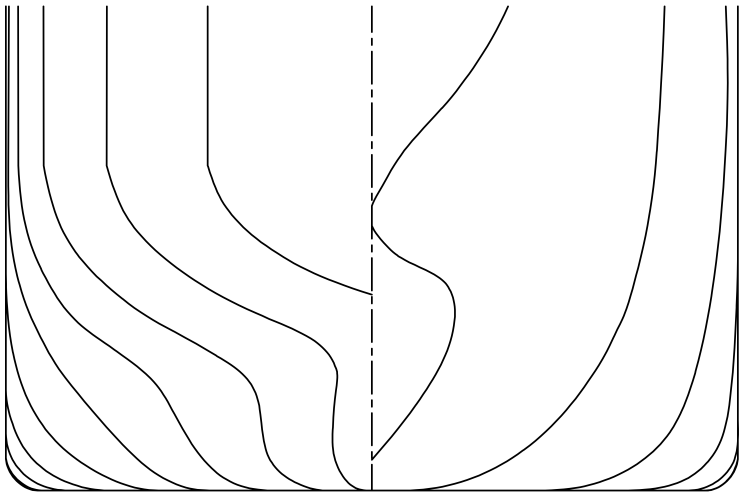

Figure 18: Hull sections (body plan) of the D-Bulker ship model.

Two loading conditions with $GM = 3.58$ m and $GM = 7.0$ m are studied, representing two fully loaded cargo scenarios. Main particulars of both loading conditions are listed in Table 8. The first condition assumes carrying a dry bulk cargo, whereas the second considers loading a high-density cargo, such as steel coils or iron ore. For high-density cargo, it is common practice to load alternate cargo holds while leaving the others empty. This arrangement, known as Alternate Hold Loading (AHL), is illustrated in Figure 19. The AHL is used to maintain a higher vertical center of gravity, thereby reducing the metacentric height. Although one set of holds remains empty, the total displacement remains approximately the same. This is because the weight of the cargo in the filled holds is nearly double that of the dry cargo, resulting in a comparable overall weight [48]. The GM value for the bulk carrier loaded with a high-density cargo is referenced from a study analyzing a vessel of similar size under AHL conditions [49].

Table 8: Loading conditions of D-Bulker

Parameter	**Symbol**	**LC-1**	**LC-2**
Mean Draft	T_m [m]	15	15
Trim	Tr [m]	0	0
Displacement Volume	∇ [m^3]	99,022	99,022
Metacentric Height	GM_t [m]	3.58	7.0
Block Coefficient	C_B [-]	0.85	0.85
Natural Roll Period	T_r [s]	15.3	10.9
Vertical Location of Crew Area	z [m]	37	
Longitudinal Crew Location from AP	x [m]	28	

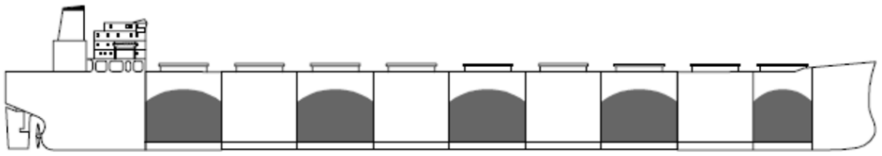

Figure 19: Alternate Hold Loading (AHL) condition with heavy cargo in a bulk carrier [48].

The highest point for excessive acceleration assessment is identified at the bridge, where crew operations typically occur. The vertical and longitudinal coordinates of this point, measured from the keel and aft perpendicular respectively, are listed in Table 8. Figure 20 shows the profile view of the D-Bulker model with the selected EA calculation point at the bridge.

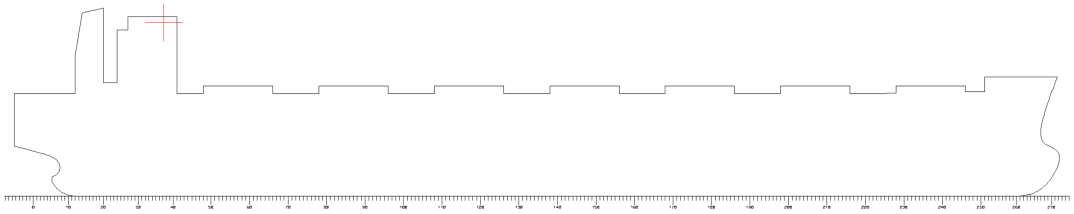

Figure 20: Profile view of D-Bulker with excessive acceleration calculation point

3.1.3 Ropax Vessel

RoPax (Roll-on/Roll-off Passenger) vessels are designed to transport both passengers and vehicles, featuring a long and streamlined hull with a relatively low block coefficient. The D-RoPax model used in this study is based on a representative ship from the NAPA demo ship library. This model has a length of 210 meters and a block coefficient of 0.56, reflecting the slender geometry typical for RoPax vessels. Such hull forms are optimized for higher speeds and reduced resistance. Figure 21 and Figure 22 present the 3D view and body plan of the D-RoPax model, respectively.

Figure 21: 3D view of the D-Ropax hull form.

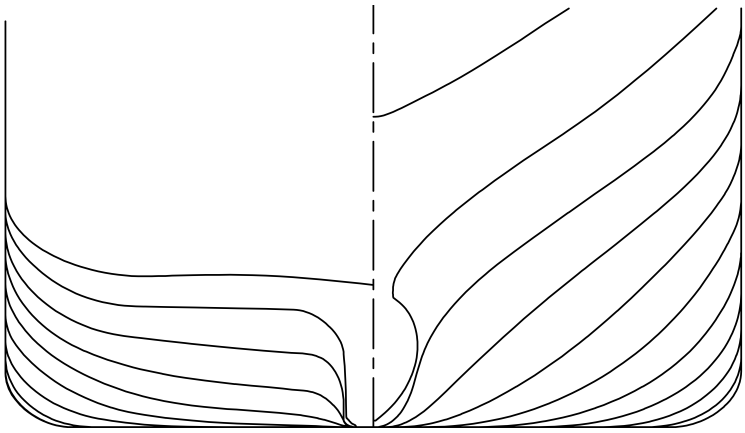

Figure 22: Hull sections of D-Ropax ship model

RoPax vessels typically operate on short sea routes and are usually maintained in a consistent loading condition due to their passenger and vehicle transport roles. Therefore, only one representative loading condition is considered for the D-RoPax model. The main particulars of this condition are summarized in Table 9. For the excessive acceleration (EA) assessment, several high and potentially vulnerable points are identified on the ship. A total of four EA points are selected for the vulnerability evaluation, with the highest point located at the bridge, where crew operations are typically performed. The coordinates of this point, measured from the keel and aft perpendicular, are also listed in Table 9. Figure 23 shows the profile view of the D-RoPax model with the indicated EA calculation points.

Table 9: Loading condition of D-RoPax ship

Parameter	**Symbol**	**LC-1**
Mean Draft	T_m [m]	6.3
Trim	Tr [m]	0
Displacement Volume	∇ [m^3]	26172
Metacentric Height	GM_t [m]	2.88
Block Coefficient	C_B [-]	0.56
Natural Roll Period	T_r [s]	20.4
Vertical Location of Crew Area	z [m]	35
Longitudinal Crew Location from AP	x [m]	168

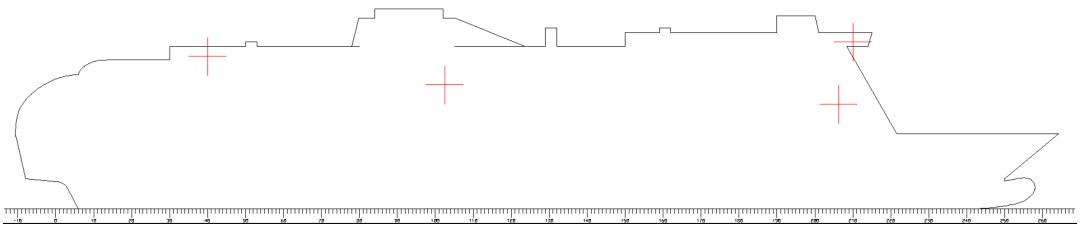

Figure 23: Profile view of D-RoPax ship with excessive acceleration calculation points.

3.2 Selection of Wave Data Source

The SGISC Level 2 vulnerability assessment, as outlined in the IMO guidelines, requires three main inputs: the loading conditions, ship design parameters, and environmental wave data. For the environmental input, the SGISC recommends using a wave scatter table based on IACS Recommendation No. 34 Rev.1. This table provides the long-term joint probability distribution of significant wave height and zero-crossing period for different sea states as shown in Table 4. The underlying data are based on historical wave observations recorded by ships and compiled as the Global Wave Statistics (GWS), published by British Maritime Technology (BMT) [28]. The Rev.1 wave scatter table covers GWS zones 8, 9, 15, and 16 (see Figure 10), which are considered to represent most severe wave conditions in the global oceans[50].

Although the BMT dataset was the most accurate data available at the time of its publication, it does not reflect long-term climate variations. Many studies [32] [51] have also highlighted that BMT-based data may not accurately represent actual sea state, often representing more extreme conditions than the actual measurements. Now over the time, wave modeling techniques have improved significantly, and various global wave hindcast datasets have become available for use. Hindcast datasets are generated using numerical simulations and provide improved spatial and temporal resolution for describing ocean wave conditions. This data provide a more accurate and consistent description of wave conditions by simulating sea states over extended periods [31]. Several global hindcast datasets are now widely used, including ERA5, ERA-Interim, IOWAGA, NOAA, and WAVERYS. These differ in modelling approach, resolution, wind forcing, and validation method. Their key features are summarised in Figure 24. A detailed comparison of these datasets was presented in a recent study, where IOWAGA hindcast dataset was shown to have the highest accuracy when validated against satellite altimeter measurements[52].

Dataset	ERA5	ERA-INTERIM	IOWAGA	NOAA	WAVERYS
Provider	ECMWF	ECMWF	IFREMER	NOAA	Copernicus
Software	WAM	WAM	WWIII	WWIII	MFWAM
Release date	2018	2006	2016	2017	2019
Wind forcing	ERA5	ERA-Interim	CFSR*	CFSR	ERA5
Resolution (grid)	0.36°	0.75°	0.5°	0.5°	0.2°
Time step	1h	6h	3h	3h	3h
Full spectra	Yes	Yes	Some	Some	No
Range	1950-2019**	1979-2018	1990-2016*	1979-2009	1993-2018
Data access	API	API	FTP	FTP	FTP
Altimeter	Assimilation	N/A	Calibration	N/A	Assimilation

Figure 24: Comparison of key features of commonly used global hindcast datasets[52].

Furthermore, recognising the limitations of the Rev.1 wave scatter table, IACS recently updated the previous wave scatter table to Rev.2 [53]. The Rev.1 wave scatter table is based on the BMT data, and the revised table is based on the IOWAGA hindcast dataset. It has now been extended further south to include additional zones 24 and 25, as shown in Figure 25. Although the SGISC guidelines still adopt the IACS Rev.1 wave scatter table, this study also includes the use of the Rev.2 table to compare the vulnerability results between Rev.1 and Rev.2. A comparison of the Rev.1 and Rev.2 wave scatter diagrams is shown in Figures 26. It is important to note that Rev.1 uses the zero-crossing wave period (T_z), while Rev.2 uses the mean wave period (T_m). It can be seen that Rev.2 shows a different distribution of wave heights, with generally fewer extreme sea states compared to Rev.1.

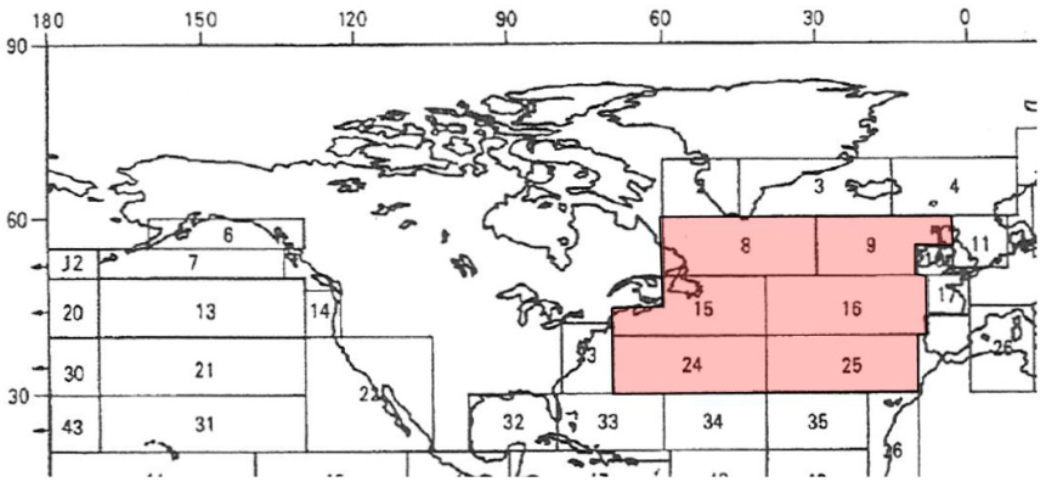

Figure 25: Sea areas included in the updated IACS Rev.2 wave scatter table. [54]

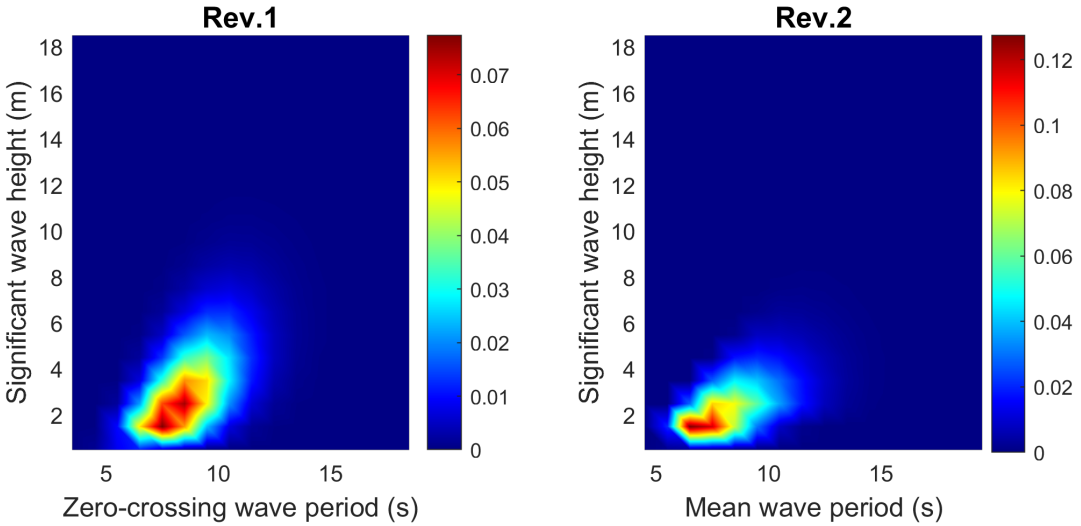

Figure 26: Comparison of wave scatter diagrams between IACS Rev.1 and Rev.2 .

While the IOWAGA dataset appears to be the most accurate option available, it is not straightforward to use directly for global zone-based comparisons. The dataset provides high-resolution outputs on a fine spatial grid, which makes it difficult to match with the GWS zones (big rectangular area). To represent GWS zones with such high-resolution data requires retrieving large volumes of data and performing extensive post-processing. On the other hand, the GWS zone-based approach offers simplicity and consistency, and it has been widely used in many studies.

To overcome this, a recent study adapted the IOWAGA hindcast data to develop wave scatter tables for all GWS zones, offering a more accurate alternative to BMT based GWS wave data[31]. These tables are expressed in terms of significant wave height and mean wave period. Since the SGISC criteria are based on the Bretschneider wave spectrum, the mean wave period (T_{m}) is converted to the zero-crossing period (T_z) using relation shown in Equation 24 [35].

$$T_z = \frac{T_{\mathrm{m}}}{1.0864} \tag{24}$$

Based on the improved accuracy of the IOWAGA hindcast data and its compatibility with the GWS zone structure, this dataset is used for the present study. Hindcast based wave scatter diagrams for all GWS zones studied in this study are presented in Appendix A.

3.3 Selection of Sea Areas

This section explains how global sea areas were selected for vulnerability assessment, based on the operational patterns of different ship types. The selection is primarily based on global traffic density data, with high-density routes of ship category is used to identify zones.

Global traffic density of container ships was analyzed using AIS-based route data in the study by Hashimoto et al. [26]. Based on this analysis, the authors identified high-density sea zones for the SGISC Level 2 assessment. The same selected zones, drawn on the global traffic density map, are shown in Figure 27 and are also used in this study for the vulnerability assessment of container ships. These zones are also considered suitable for bulk carriers, as both ship types follow largely overlapping high-traffic routes and share many common ports [55].

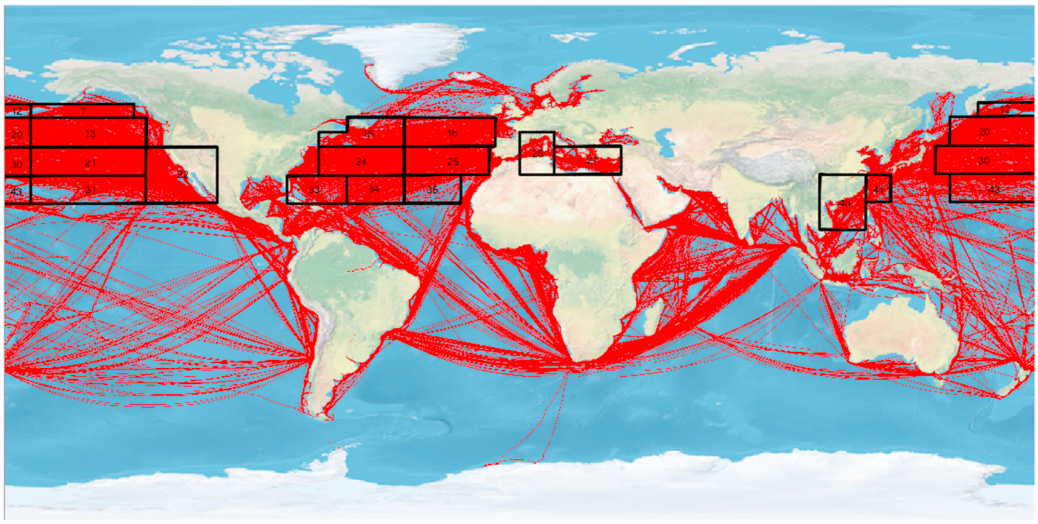

Figure 27: Global container ship routes showing high-density shipping lanes. [26]

Two new zones (85 and 90) have been added to this study to reflect recent changes in global shipping routes. These changes are due to the disruption of typical route through the Suez Canal [56]. Many ships are avoiding the Red Sea and taking a longer route around the Cape of Good Hope via South Africa. Table 10 presents the final selection of major cargo shipping zones used in the vulnerability assessments of container ships and Bulk carrier.

Table 10: GWS zones representing major Cargo shipping routes

Area	GWS zone number
Centre-North Atlantic	15, 16, 24, 25, 33, 34, 35
Centre-North Pacific	7, 12, 13, 20, 21, 22, 30, 31, 43
East, South China Sea	40, 41
Mediterranean Sea	26, 27
South Atlantic	85, 90

Multiple sources are used to identify sea zones relevant to global RoPax vessel routes. In European seas and the Mediterranean Sea, significant RoPax traffic exists between various countries [57]. Zone 5 is selected to represent the Baltic Sea, which has high

volumes of RoPax traffic in the Baltic Sea. Zone 11 covers the North Sea, where traffic between the UK and continental countries is significant. Zone 10 includes the Irish Sea, which primarily hosts routes between the UK and the Republic of Ireland. Zone 17 represents the Bay of Biscay, a region mainly used by RoRo vessels but also featuring RoPax routes between Spain and UK. Similarly, Zones 26 and 27 are selected to represent the Mediterranean Sea, where significant RoPax activity occurs between coastal countries. In the East China Sea, RoPax traffic primarily operates between three countries: China, South Korea, and Japan, based on routes identified from multiple sources [58, 59]. In this study, Zones 18, 28, and 29 are selected to represent RoPax activity in this region, covering key routes between these countries. Table 11 presents the final selection of major Ropax traffic zones used in the vulnerability assessments of D-Ropax.

Table 11: GWS and regional zones representing major RoPax shipping routes

Area	Zone number or region
European seas	5, 10, 11, 17
Mediterranean Sea	26, 27
East China Sea	18, 28, 29
Australia	Bass Strait

In the Oceania, RoPax traffic mainly operates between mainland Australia and the island state of Tasmania. However, when referring to the Global Wave Statistics (GWS) zones (see Figure 28), this specific region is not directly dedicated zone. The nearest zones: 92, 93 and 101 are large and cover wider oceanic areas, which include more extreme sea states that are not representative of the Bass Strait itself.

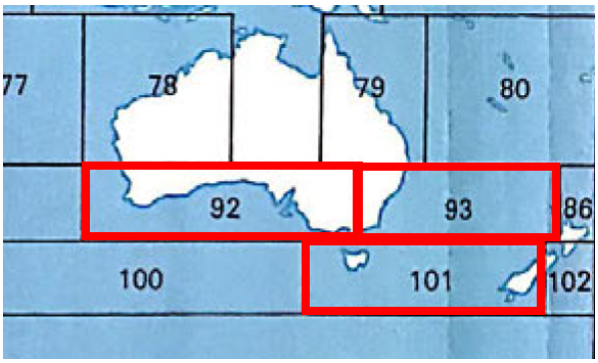

Figure 28: GWS zones near Tasmania and southern Australia [28].

Liu et al. investigated the wave climate of Bass Strait and South-East Australia over the period 1981 to 2020.[60], sea conditions in the Bass Strait are generally milder compared to surrounding sea regions. Figure 29 illustrates that extreme significant wave heights in the Bass Strait are lower, even during extreme return periods such as 50-year or 100-year events.

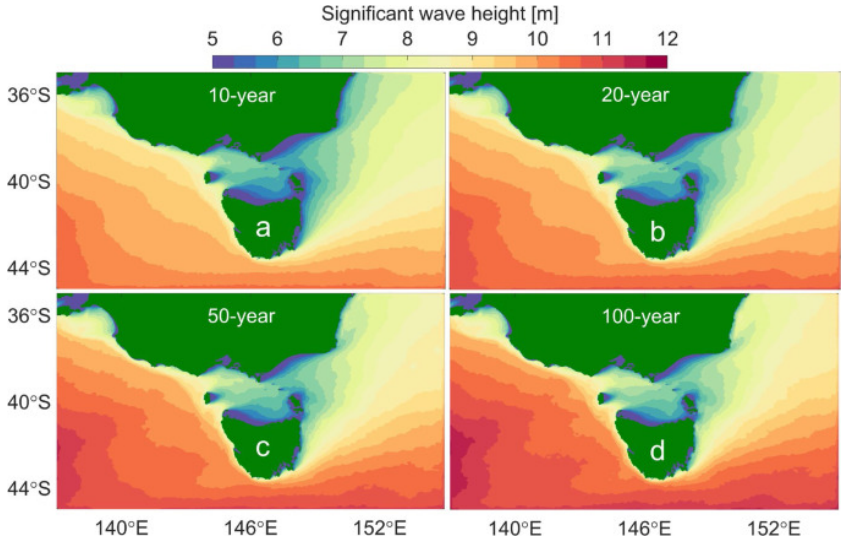

Figure 29: Extreme significant wave heights in the Bass Strait [60]

Therefore, instead of using broad GWS zones, this study uses regional wave climate data from the www.waveclimate.com database to better represent the actual sea state in the Bass Strait. The selected area, shown in Figure 30, is a 400km × 400km offshore region centered at 40 ° S, 146 ° E, which captures the local sea conditions relevant to RoPax operations in the Bass Strait.

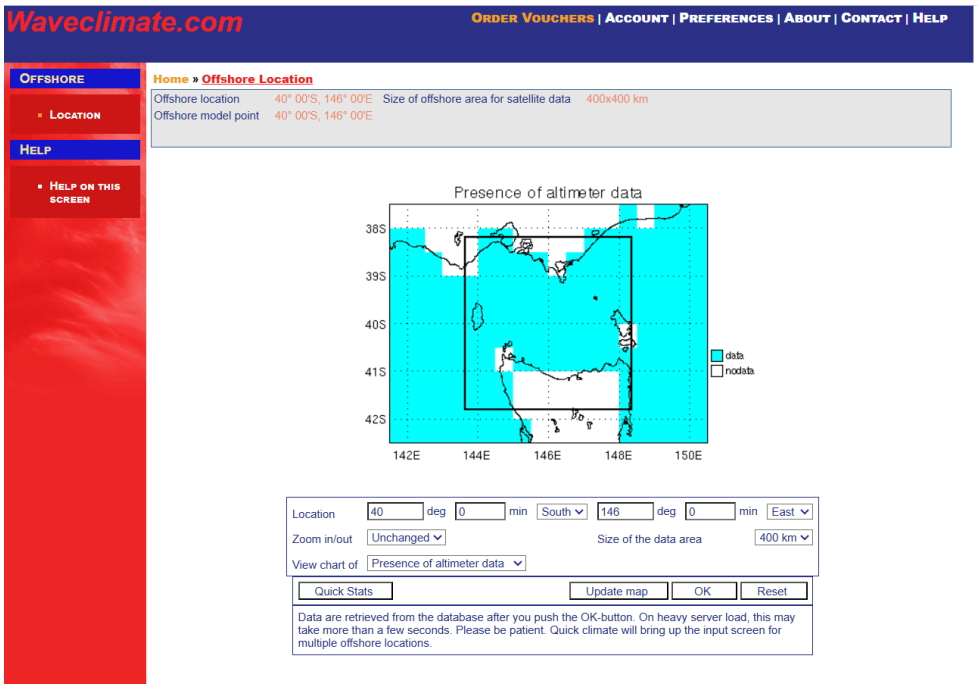

Figure 30: WaveClimate offshore data box covering Bass Strait region[61]

In total, 27 GWS zones and one regional zone (Bass Strait) are selected to represent

the most relevant operational areas for all sample ships. The selected zones are visualized on the map in Figure 31. These zones define the wave scatter tables used as environmental input for all vulnerability assessments conducted in this study.

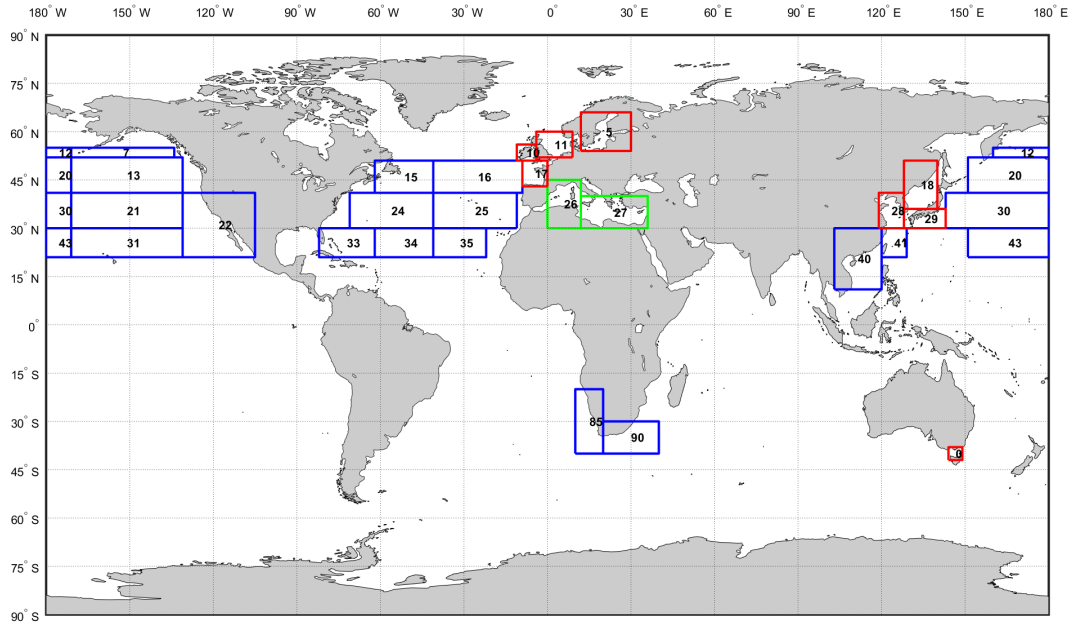

Figure 31: Global Wave Statistics Map for high traffic zones. Blue: container ship/bulk carrier routes; Red: RoPax routes; Green: Common zones for all sample ships.

3.4 Applied Software for Vulnerability Calculations

This study utilized NAPA software to perform failure vulnerability assessments of all sample ships in accordance with the SGISC guidelines. NAPA is a well-established and widely used software tool for ship design in the industry. The software can perform Level 1 and Level 2 SGISC calculations. In this study, only Level 2 vulnerability assessments are performed, which are more complex and require evaluation across multiple sea states using wave scatter data.

All vulnerability assessments are performed using NAPA Release 2024.2[62] , specifically using the VARDEF*SGIS.MATRIX module. This module allows users to define the failure mode of interest and provide all the input values required for the assessment of vulnerability Level 2. It also supports the import of user-defined wave-scatter tables. By default, it includes the standard wave scatter table recommended by SGISC guidelines. The wave scatter tables of all other zones are imported into the software and made available for selection within the module for zone-wise level 2 vulnerability calculations. After defining all inputs, level 2 calculations are performed and the final vulnerability index values are obtained for each loading condition and selected wave scatter table. An example of the interface of the module used to perform parametric rolling calculations for DTC is shown in Figure 32.

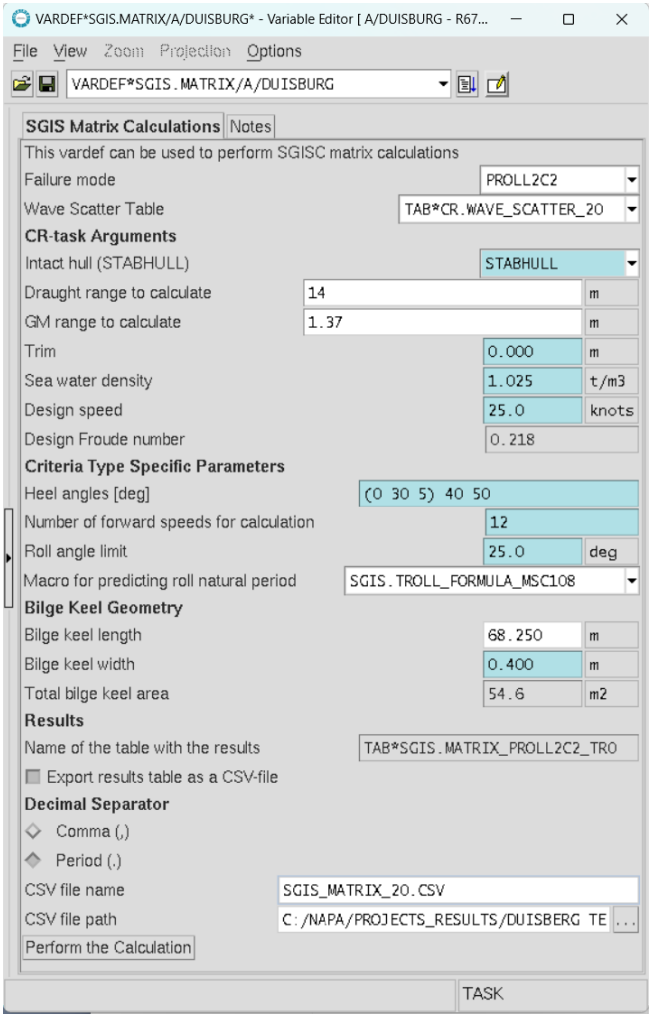

Figure 32: Interface of NAPA module used for performing SGISC calculations.

3.5 Data Collection and Analysis

To assess the vulnerability of the selected ship types against the defined failure modes, the results are calculated and analyzed in two main stages.

In the first stage, the Level 2 vulnerability criteria are evaluated using a set of predefined loading conditions for each ship, defined by their GM and draft as explained earlier. The vulnerability criteria are computed across all relevant GWS zones for each failure mode. This initial analysis allows the identification of critical sea zones and provides a comparative understanding of how different loading conditions affect the risk of failure. In the second stage, a more detailed analysis is performed through the generation of vulnerability matrices. For each ship and failure mode, the level 2 criteria values are recalculated over a wide range of GM and draft combinations, forming a two-dimensional vulnerability map for selected GWS zones. Two zones are selected for this purpose: one with high vulnerability and another one with relatively lower risk, as identified in the first stage. This approach provides deeper insight into

the sensitivity of vulnerability to loading conditions, allowing the identification of critical combinations of GM and draft that may lead to failing the SGISC criteria. To support this analysis, each matrix is paired with the corresponding wave scatter diagram of the zone, which illustrates the probability of different sea states in that zone. Overall, this two-step methodology ensures a comprehensive understanding of how ship stability performance varies with both operational loading and environmental conditions. The vulnerability index values obtained from NAPA were further processed in MATLAB to organize the results zone-wise. MATLAB is used to generate all figures, including vulnerability matrix plots and zones-comparative plots for detailed analysis and presentation.

4 Results

4.1 Parametric Rolling

4.1.1 Duisburg Test Case

Figure 33 shows the Level 2 C2 vulnerability index values for parametric rolling across different sea zones for the DTC container vessel in two loading conditions as defined in Section 3.1.1. In LC-1, the C2 values are nearly zero in all zones, indicating that the ship is not vulnerable to parametric rolling with high GM. In contrast, LC-2 shows noticeable C2 values in several zones, suggesting increased vulnerability due to the lower metacentric height and reduced transverse stability. Figure 34 presents the SGISC vulnerability map for parametric rolling in the DTC ship under LC-2. It shows the relative risk levels across global sea zones based on logarithmic scaled vulnerability index values, where the most critical zone has the highest vulnerability level.

The IACS Rev.1 wave scatter table gave the highest C2 value, although it still remained below the SGISC threshold ($R_{PR2} = 0.025$). This dataset represents the original North Atlantic wave conditions used in the SGISC guidelines. The newer IACS Rev.2, based on hindcast data, gave a much lower C2 value, not only lower than Rev.1 but also lower than the most critical sea zones in this study.

Considering the global sea areas, the Pacific Ocean showed the highest vulnerability, especially in Zone 13 and Zone 20, which appeared as the most critical after Rev.1. In the Atlantic Ocean, Zone 16 shows elevated values, while in the South Atlantic, Zone 90 (around the Cape of Good Hope) also shows relatively high vulnerability. However, the zones in the Mediterranean Sea and Southeast China Sea indicate a very low vulnerability to parametric rolling.

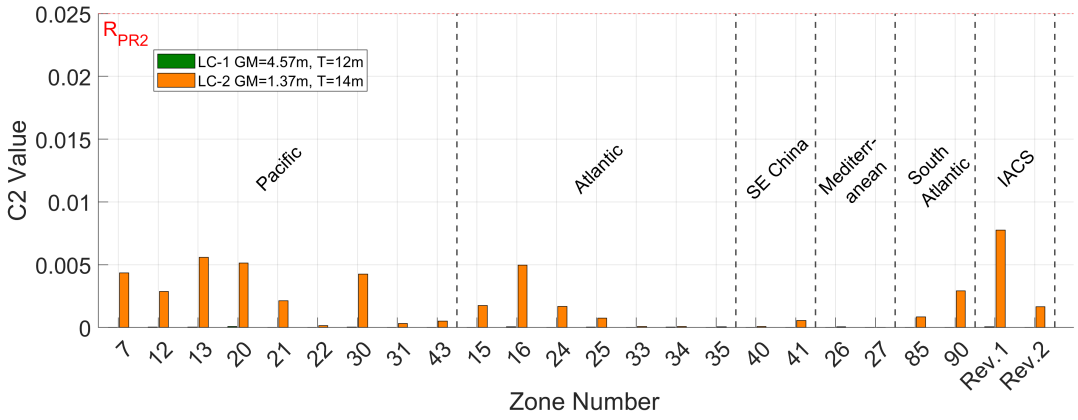

Figure 33: Parametric rolling Level 2 results for DTC across GWS zones.

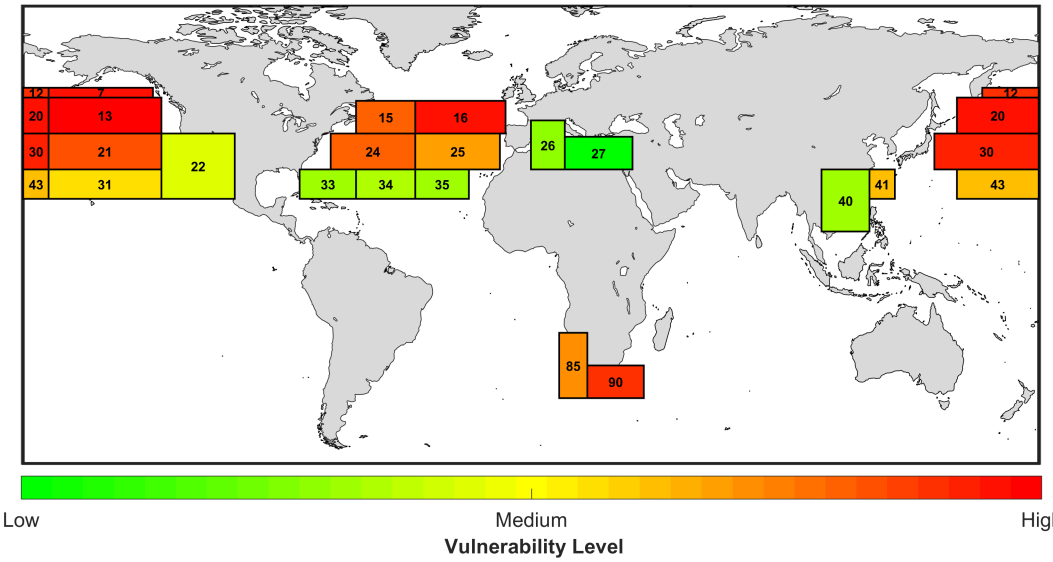

Figure 34: Parametric rolling vulnerability map for DTC under LC-2

Figures 35 and 36 present the matrix results for parametric rolling vulnerability of the DTC model in the Zones 13 and 15, respectively. These results provide a detailed view of how the failure criterion varies across different GM and draft combinations. Zone 13 was selected as the most critical area based on earlier analysis, while Zone 15 from the Atlantic represents a zone with comparatively lower vulnerability.

According to the SGISC vulnerability criteria, the overall vulnerability of the DTC vessel to parametric rolling remains low across most GM–draft combinations in both selected zones. In Zone 13, the vulnerable region appears primarily at low GM values, especially below 1 m, and is further increased when combined with lower drafts. A similar trend is observed in Zone 15, although the extent of vulnerability is less severe. The results demonstrate that parametric rolling vulnerability is highly dependent on GM, where lower GM values lead to an increased risk of failure. This behavior is consistent with the physical mechanism of parametric rolling, which typically develops at higher roll periods corresponding to low GM. These results further support the classification of Zone 13 as more critical than Zone 15, as its wave scatter diagram shows a broader distribution toward higher significant wave heights. As described in Section 2.2.1, the representative wave height $H_{r,i}$ used to assess vulnerability is mainly governed by the significant wave height H_s.

In addition to GM, the draft also affects the vulnerability, although to a lesser degree. At a same GM, lower drafts tend to show slightly higher vulnerability. This effect can be explained through hydrostatic characteristics. As shown in Table 12, the block coefficient (C_B) of the DTC model decreases from 0.667 at 15 m draft to 0.602 at 10 m. A lower C_B implies a finer hull form with more variation in water plane area along the length of the ship. This makes the vessel more sensitive to changes in wave profile as it encounters head or following seas. According to the rolling period formulation defined in Section 3.1, a lower draft results in a longer roll period for the ship. Consequently,

lower drafts provide more time for wave-induced stability variations to develop and amplify the roll motion. In contrast, shorter roll periods at higher drafts reduce this effect, making the vessel less vulnerable to parametric rolling.

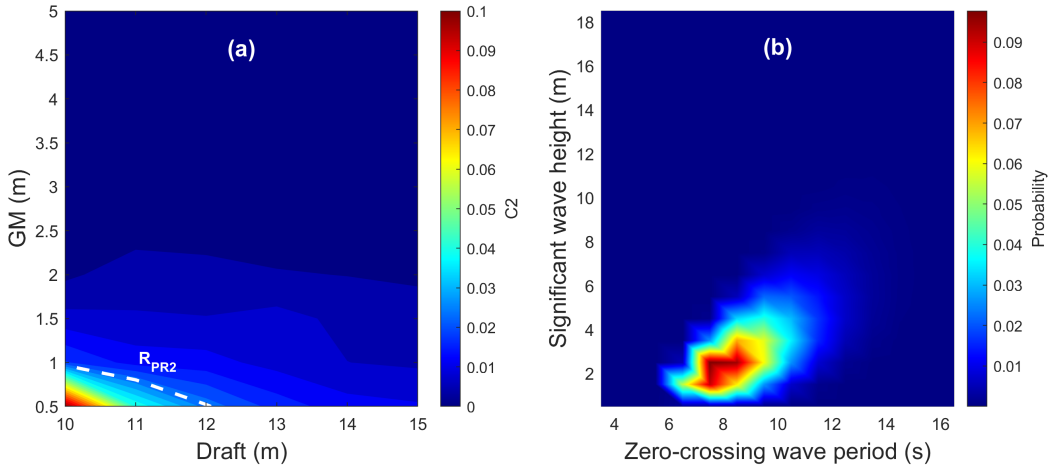

Figure 35: Zone-13 : (a) Parametric rolling Level 2 matrix results for DTC (b) Wave scatter diagram.

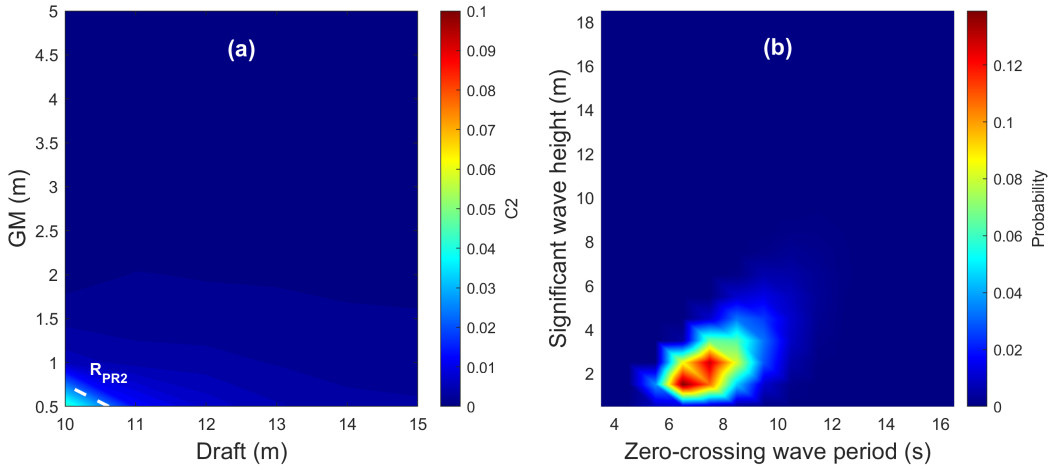

Figure 36: Zone-15 : (a) Parametric rolling Level 2 matrix results for DTC (b) Wave scatter diagram.

Table 12: Variation of Block Coefficient and Roll Period (at GM = 0.5 m) with Draft for the DTC model

Draft (m)	C_B	T_r (s)
10.0	0.602	67.2
11.0	0.615	65.6
12.0	0.629	64.3
13.0	0.642	63.2
14.0	0.654	62.2
15.0	0.667	61.3

These matrix results confirm that the DTC vessel is most vulnerable to parametric rolling in low GM and low draft conditions, particularly in zones with more extreme wave conditions, such as the Pacific. An overall comparison of the key factors related to parametric rolling is presented in Section 4.1.4, focusing on how they contribute to vulnerability across all the studied vessels.

4.1.2 D-Container

Figure 37 shows the Level 2 C2 vulnerability index values for parametric rolling across different sea zones for the D-Container vessel in two loading conditions as defined in Section 3.1.1. In LC-1, the C2 values are nearly zero in all zones, indicating no vulnerability to parametric rolling when the vessel operates with high GM. In contrast, LC-2 showed clear C2 values in multiple zones, reflecting increased vulnerability due to the reduced metacentric height and lower transverse stability. Figure 38 presents the SGISC vulnerability map under LC-2 based on log-scaled vulnerability index values of studied sea zones. The zone-wise vulnerability profile remains mostly similar to that seen in the DTC, with the same regions showing relatively high or low risk, although some zones display small differences in level of vulnerability.

The IACS Rev.1 wave scatter table produced the highest C2 value, although it remained below the SGISC threshold ($R_{PR2} = 0.025$). This corresponds to the original North Atlantic data used in SGISC guidelines. The IACS Rev.2, based on more recent hindcast data, gave a significantly lower C2 value, not only below Rev.1, but also lower than any of the real-world sea zones included in this analysis.

Among the sea zones, the Pacific Ocean again shows the highest vulnerability, with Zone 13 and Zone 20 standing out as the most critical areas after Rev.1. Zone 16 in the Atlantic Ocean and Zone 90 in the South Atlantic also show elevated C2 values. In contrast, the zones representing the Mediterranean Sea and Southeast China Sea show near-zero C2 values, indicating a very low risk of parametric rolling for the D-Container ship under both loading conditions.

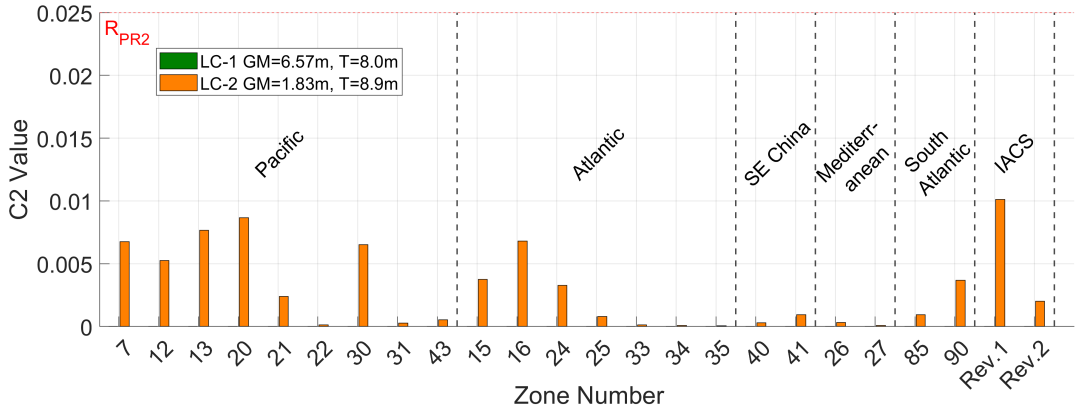

Figure 37: Parametric rolling Level 2 results for D-Container across GWS zones.

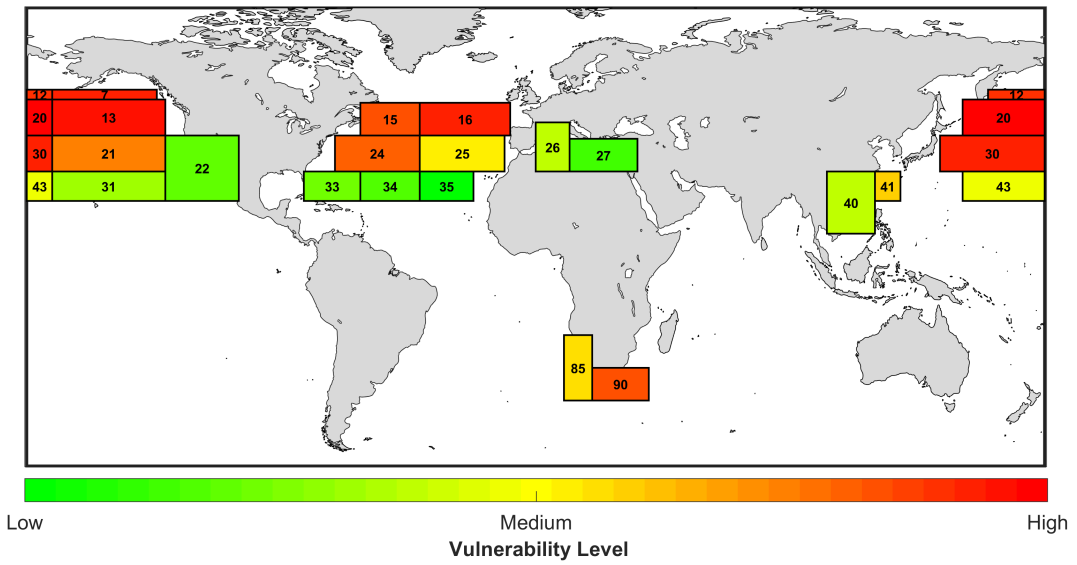

Figure 38: Parametric rolling vulnerability map for D-Container under LC-2

Figures 39 and 40 show the Level 2 matrix results for parametric rolling vulnerability of the D-Container vessel in Zone 13 and Zone 15, respectively. The same two zones were analyzed earlier for the DTC model to allow consistent comparison across sample ships. These plots illustrate how vulnerability varies over a range of GM and draft combinations.

In both zones, the results showed increased vulnerability at low GM values. In Zone 13, the C2 values exceeded the threshold primarily when GM is below 1.0 m and draft is about 10 m. However, even at low GM, the vulnerability reduced as draft decreases. In Zone 15, a similar vulnerability pattern is observed at low GM, but all values remained below the threshold. These trends further support the classification of Zone 13 as more critical than Zone 15, as its wave scatter diagram shows a broader distribution toward higher significant wave heights.

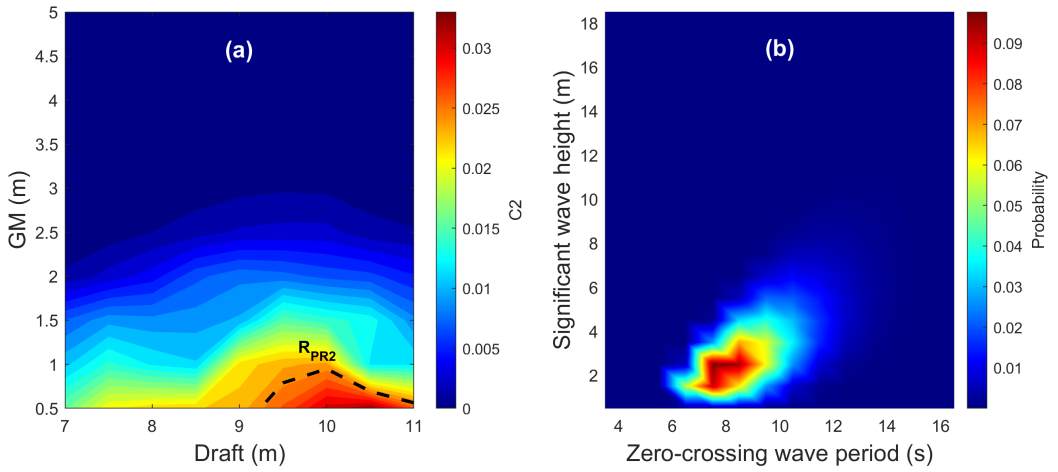

Figure 39: Zone-13 : (a) Parametric rolling Level 2 matrix results for D-Container (b) Wave scatter diagram.

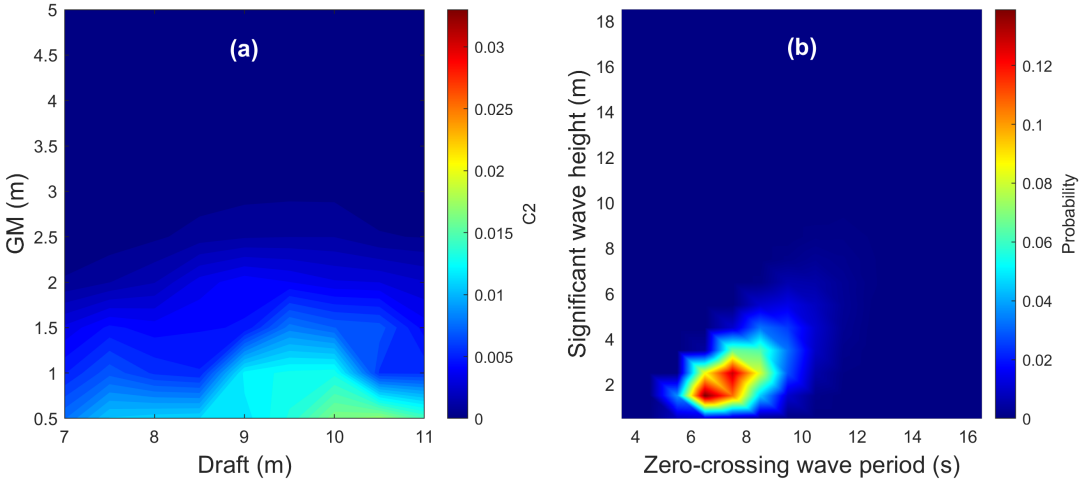

Figure 40: Zone-15 : (a) Parametric rolling Level 2 matrix results for D-Container (b) Wave scatter diagram.

Another important observation is that, unlike the DTC model, the D-Container vessel shows highest vulnerability at higher drafts when GM is fixed. This difference shows that hull form plays an important role in how draft affects parametric rolling. For the D-Container, more geometric changes occur around the 10 m draft level, where the hull form broadens to accommodate container cargo. This change resulted in greater variations in water plane area, which amplifies the parametric excitation mechanism. As shown in Figure 41, more geometric changes occurred at a 10 m draft. Although the block coefficient (C_B) increases gradually with the draft, the hull shape transitions more abruptly at a 10 m draft level, contributing to high vulnerability.

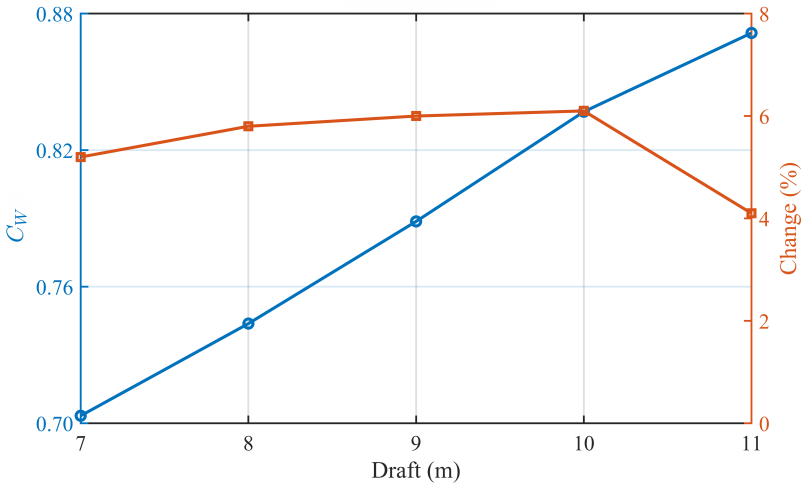

Figure 41: Water plane Coefficient (C_W) and its percentage change across drafts for D-Container ship

4.1.3 D-Ropax

Figure 42 shows the Level 2 C2 vulnerability index values for parametric rolling for the D-Ropax vessel across selected sea zones. The IACS Rev.1 wave scatter table results in a C2 value that exceeds the SGISC threshold, marking it as the only loading condition case in this study, where the C2 value exceeds the threshold defined by the criteria for parametric rolling. The Rev.2 value is also relatively high, but remains just below the threshold. Although the D-Ropax did not pass the criteria with standard wave scatter table (Rev.1), the vulnerability index remained below the threshold for all zones in possible ropax routes. Thus, according to the SGISC guidelines, operational limitations can be applied, which allow the vessel to operate in these areas under this loading condition without requiring design modifications.

Figure 43 presents the SGISC vulnerability map under loading condition based on log-scaled vulnerability index values of studied sea zones. Among the operational zones, the European seas showed the highest vulnerability, particularly Zone 17 (Bay of Biscay), followed by Zones 10 and 11. These three zones have the highest values among all zones evaluated for this ropax vessel. Other zones, such as those in the Mediterranean, East China Sea, and Bass Strait, yielded lower C2 values, but these are still notably higher than the values observed for the container vessels in the same zones.

These results indicate that the Ropax vessel exhibits a generally higher vulnerability to parametric rolling, which reflects the influence of its hull geometry and operational characteristics. Even in zones where the threshold is not exceeded, the values are significant, suggesting that D-ropax is more prone to dynamic instability compared to the others sample ships.

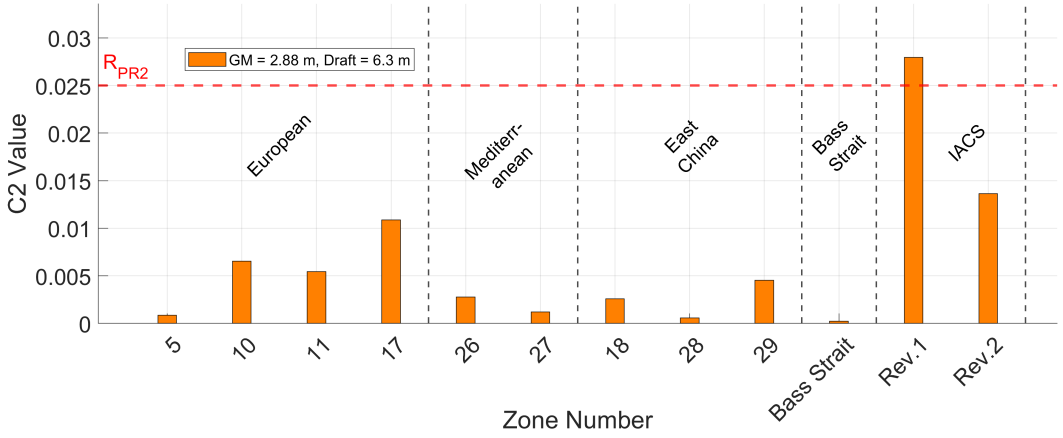

Figure 42: Parametric rolling Level 2 results for D-Ropax across GWS zones.

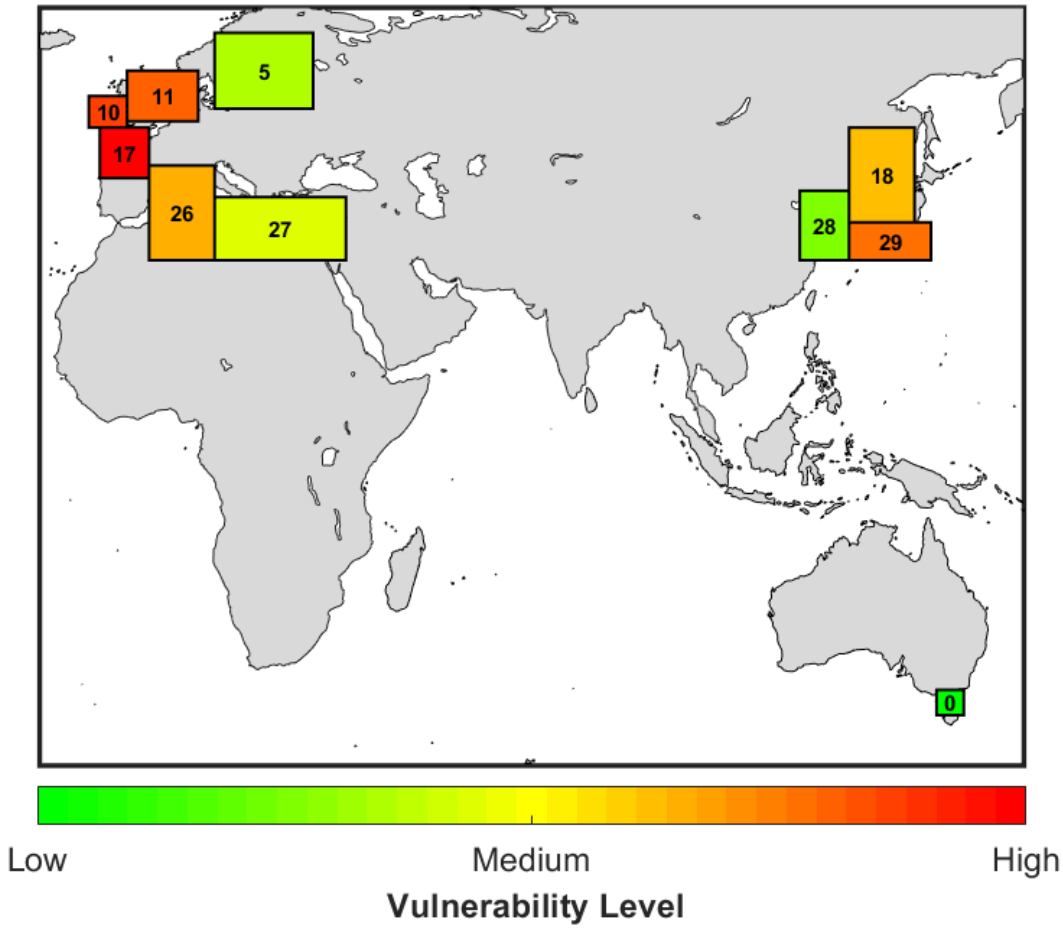

Figure 43: Parametric rolling vulnerability map for D-Ropax under loading condition

Figures 44 and 45 show the parametric rolling Level 2 matrix results for the D-

Ropax vessel in Zone 17 and Zone 26 respectively. Zone 17 was identified as the most vulnerable region based on earlier analysis, while Zone 26 was selected for its comparatively lower vulnerability.

The results show that vulnerability is low at higher GM values and increases significantly at lower GM, following a similar trend observed in the other vessels. However, the overall vulnerability of the D-Ropax is notably higher than that of the DTC and D-Container vessels. Even at moderately higher GM levels, significant C2 values are observed. Compared to the other ships, the block coefficient (C_B) of the D-Ropax is considerably lower at the studied drafts, indicating a more slender hull form. This behavior causes the water plane area to change more quickly with small changes in draft, making the ship more vulnerable to parametric rolling. Table 13 below shows the variation of C_B with draft:

Table 13: Variation of Block Coefficient with Draft for the D-Ropax model

Draft (m)	**Block Coefficient (C_B)**
4.0	0.497
5.0	0.524
6.0	0.548
7.0	0.573
8.0	0.595

Comparing the two zones, Zone 17 exhibits greater vulnerability across a wider range of conditions. This is supported by the wave scatter diagram, which shows more frequent occurrence of extreme sea states compared to Zone 26.

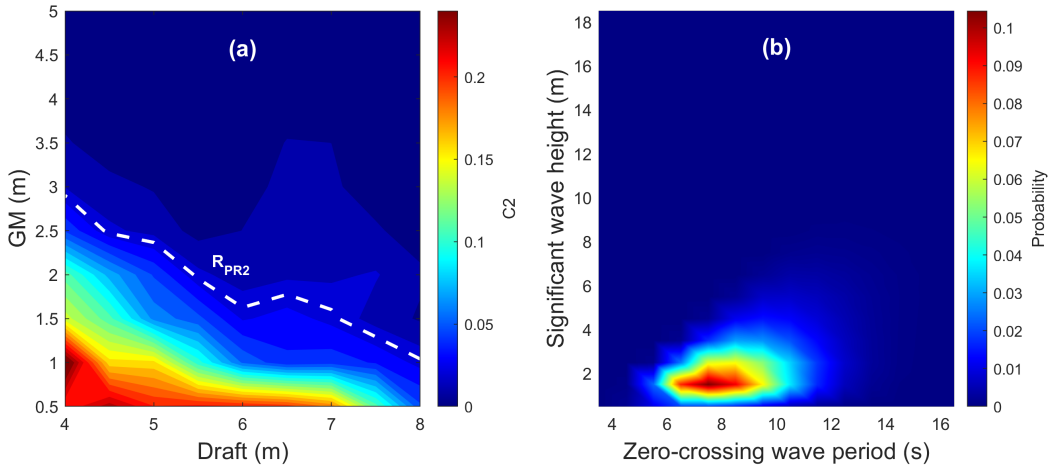

Figure 44: Zone-17 : (a) Parametric rolling Level 2 matrix results for D-Ropax (b) Wave scatter diagram.

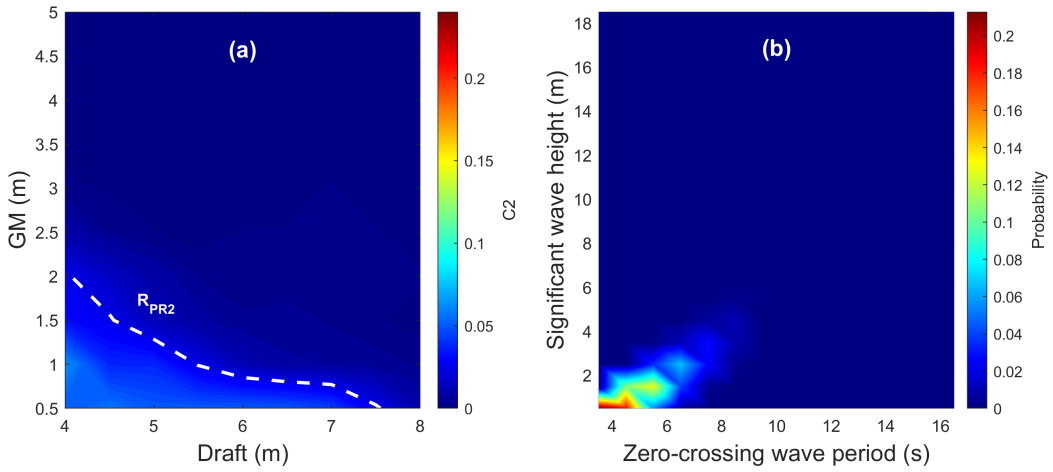

Figure 45: Zone-26 : (a) Parametric rolling Level 2 matrix results for D-Ropax (b) Wave scatter diagram.

At fixed GM values, the highest vulnerability is observed at lower drafts, particularly between 4 m and 5 m. This contrasts with the D-Container, where vulnerability increased at higher drafts. For the D-Ropax hull form, the geometry changes more abruptly at lower drafts, leading to increased variation in water plane area and amplifying the parametric rolling response under head or following seas.

4.1.4 Key Findings from the Parametric Rolling Assessment

The following points summarize the key factors influencing parametric rolling vulnerability across all ships and sea zones studied.

- **Metacentric height (GM):** Across all ships, the results show that lower GM values lead to increased vulnerability to parametric rolling. This is because a low GM reduces the restoring moment of the ship, which leads to a longer natural roll period and increases the vulnerability of the vessel. The longer roll period also brings the ship closer to the resonance condition $T_e \approx Tr/2$, which often occurs in following seas and can lead to parametric rolling[63].
- **Draft:** The effect of draft varies by hull form. DTC and D-Ropax showed higher vulnerability at lower drafts, which is also associated with longer roll periods, making them more prone to parametric resonance. In contrast, the D-Container vessel was more vulnerable at higher drafts at same GM due to a more abrupt change in hull form. These differences reflect how hull geometry responds to different draft levels and influences the ship dynamic behavior.
- **Hull Geometry:** The overall vulnerability to parametric rolling varies notably among the four sample ship. D-Ropax exhibits the highest level of vulnerability, followed by the D-Container and DTC vessels, whereas D-Bulker shows negligible vulnerability and was therefore excluded from the detailed analysis. This difference is closely linked to how the metacenter(KMT) of each hull changes

with draft at crest and trough waves. Change of metacenter at wave of 4 meter is shown in Figure 46, the D-Ropax experiences the greatest change in KMT across the studied drafts, making it highly vulnerable to parametric rolling. In contrast, the D-Bulker shows almost no variation in KMT with draft, indicating minimal sensitivity to wave-induced changes. Therefore, it is not vulnerable to parametric rolling. Overall, it can be observed that as the draft increases, the variation in the metacentric height (KMT) becomes smaller. This means that at lower drafts, the metacenter is more sensitive to wave profile changes, resulting in greater vulnerability when GM is fixed. Therefore, ships tend to exhibit higher vulnerability at lower drafts due to larger shifts in KMT between wave crest and trough conditions.

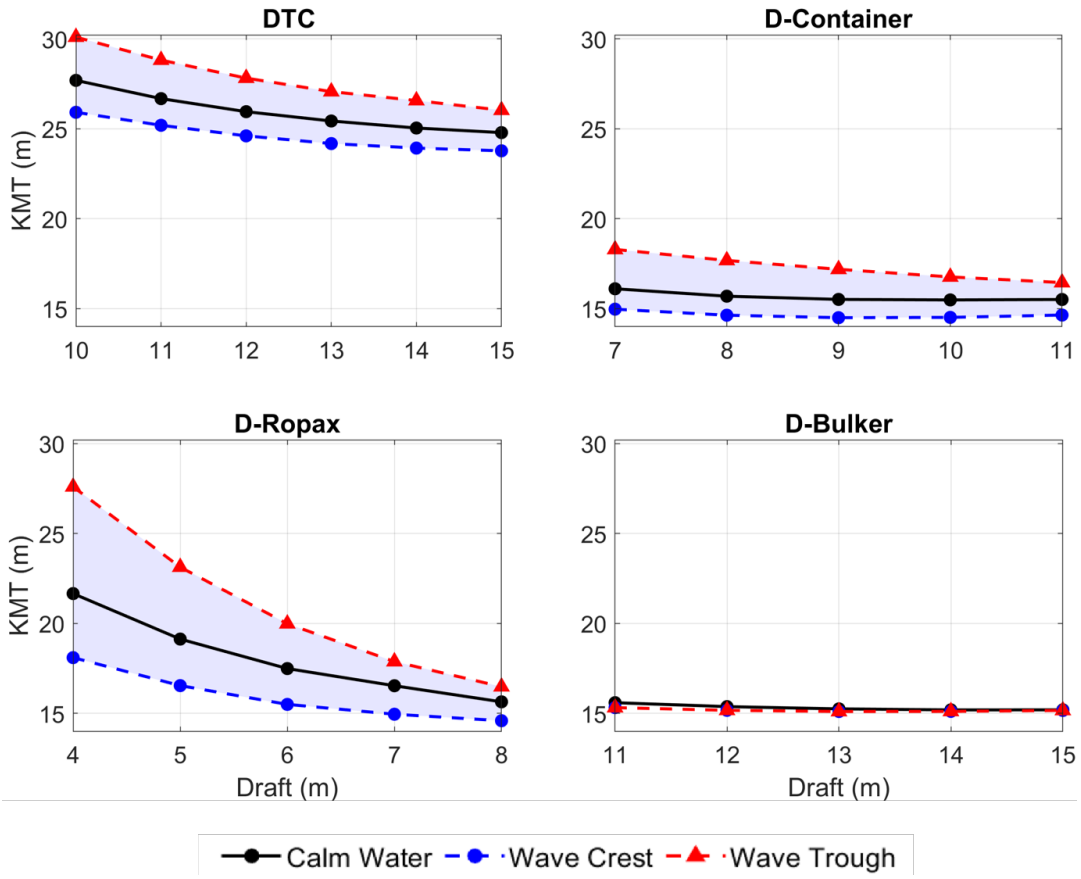

Figure 46: Change of Transverse Metacenter (KMT) between wave crest and trough across drafts for all sample ships

- **Environmental Conditions:** Significant wave height is a critical factor, as it drives changes in water plane area. Higher wave heights cause larger variations, increasing vulnerability. As described in Section 2.2.1, the representative wave height $H_{r,i}$ used to assess vulnerability is mainly governed by the significant wave height H_s. Zone-level comparisons show that higher vulnerability corresponds

to wave scatter diagrams with broader distributions toward high significant wave heights. For container vessels, the Pacific Ocean zones were more vulnerable, whereas the IACS Rev.1 dataset consistently produced the highest vulnerability index values across all zones. In the case of D-Ropax, the European sea zones showed the highest risk of vulnerability, with IACS Rev.1 resulting in the maximum index values.

- **Speed:** In the SGISC Level 2 assessment method, the design speed is used as input. It is further used in evaluating the vulnerability at 12 different speeds using defined speed factors, as described in Section 2.2.1. The final result is obtained by averaging the outcomes across these speeds in both head and following seas. Since lower speeds are more vulnerable to parametric resonance, ships with lower design speeds tend to show higher vulnerability index values under this approach [26].

These findings highlight the complex interaction between ship design, loading conditions, and wave environment in causing parametric rolling failures.

4.2 Pure Loss of Stability

4.2.1 Duisburg Test Case

Figure 47 shows the Level 2 vulnerability index values for pure loss of stability for the DTC container vessel across different GWS zones. In LC-1, all values remain close to zero, indicating no vulnerability under high GM conditions. In LC-2, several zones show higher values, although all values remain below the SGISC threshold.

The IACS Rev.1 wave scatter table again gives the highest vulnerability value for this failure mode, although the value remains below the SGISC threshold ($R_{PL0} = 0.06$). The IACS Rev.2 value is noticeably lower than Rev.1 and also lower than several other studied sea zones, placing it closer to the lower end of the vulnerability range.

The distribution of zone-wise vulnerability shows a trend similar to that observed in parametric rolling. The Pacific Ocean zones, particularly Zone 13 and Zone 20 continue to show the highest values among real sea areas, indicating that this region consistently presents a higher risk of dynamic stability failures. In the Atlantic, Zone 16 shows a moderate level of vulnerability. In the South Atlantic, Zone 90 also contributes to the higher end of the range. In contrast, zones in the Southeast China Sea, Mediterranean, and others show near-zero values, confirming low vulnerability for this failure mode in those areas.

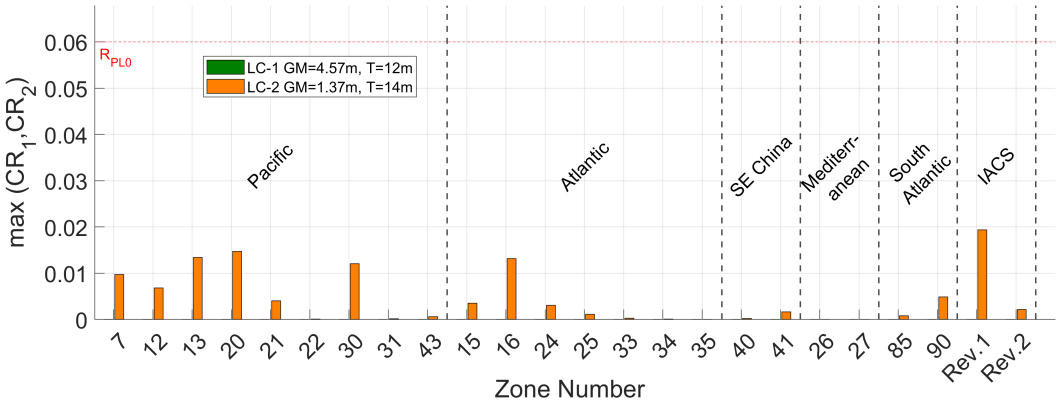

Figure 47: Pure Loss of Stability Level 2 results for DTC across GWS zones.

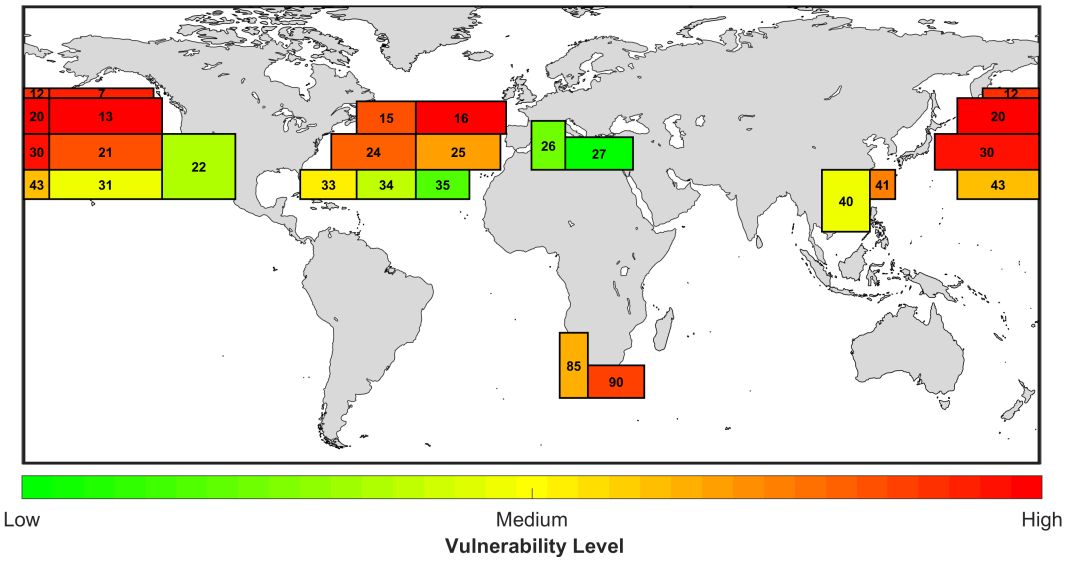

Figure 48: Pure Loss of Stability vulnerability map for DTC under LC-2

Figures 49 and 50 present the Level 2 matrix results for pure loss of stability vulnerability of the DTC model in Zone 20 (Pacific Ocean) and Zone 85 (South Atlantic), respectively. These zones were selected based on earlier analysis, with Zone 20 identified as one of the most critical sea areas and Zone 85 representing a region with moderate vulnerability.

In both zones, the results show that vulnerability is most significant at lower GM values, particularly when GM falls below 1.0m, where the index value exceeds the threshold defined by the Level 2 pure loss of stability criteria. The reason for this increased vulnerability at a low GM is the reduction in the restoring moment of the ship. This makes the ship more vulnerable to the effects of any external heeling moment, particularly when a wave crest passes amidships. With the wave crest at

midship, the righting lever curve further reduces, and the vessel may fail to meet the SGISC Level 2 criteria for pure loss of stability. Specifically, vulnerability is identified when either the vanishing stability angle (φ_V) falls below 30°, or when the wave-induced heel angle (φ_{SW}) exceeds 25° at heeling lever moment. At low GM, both of these failure conditions become more likely due to the limited stability reserve and reduced ability to recover from any external heeling moment.

Regarding the influence of draft, the results show that vulnerability is generally more pronounced at lower drafts. At a same GM, lower drafts correspond to slightly higher vulnerability indices. As explained in section 4.1.2, at lower drafts, the ship hull is finer, which reduces the ability of ship to generate a sufficient restoring moment in waves. In addition, results show that Zone 20 is more vulnerable to pure loss of stability than Zone 85. This is supported by the wave scatter diagram for Zone 20, which shows a broader distribution toward higher significant wave heights.

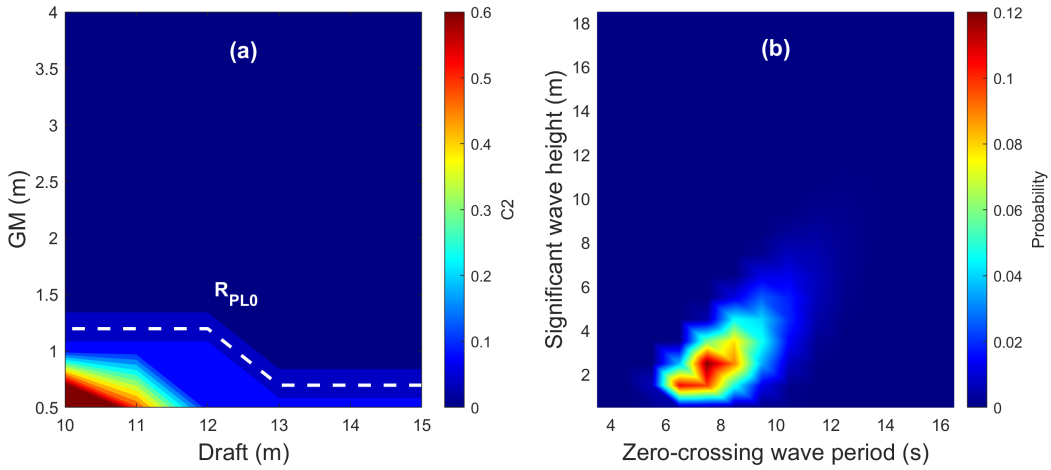

Figure 49: Zone-20: (a) Pure loss of stability Level 2 matrix results for DTC (b) Wave scatter diagram.

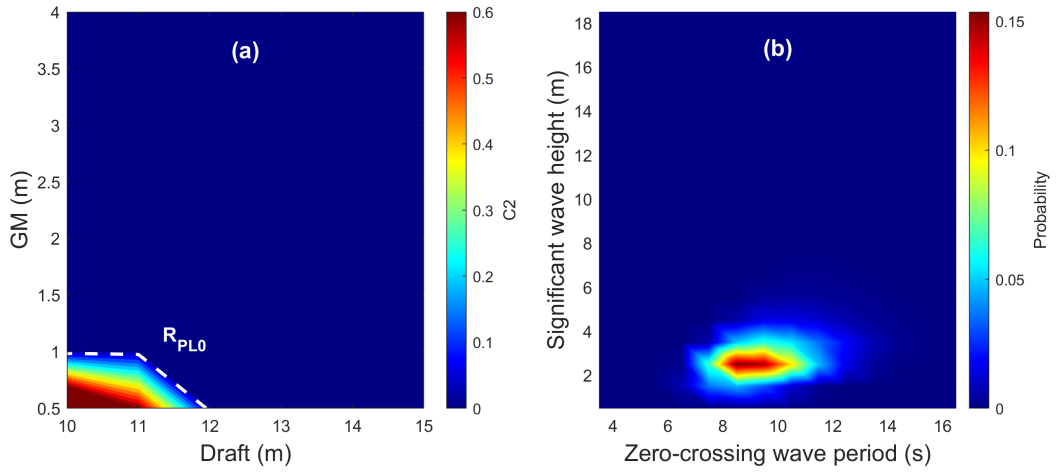

Figure 50: Zone-85: (a) Pure loss of stability Level 2 matrix results for DTC (b) Wave scatter diagram.

4.2.2 D-Container

Figure 51 shows the Level 2 vulnerability index values for pure loss of stability for the D-Container vessel across different GWS zones. For both LC-1 and LC-2, all values remain at or near zero, indicating no vulnerability under the evaluated loading conditions.

Since these loading conditions are predefined and used for all case studies, the actual sensitivity of the vessel is not fully captured in this analysis. A clearer understanding of the vulnerability is obtained through matrix results, where a wider range of GM and draft combinations is evaluated.

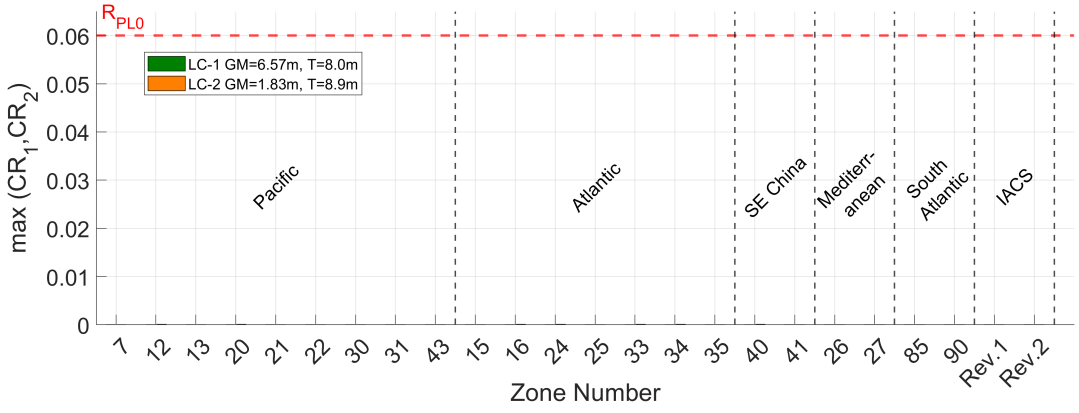

Figure 51: Pure Loss of Stability Level 2 results for D-Container across GWS zones.

Figures 52 and 53 present the Level 2 matrix results for pure loss of stability vulnerability of the D-Container vessel in Zone 20 and Zone 85. These are the same zones previously analysed for the DTC model to allow consistent comparison across sample ships.

In both zones, the D-Container shows increased vulnerability at lower GM values, following the same trend observed in the DTC case. However, unlike the DTC, the D-Container exhibits the highest vulnerability at higher drafts, around 10m. This difference is due to the hull geometry, as previously discussed in Section 4.1.2, where the D-Container shows more abrupt geometric changes at higher drafts, which result in greater variation in water plane area. Consequently, when the ship is at the crest waves, the reduction in the restoring moment becomes more severe at a higher draft for the D-Container ship. These results highlights that the response of the vessel to pure loss of stability is highly dependent on how its hull geometry varies with the draft.

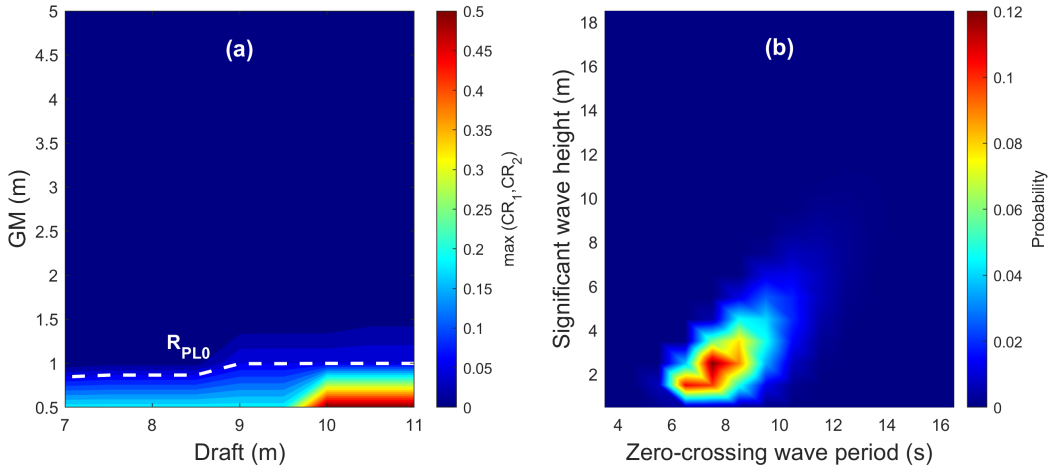

Figure 52: Zone-20: (a) Pure loss of stability Level 2 matrix results for D-Container (b) Wave scatter diagram.

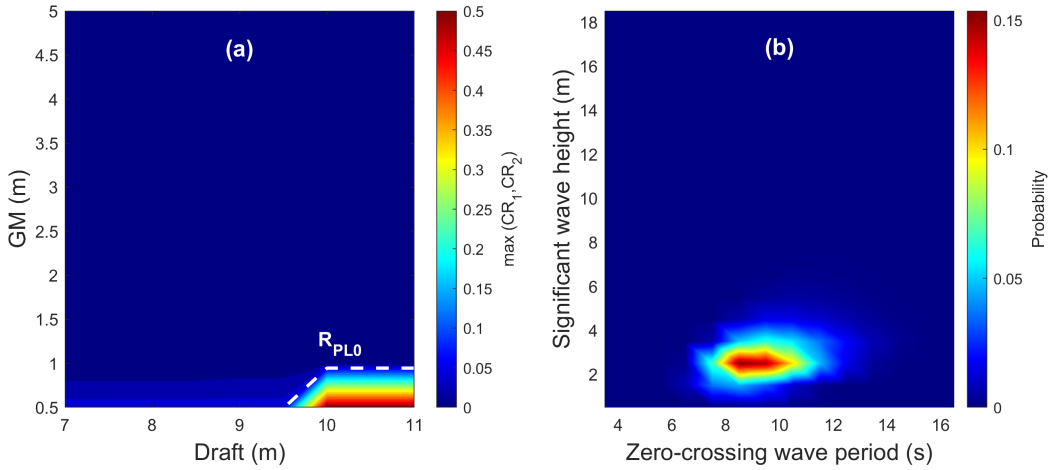

Figure 53: Zone-85: (a) Pure loss of stability Level 2 matrix results for D-Container (b) Wave scatter diagram.

4.2.3 D-Ropax

Figure 54 shows the Level 2 vulnerability index values for pure loss of stability for the D-Ropax vessel across different GWS zones. In the studied loading condition, all values remain very close to zero across all zones, indicating no significant vulnerability for this failure mode.

The IACS Rev.1 wave scatter table gives the highest value among all zones for this case, but it still remains well below the SGISC threshold ($R_{PL0} = 0.06$). Although the fixed loading condition does not indicate any risk, a more complete assessment is possible through matrix results, where the variation of GM and draft can reveal potential sensitivity not visible under a single loading condition.

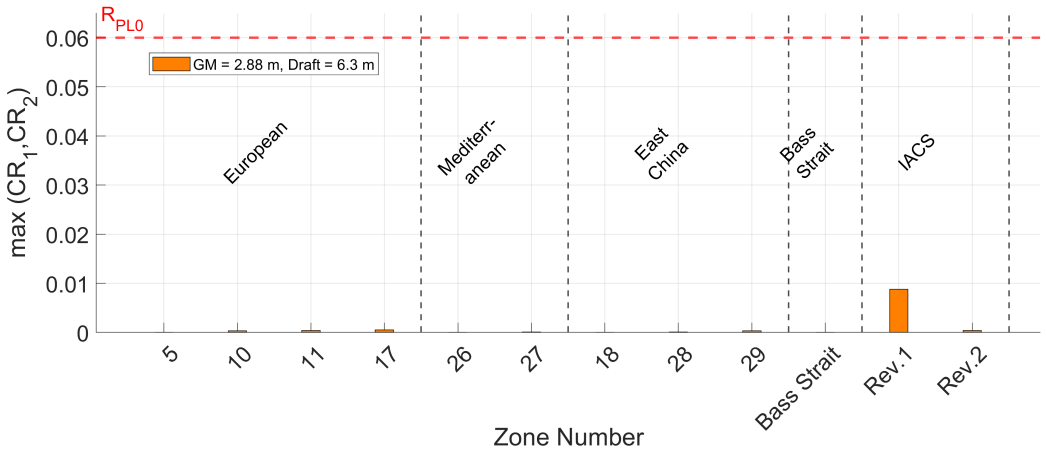

Figure 54: Pure Loss of Stability Level 2 results for D-Ropax across GWS zones.

Figures 55 and 56 show the level 2 matrix results for the pure loss of stability vulnerability of the D-Ropax vessel in Zones 17 and 26. Zone 17 was previously identified as the most vulnerable among the studied sea areas, whereas Zone 26 showed a relatively lower vulnerability in earlier analyses. Because D-Ropax is a passenger vessel, a stricter criterion is applied under the SGISC Level 2 assessment with the threshold for the wave-induced heel angle φ_{SW} is reduced to 15°, rather than 25° as used for cargo ships. This makes the D-Ropax overall more vulnerable to fail the SGISC level criteria under the same sea state conditions. Furthermore, this ship has the lowest block coefficient (C_B) among the studied ships, resulting in a finer hull form and more reduction in restoring moment in waves.

The results also confirm that vulnerability is higher at low GM values, consistent with the other sample ships. As GM increases, the vessel's restoring moment improves, which reduces the probability of failing vulnerability criteria. In terms of draft, the D-Ropax shows the highest vulnerability at lower studied drafts. This is due to hull geometry, where more abrupt change in waterpalne area occur at lower drafts. When comparing the two zones, Zone 17 shows higher vulnerability than Zone 26. This

aligns with its wave scatter diagram, which displays a broader distribution toward higher significant wave heights.

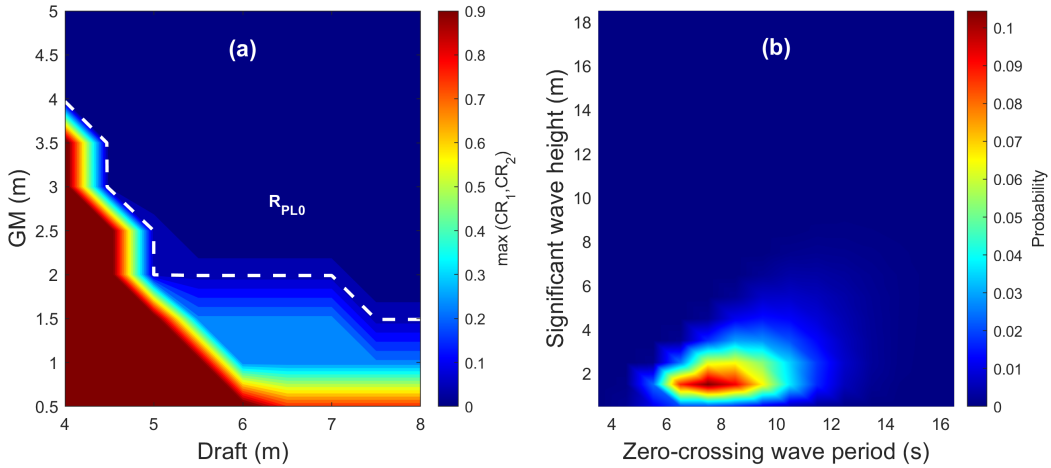

Figure 55: Zone-17: (a) Pure Loss of Stability Level 2 matrix results for D-Ropax (b) Wave scatter diagram.

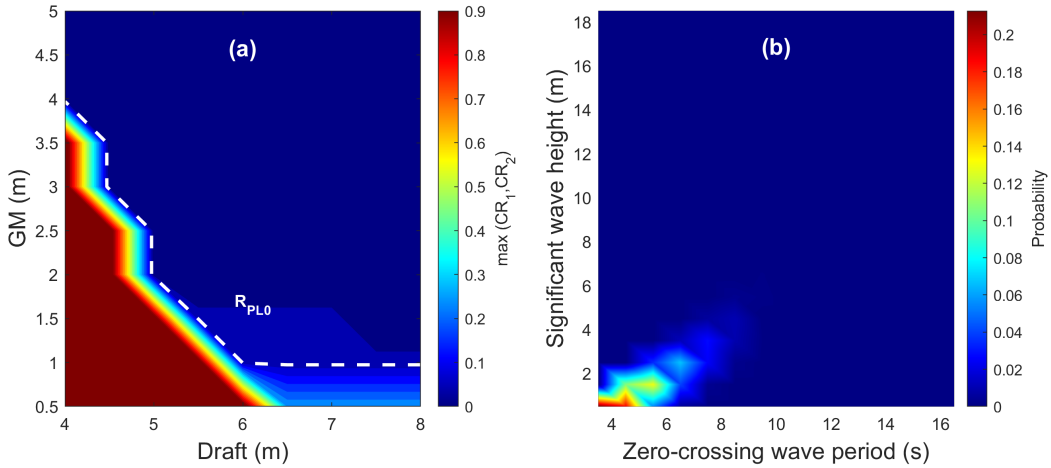

Figure 56: Zone-26: (a) Pure Loss of Stability Level 2 matrix results for D-Ropax (b) Wave scatter diagram.

4.2.4 Key Findings from the Pure Loss of Stability Assessment

The following points summarize the key factors influencing pure loss of stability vulnerability across all ships and sea zones studied.

- **GM (Metacentric Height):** Across all sample ships, the vulnerability to pure loss of stability increases significantly at low GM values. A smaller GM results in a reduced restoring moment, which reduces the ability of ship to recover from extreme rolling angles induced by external heeling. Under such conditions, the

ship is more likely to fail the Level 2 criteria, either due to a vanishing stability angle or a wave-induced heel angle exceeding the allowable threshold in Level 2 criteria.

- **Hull Geometry:** The geometry of the hull plays a major role in determining how restoring moment varies with wave conditions. Ships with finer hull forms or more abrupt geometric changes (e.g., D-Container and D-Ropax) are more sensitive to wave-induced reduction of stability. In contrast, D-Bulker showed zero vulnerability due to its fuller hull and very minimal variation in the water plane area, and was therefore excluded from the analysis for pure loss of stability as well.
- **Ship Type and Assessment Criteria:** According to the SGISC Level 2 criteria, passenger ships are subject to a stricter version of Criterion 2, where the threshold for the wave-induced heel angle (φ_{SW}) is reduced from 25° to 15°. This increases the vulnerability of passenger vessels, such as the D-Ropax, compared to cargo ships under the same environmental and loading conditions.
- **Speed:** Speed does not have a direct influence on the Level 2 vulnerability criteria, except through Criterion 2, where the heeling lever depends on the square of the Froude number. A higher speed leads to larger heeling moments, which can increase the likelihood of exceeding the threshold for wave-induced heel angle.
- **Environmental Conditions:** Zones with a higher occurrence of large significant wave heights tend to show greater vulnerability. This is because waves with higher crests passing amidships lead to a larger reduction in water plane area and righting lever. As a result, the restoring moment decreases more significantly, making it more likely for the vessel to fail the Level 2 pure loss of stability criteria. For container vessels, the Pacific Ocean zones were more vulnerable, while the IACS Rev.1 dataset consistently produced the highest vulnerability index values across all zones. In the case of the D-Ropax, the European sea zones showed the highest risk of vulnerability, with IACS Rev.1 again resulting in the maximum index values.

4.3 Excessive Acceleration

4.3.1 Duisburg Test Case

Figure 57 shows the Level 2 vulnerability index values for excessive acceleration for the DTC vessel across different GWS zones. These values represent the lateral acceleration at the navigation bridge, as defined in Section 3. In all zones, the results remain near zero and well below the SGISC threshold, indicating no vulnerability under the studied loading conditions which corresponds to relatively low GM values. However, further insight will be gained through the vulnerability matrices, where variations in GM and draft may reveal more critical combinations.

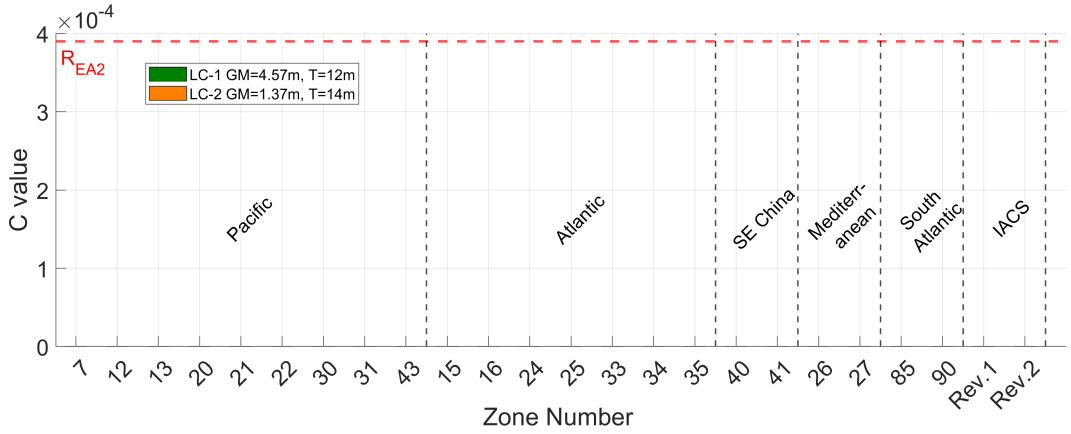

Figure 57: Excessive Acceleration Level 2 results for DTC across GWS zones.

Figures 58 and 59 show the Level 2 vulnerability matrix results for excessive acceleration for the DTC model in Zone 20 and Zone 41, respectively. These zones are selected based on the EA vulnerability analysis of D-Container to maintain consistency in evaluating the vulnerability of sample cargo ships.

As shown in the matrix, the DTC model showed no vulnerability across the full range of GM and draft combinations. The EA index values remained well below the SGISC threshold $R_{EA2} = 0.00039$ in both sea areas. This low vulnerability is largely because of high natural roll period of DTC compared to the other ships. Table 4.1 provides the roll period of all sample ships at the same GM across studied drafts. The higher roll period prevents the ship from experiencing resonance with most encountered sea states, thereby limiting roll-induced accelerations.

Although the vulnerability remains below the SGISC threshold in both zones, the results show a relative increase in index values at higher GM and draft combinations. These trends are consistent with theoretical expectations and are further discussed in the D-Container ship results section.

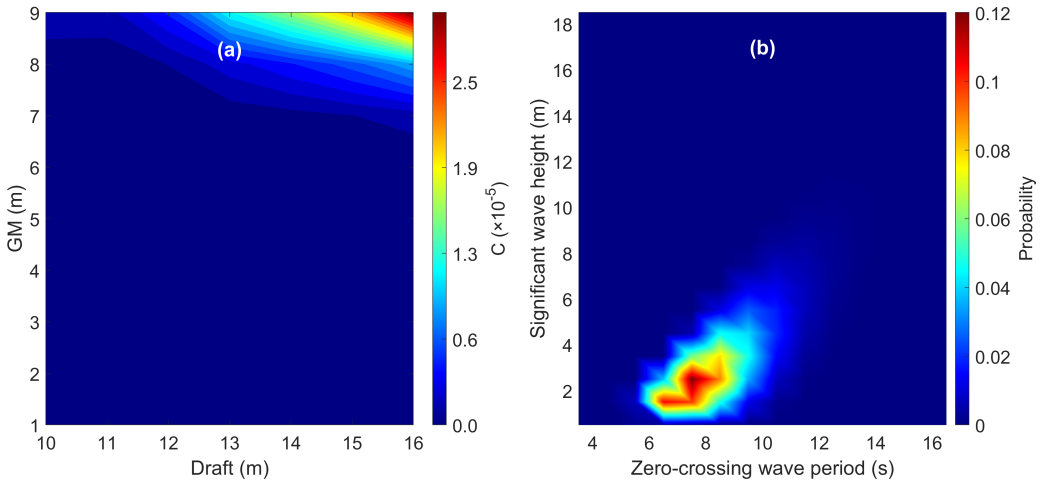

Figure 58: Zone-41 : (a) Excessive Acceleration Level 2 matrix results for DTC (b) Wave scatter diagram.

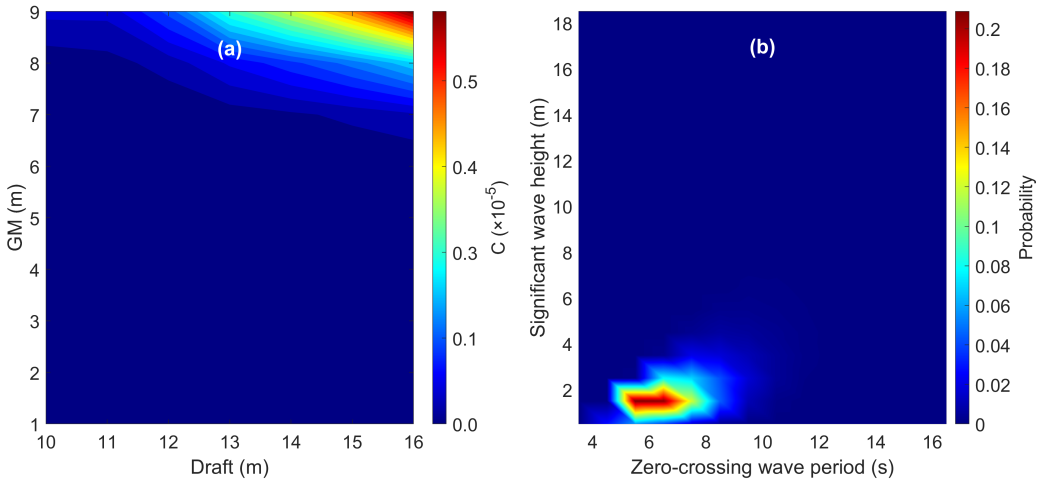

Figure 59: Zone-41 : (a) Excessive Acceleration Level 2 matrix results for DTC (b) Wave scatter diagram.

4.3.2 D-Container

Figure 60 shows the Level 2 vulnerability index values for excessive acceleration for the D-Container vessel across different GWS zones. These values represent the lateral acceleration at the navigation bridge, as defined in Section 3. In LC-2, all values remain well below the threshold (R_{EA2} = 0.00039), indicating no vulnerability in the low GM condition. In contrast, several zones show higher C values under LC-1, confirming that the vessel is vulnerable to this failure mode when operating with higher GM. This behavior aligns with the behavior of excessive acceleration, where increased GM leads to short rolling period and greater lateral accelerations at high locations on board.

The IACS Rev.1 wave scatter table produces the highest value in the dataset, clearly above the threshold. The Rev.2 value is significantly lower, remaining well below both Rev.1 and most of the other studied zones. Among the studied sea areas, the Pacific Ocean shows the highest response, with zone 20 clearly exceeding the threshold and others showing values near the limit. Some of the zones in the Atlantic and South Atlantic regions also show high responses, while the Mediterranean and Southeast China remain least vulnerable under LC-1 loading condition.

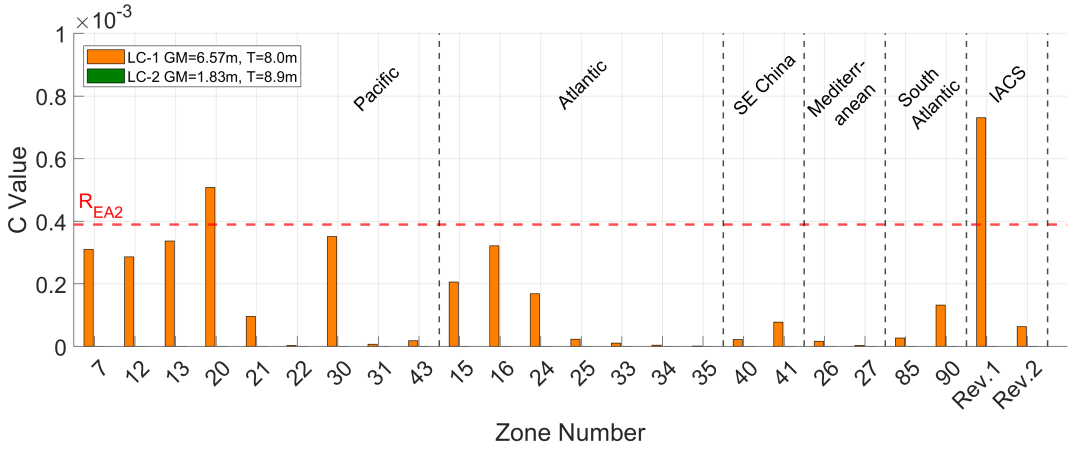

Figure 60: Excessive Acceleration Level 2 results for D-Container across GWS zones.

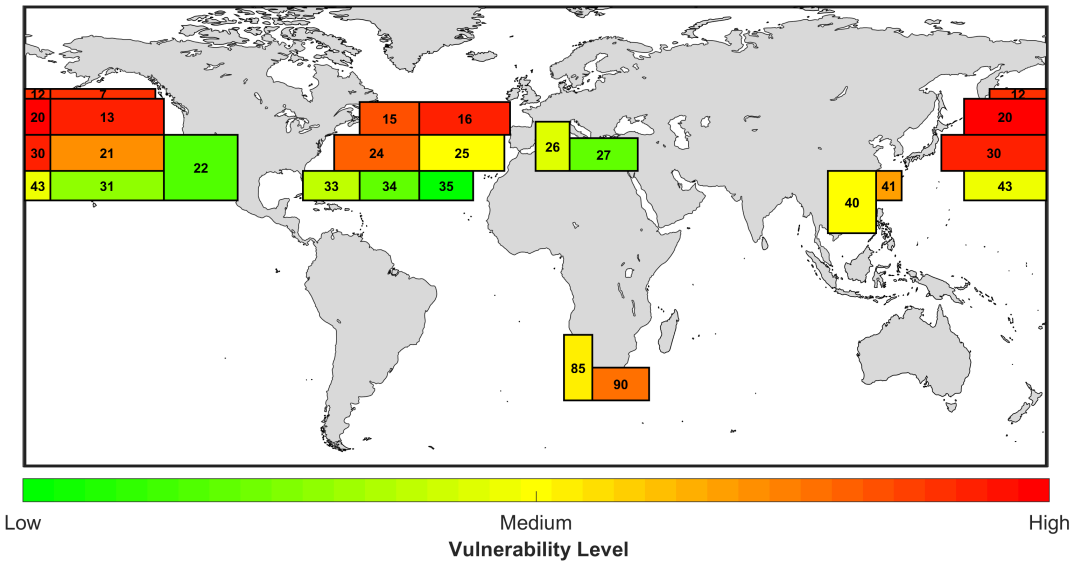

Figure 61: Excessive Acceleration vulnerability map for D-Container under LC-1

Figures 62 and 63 show the Level 2 vulnerability matrix results for excessive acceleration for the D-Container vessel in Zone 20 and Zone 41, respectively. Zone 20 was previously identified as the most vulnerable among the studied sea areas, whereas

Zone 41 showed a relatively lower vulnerability in earlier analyses. Compared to the DTC, the D-Container shows higher acceleration vulnerability partly due to its relatively short roll period across the evaluated drafts and GM values.

In Zone 20, the D-Container shows high vulnerability at high GM values, with index values exceeding the SGISC threshold $R_{EA2} = 0.00039$ particularly above GM ≈ 5 m. This trend is consistent with the theoretical expectation that higher GM results in higher roll accelerations at higher locations like the navigation bridge. At high GM, the natural roll period of the ship decreases, resulting in sharper and faster roll motions, thus increasing the lateral acceleration and ultimately leading to increased failure index values.

In terms of draft influence, at a fixed GM, vulnerability increases slightly with draft. This trend aligns with the calculated roll periods, where higher drafts give shorter roll periods for the same GM, further contributing to sharper roll responses and hence higher acceleration. In Zone 41, a similar pattern is observed, but the vulnerability is notably lower than in Zone 20. The index values in this zone remain below the threshold for almost all draft-GM combinations. This difference is well justified by the wave scatter diagram, as Zone 41 shows a lower frequency of extreme sea states compared to Zone 20.

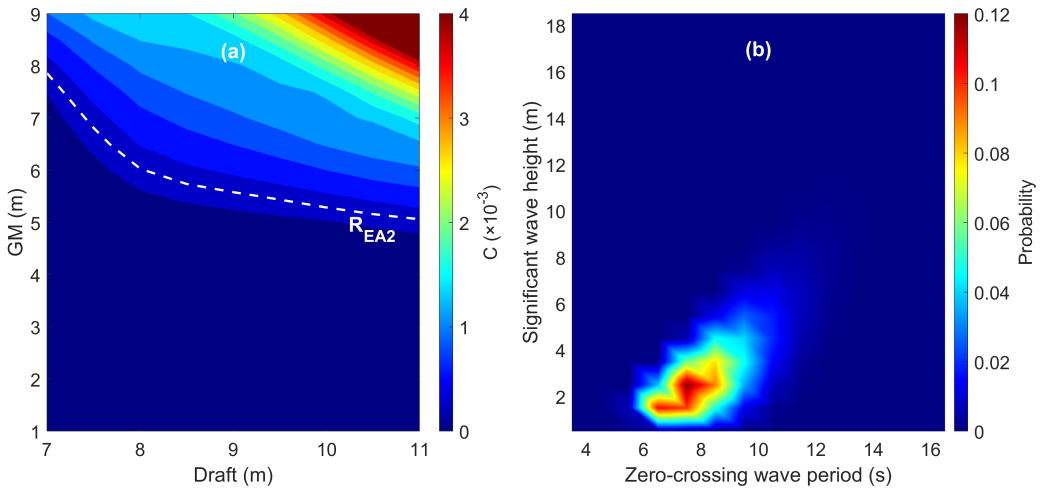

Figure 62: Zone-20 : (a) Excessive Acceleration Level 2 matrix results for D-Container (b) Wave scatter diagram.

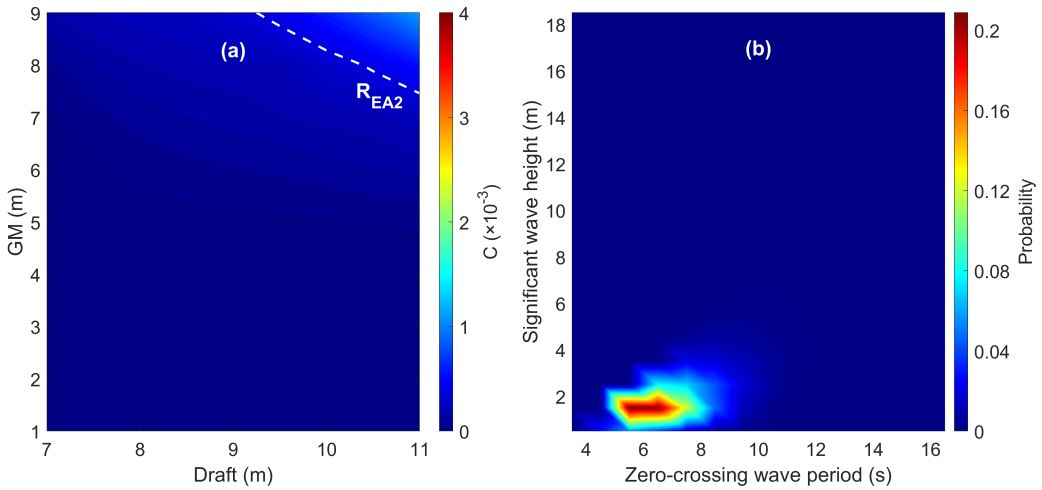

Figure 63: Zone-41 : (a) Excessive Acceleration Level 2 matrix results for D-Container (b) Wave scatter diagram.

4.3.3 D-Bulker

Figure 64 shows the Level 2 vulnerability index values for excessive acceleration for the D-Bulker vessel across different GWS zones. These values represent the lateral acceleration at the navigation bridge, as defined in Section 3. Unlike in the other failure modes, this vessel shows significant vulnerability under LC-2, where the GM is high. In LC-1, the values are close to zero in all zones. However, in LC-2, many zones exceed the SGISC threshold (R_{EA2} = 0.00039), indicating that the vessel is vulnerable to this failure mode when operating with high transverse stability. This is consistent with the expected behavior of excessive acceleration with high GM value.

In the Bulk carrier, IACS Rev.1 wave scatter table also gives the highest value in the dataset, clearly above the threshold. The Rev.2 result is lower than Rev.1 but still above the R_{EA2}. In the Pacific Ocean, more than half of the zones show values well above the threshold, confirming this region as the most critical for this failure mode too. Several zones in the Atlantic and South Atlantic also exceed the threshold, indicating widespread vulnerability in these areas as well. Notably, the Southeast China Sea, which was not vulnerable in other failure modes, shows values above the threshold in this case. In the Mediterranean region, Zone 26 remains below the threshold but is close to the limit, indicating a moderate level of risk in this region too.

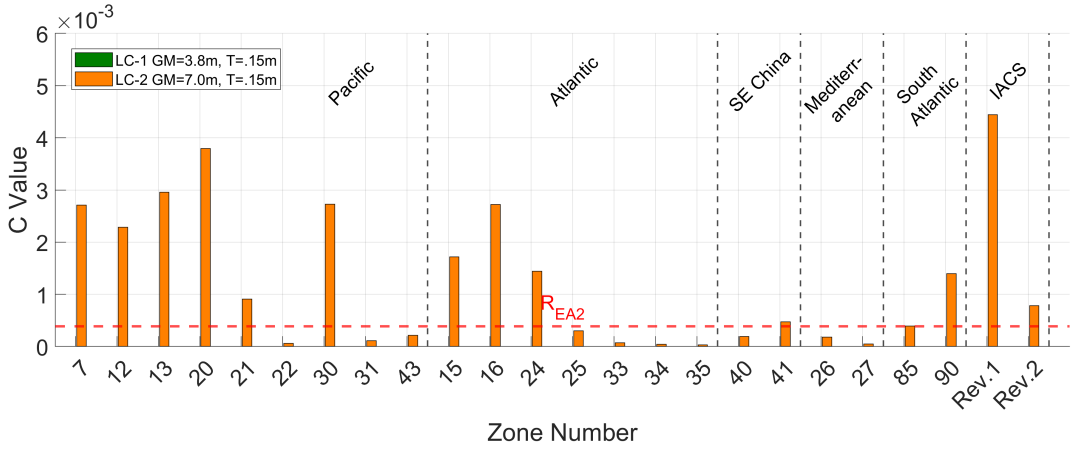

Figure 64: Excessive Acceleration Level 2 results for D-Bulker across GWS zones.

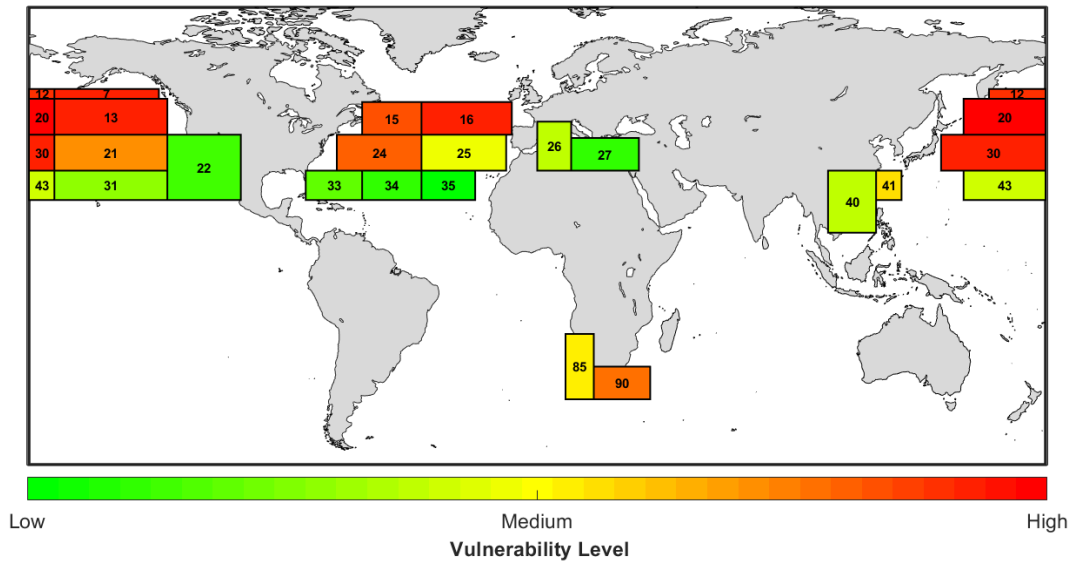

Figure 65: Excessive Acceleration vulnerability map for D-Bulker under LC-1

Figures 66 and 67 present the Level 2 vulnerability matrix results for excessive acceleration for the D-Bulker ship in Zone 20 and Zone 41, respectively. The same sea areas as the D-Container and DTC are selected for consistency among the cargo ship categories.

Zone 20 reveals significant vulnerability at higher GM values, with a notable portion of the operating range exceeding the SGISC threshold $R_{EA2} = 0.00039$. The observed pattern is similar to that of the D-Container, where increased GM leads to reduced roll period and sharper roll motions, thus amplifying the lateral accelerations at navigation bridge. For draft, the results follow the expected behavior, with a fixed GM, higher drafts slightly increase vulnerability.

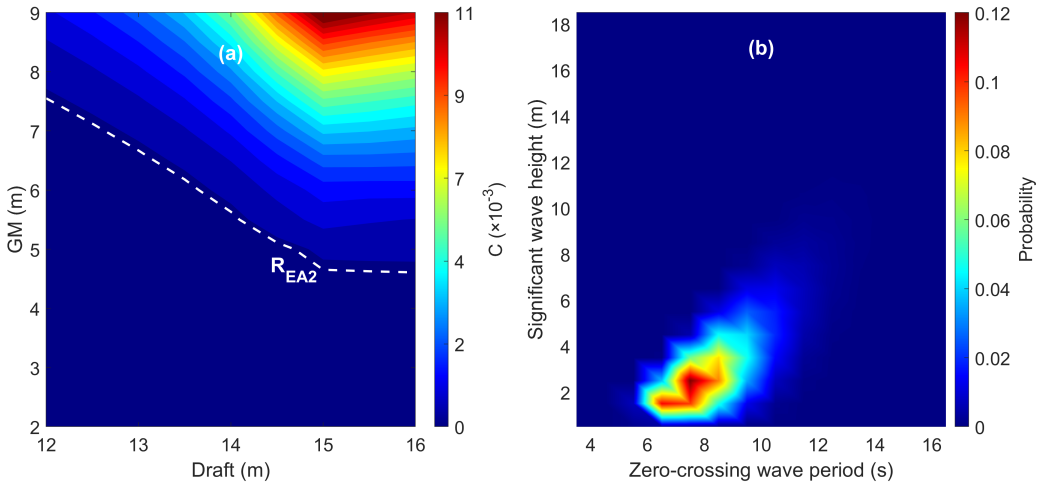

Figure 66: Zone-20 : (a) Excessive Acceleration Level 2 matrix results for D-Bulker (b) Wave scatter diagram.

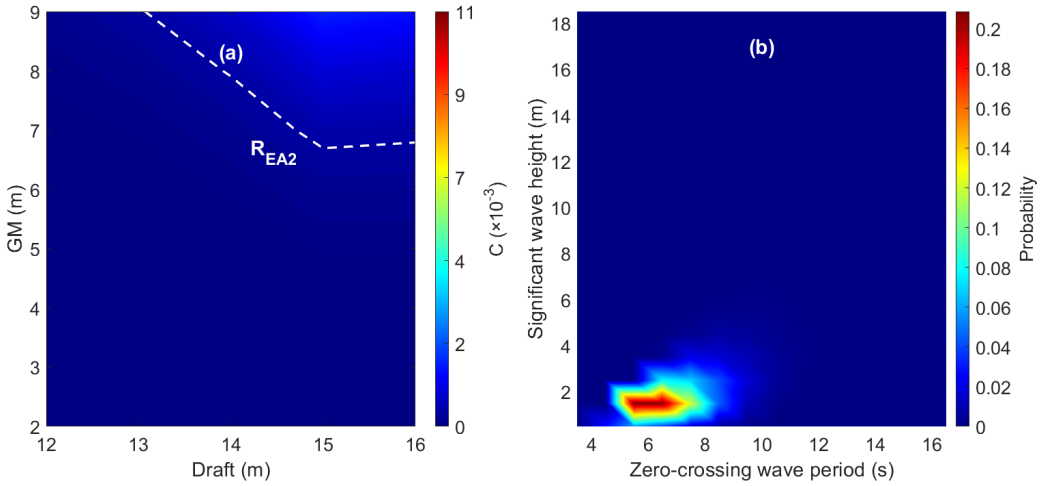

Figure 67: Zone-41 : (a) Excessive Acceleration Level 2 matrix results for D-Bulker (b) Wave scatter diagram.

4.3.4 D-Ropax

Figure 68 shows the Level 2 vulnerability index values for excessive acceleration for the D-Ropax vessel across different GWS zones. The vulnerability assessment is performed for all four selected locations on board as described in Section 3. The maximum values are obtained at the highest location, i.e., the navigation bridge. Therefore, all reported results in this section correspond to that location. In all zones, the results remain near zero and well below the SGISC threshold, indicating no vulnerability under the low GM. However, further insight will be gained through the vulnerability matrices, where variations in GM and draft may reveal more critical combinations.

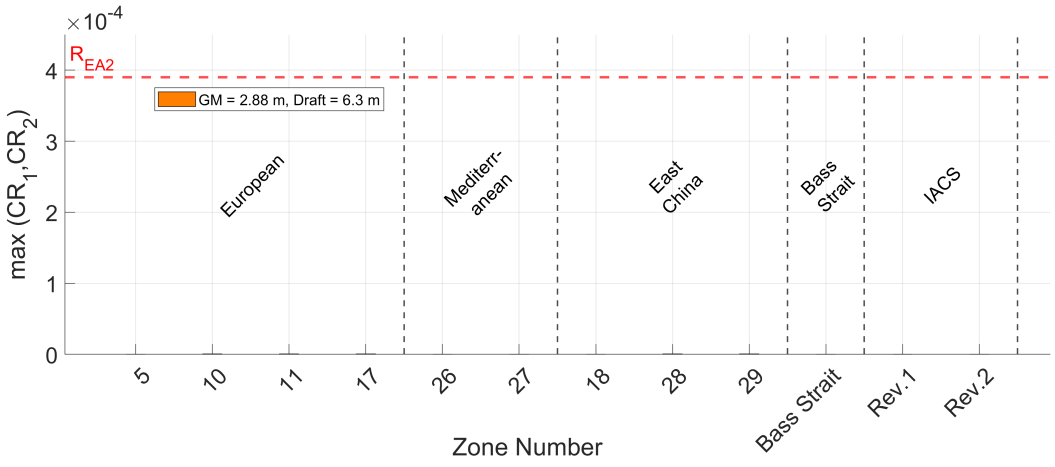

Figure 68: Excessive Acceleration Level 2 results for D-Ropax across GWS zones.

Figures 69 and 70 present the Level 2 vulnerability matrix results for excessive acceleration for the D-Ropax vessel in Zone 17 and Zone 26, respectively. Both zones gave relatively low vulnerability, with the computed index values mostly staying below the SGISC threshold.

One factor is the relatively high natural roll period of the D-Ropax, which reduces the amplitude of roll accelerations under the encountered wave conditions. Additionally, the selected operational zones for the D-Ropax vessel are less extreme in wave environment compared to zones analyzed for cargo vessels.

The similar trend with respect to GM is followed for D-Ropax. However, the draft dependency shows an inverse trend compared to the other ships. For D-Ropax, higher vulnerability is observed at lower drafts. This behavior is attributed to reduced roll damping at lower drafts, where the block coefficient is very low[17].A smaller underwater volume decreases hydrodynamic damping forces, allowing larger angular accelerations to develop under wave , even if the roll period remains relatively long. When results were checked beyond 8 m draft, higher drafts showed greater vulnerability, confirming that lower drafts with lowest C_B reduce damping and increase index value.

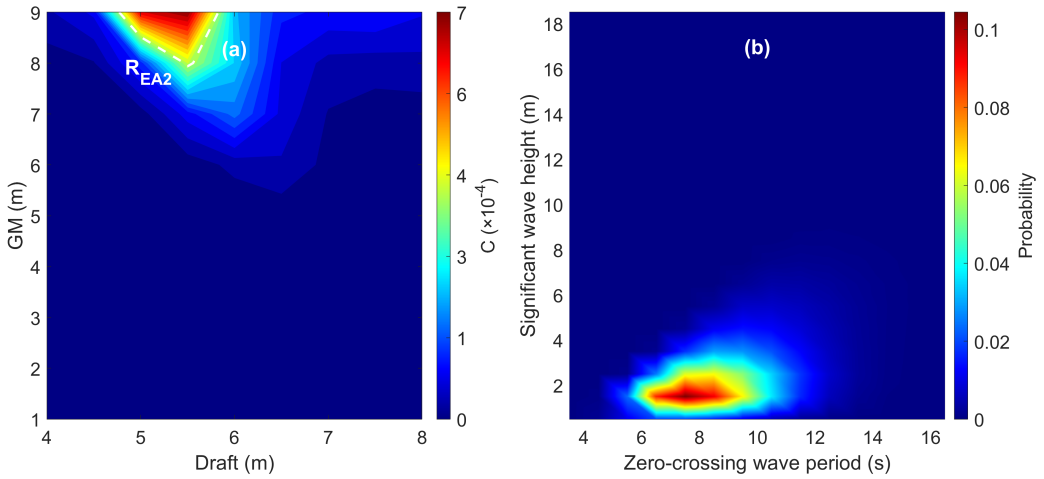

Figure 69: Zone-17 : (a) Excessive Acceleration Level 2 matrix results for D-Ropax (b) Wave scatter diagram.

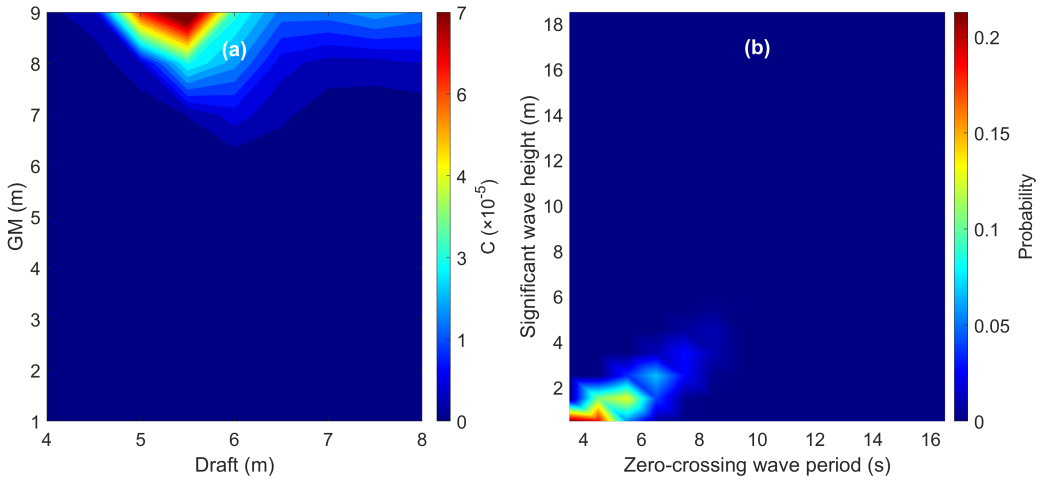

Figure 70: Zone-26 : (a) Excessive Acceleration Level 2 matrix results for D-Ropax (b) Wave scatter diagram.

4.3.5 Key Findings from the Excessive Acceleration Assessment

The following findings summarize the critical aspects influencing excessive acceleration vulnerability across all ships:

- **Roll Period:** The overall excessive acceleration vulnerability mainly depends on roll period of each ship. Figure 71 compares roll periods at GM = 7 m across all ships. The DTC and D-Ropax with the longest roll period, showed the lowest vulnerability, while the D-Container and D-Bulker, with shorter roll periods, are more prone to this failure.

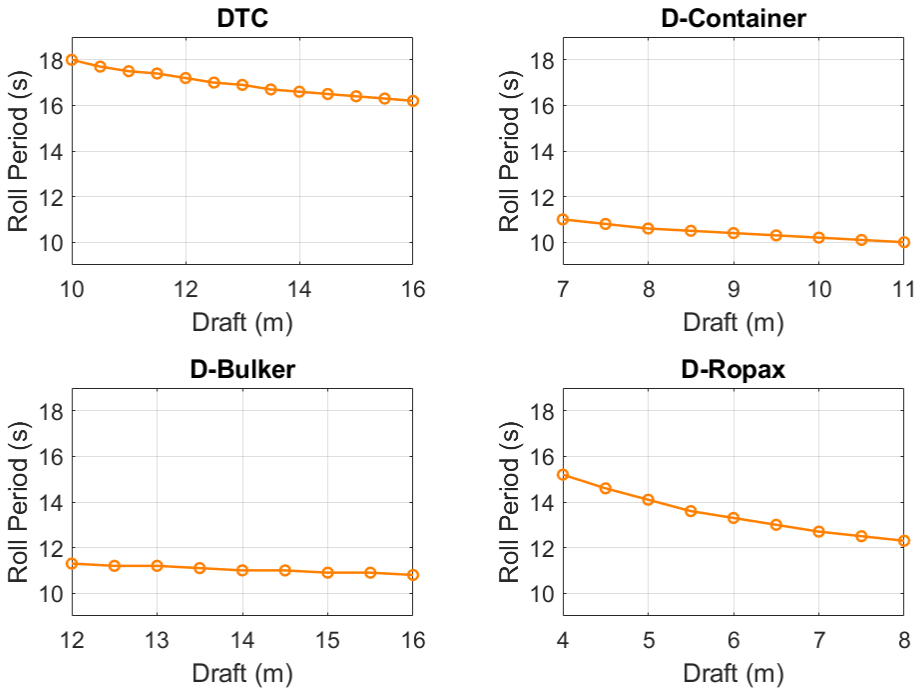

Figure 71: Roll period vs draft comparison at GM = 7 m for all sample ships

- **Metacentric Height (GM):** In all ships, excessive acceleration vulnerability increased with higher GM values. This is due to the associated reduction in natural roll period, which results faster roll motions. Higher accelerations at short periods raise the index value defined in the SGISC Level 2 criterion.
- **Draft Influence:** For most studied ships, increasing draft at fixed GM led to higher acceleration vulnerability. This behavior is consistent with the trend of decreasing roll period at higher drafts, resulting in steeper roll acceleration. The effect was especially evident for the D-Container and D-Bulker vessels.
- **Hull Form and Damping Considerations:** Ships with finer hull forms experience lower hydrodynamic roll damping, particularly at low drafts.[17] This contributes to sharper roll responses and greater lateral accelerations, explaining the unexpected vulnerability behavior observed in the D-Ropax at lower drafts.
- **Environmental Conditions:** Similar to the other SGISC failure modes, the environmental conditions have a notable impact on the results of excessive acceleration vulnerability. In EA assessment, the IACS Rev.1 wave scatter table again showed higher index values compared to other zones. Among the regional zones, the Pacific Ocean zones consistently resulted in the highest EA index values. This trend aligns with the findings for other failure modes.

4.4 Summary of SGISC Vulnerability Results

Table 14 shows that most of the studied ship types satisfy the SGISC criteria under their defined loading conditions using the standard Rev.1 wave scatter table. The D-RoPax vessel does not meet the pure loss of stability criterion at its loading condition, but since all RoPax operating zones pass the vulnerability check, the vessel can operate without changes to its design or loading condition. This is in line with SGISC guidelines, which allow the ships to sail with operational limitations if the ship fails the criteria. In contrast, both the D-Container and D-Bulker failed the excessive acceleration criterion, and several sea zones also exceeded the threshold. Therefore, to operate in those non-compliant zones, weather routing must be applied, or the ship's design or loading condition must be modified as per SGISC guidelines.

Table 14: SGISC Vulnerability Assessment for all sample ships at loading conditions

Sample Ship	Loading Condition	Failure Mode	Rev.1 Value	Threshold Value	Vulnerability Status
DTC	LC-1	PR	0	0.025	Pass
DTC	LC-2	PR	0.007	0.025	Pass
DTC	LC-1	PLS	0	0.060	Pass
DTC	LC-2	PLS	0.019	0.060	Pass
DTC	LC-1	EA	0	0.00039	Pass
DTC	LC-2	EA	0	0.00039	Pass
D-Container	LC-1	PR	0	0.025	Pass
D-Container	LC-2	PR	0.01	0.025	Pass
D-Container	LC-1	PLS	0	0.060	Pass
D-Container	LC-2	PLS	0	0.060	Pass
D-Container	LC-1	EA	0.001	0.00039	Fail
D-Container	LC-2	EA	0	0.00039	Pass
D-Ropax	LC-1	PR	0.028	0.025	Fail
D-Ropax	LC-1	PLS	0.008	0.060	Pass
D-Ropax	LC-1	EA	0	0.00039	Pass
D-Bulker	LC-1	PR	-	0.025	Pass
D-Bulker	LC-2	PR	-	0.025	Pass
D-Bulker	LC-1	PLS	-	0.060	Pass
D-Bulker	LC-2	PLS	-	0.060	Pass
D-Bulker	LC-1	EA	0.0044	0.00039	Fail
D-Bulker	LC-2	EA	0.0001	0.00039	Pass

In addition to loading condition analysis, each ship type is evaluated over a range of GM and draft values to identify critical loading conditions. Table 15 summarizes the most vulnerable zones for each failure mode and ship type. The results show that the D-RoPax vessel, due to its finer hull form, is the most vulnerable to pure loss of stability and parametric rolling. In contrast, the D-Bulker showed no vulnerability in these failure modes, attributed to its fuller hull form. For excessive acceleration, the

D-Container and D-Bulker are more vulnerable, primarily due to their shorter natural roll periods.

Table 15: Summary of SGISC-based vulnerability assessments in a critical zone

Sample Ship	Failure Mode	Critical Zone	Critical GM (m)	Critical Draft (m)	Overall Vulnerability
DTC	PR	13	< 1.0	10–12	Moderate
D-Container	PR	13	< 1.0	10	Moderate
D-Ropax	PR	17	< 3.0	4–5	High
D-Bulker	PR	-	-	-	No
DTC	PLS	20	< 1.0	10–12	Moderate
D-Container	PLS	20	< 1.0	9–11	Moderate
D-Ropax	PLS	17	< 4.0	4–5	High
D-Bulker	PLS	-	-	-	No
DTC	EA	20	-	-	Low
D-Container	EA	20	> 5	7–9	High
D-Ropax	EA	17	> 8	5–6	Moderate
D-Bulker	EA	20	> 4.5	12–14	High

Figures 72 and 73 present the global vulnerability maps for different ship types and failure modes. Although the levels of vulnerability for zones varied slightly across ship types, a general pattern remained the same. Pacific zones tend to be more vulnerable for cargo vessels, whereas European zones show higher vulnerability in RoPax operations.

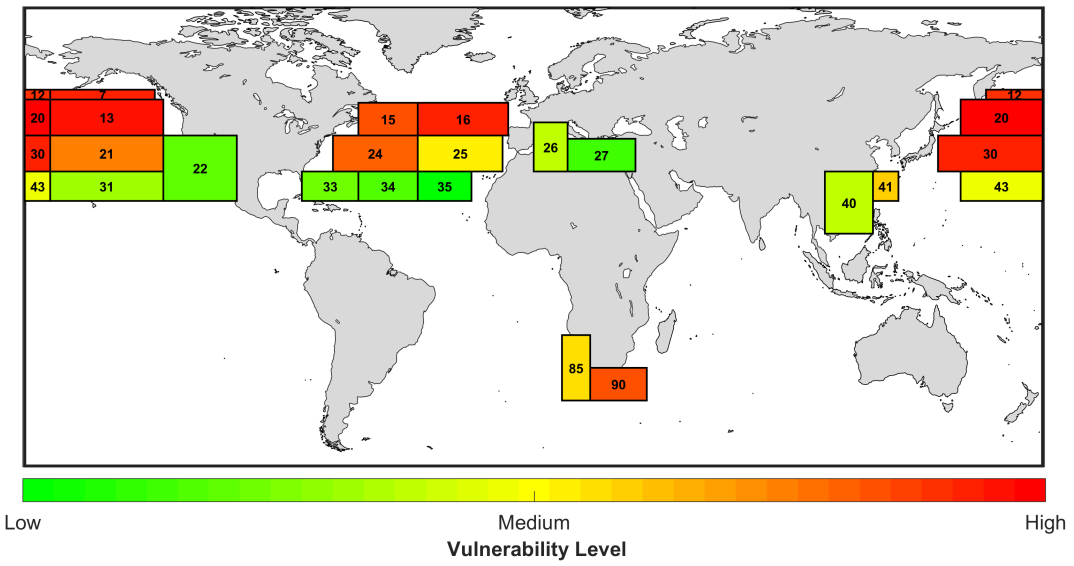

Figure 72: General vulnerability zones map for studied cargo ships across all studied failure modes

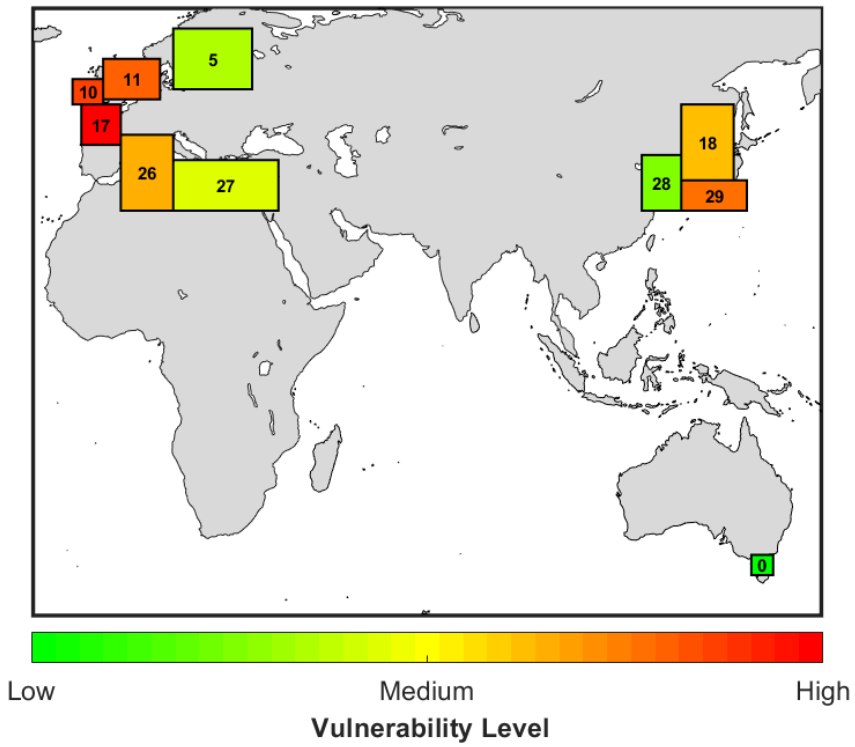

Figure 73: General vulnerability zones map for the D-RoPax vessel across all studied failure modes

5 Conclusion

This thesis investigated the vulnerability of ships to dynamic stability failures as defined by the Second Generation Intact Stability Criteria by applying Level 2 criteria. The purpose of this study is to address the limitation of standard SGISC wave scatter table (WST) which is derived from IACS Recommendation No. 34/Rev.1. A key motivation for this study is to check the applicability of SGISC, which allows unrestricted global operation once a ship passes the vulnerability check using the standard North Atlantic wave scatter table. However, it remains uncertain whether such ships would remain not vulnerable in other global sea areas. Therefore, this study applied hindcast-based scatter tables across different Global Wave Statistics (GWS) zones to evaluate three failure modes across four sample ships and compare the results against standard wave scatter table.

Based on the results of the vulnerability assessments across the studied failure modes and ship types, the main findings are presented below:

- Standard WST data consistently gave the highest vulnerability index values across all studied failure modes and ship types. This confirms the conservative nature of Rev.1 and confirms its applicability for global unrestricted operations if a ship passes this standard wave scatter data.
- Rev.2 wave data, introduced by IACS Recommendation No. 34/Rev.2, produced lower vulnerability index values, even lower than many other GWS zones.
- Among the zones selected based on cargo ship routes, those located in the Pacific region showed higher vulnerability results in all failure modes, followed by Atlantic zones.
- For the ropax routes, the selected zones showed lower vulnerability compared to standard WST and other high vulnerable GWS zones. In some cases, the D-Ropax passed the criteria in these zones despite not meeting under Standard WST, indicating that ship can sail without restrictions in those areas as per SGISC guidelines.

The following points are suggested as future recommendations to further extend this study:

- Instead of annual wave data, season-specfic wave data may be used to study the effect of seasonality on SGISC vulnerability results.
- Extend the analysis to include a more ship types and using design input data from real-world vessels to improve the accuracy of results.
- Instead of using average wave statistics zone data, use of weather route-specific hindcast wave data can give more ship operationally relevant assessment results.
- Investigate the influence of varying bilge keel dimensions, trim conditions, and damping effects on vulnerability outcomes.

References

[1] H. Nowacki, "Archimedes and ship design," in *Archimedes in the 21st Century: Proceedings of a World Conference at the Courant Institute of Mathematical Sciences*. Springer, 2017, pp. 77–112.

[2] J. Rahola, *The Judging of the Stability of Ships and the Determination of the Minimum Amount of Stability–Especially Considering the Vessels Navigating Finnish Waters*. Aalto University, 1939.

[3] A. Francescutto, "Intact stability criteria of ships–past, present and future," *Ocean Engineering*, vol. 120, pp. 312–317, 2016.

[4] A. Francescutto, A. Serra, and S. Scarpa, "The development of second generation intact stability criteria," in *Sustainable Development and Innovations in Marine Technologies*. CRC Press, 2019.

[5] M. A. Neves, "Dynamic stability of ships in regular and irregular seas-an overview," *Ocean engineering*, vol. 120, pp. 362–370, 2016.

[6] E. Begovic, C. Bertorello, B. Rinauro, and G. Rosano, "Simplified operational guidance for second generation intact stability criteria," *Ocean Engineering*, vol. 270, p. 113583, 2023.

[7] J. Paulling, S. Kastner, and S. Schaffran, "Experimental studies of capsizing of intact ships in heavy seas. us coast guard," Tech Rep (Also IMO Doc. STAB/7, 1973), Tech. Rep., 1972.

[8] O. Oakley, "Ship motions and capsizing in astern seas," in *Proceedings of the 10th Naval Hydro-dynamics Symposium*, 1974, pp. 1–51.

[9] International Maritime Organization (IMO), "Code on Intact Stability for All Types of Ships Covered by IMO Instruments, Resolution A.749(18)," Assembly Resolution A.749(18), International Maritime Organization, 4 November 1993.

[10] K. Spyrou and A. Papanikolaou, "Ship design for dynamic stability," in *Proceedings of the 7th International Marine Design Conference, Kyongju, Korea*, 2000, pp. 21–24.

[11] F. Grinnaert, "Analysis and implementation of second generation criteria in a stability computer code," Ph.D. dissertation, Université de Bretagne occidentale-Brest, 2017.

[12] L. Pérez Rojas, S. Sastre, and A. Martín Landaluce, "Review of the ship accidents investigations presented at the stab," 2008.

[13] M. Taylan, "Anatomy of a capsize: Then and now," in *8th International Ship Stability Workshop (ISSW 2005), Istanbul*, 2005.

[14] International Maritime Organization (IMO), "Adoption of the International Code on Intact Stability, 2008 (2008 IS Code), Resolution MSC.267(85)," MSC

Resolution MSC.267(85), International Maritime Organization, December 2008, adopted on 4 December 2008.

[15] A. Francescutto, A. Serra, and S. Scarpa, "A critical analysis of weather criterion for intact stability of large passenger vessels," in *Sustainable Development and Innovations in Marine Technologies*. Sonopress-Ritmo Industria e Comércio Ltda, 2001.

[16] A. Francescutto and N. Umeda, "Current status of new generation intact stability criteria development," in *Proceedings of the 11th International Ship Stability Workshop, Wageningen, The Netherlands*, vol. 2010, 2010, pp. 21–23.

[17] N. Petacco, "Second generation intact stability criteria: Analysis, implementation and applications to significant ship typologies," Ph.D. dissertation, Università degli studi di Genova, 2019.

[18] International Maritime Organization (IMO), "1/circ. 1228 revised guidance to the master for avoiding dangerous situations in adverse weather and sea conditions," *International Maritime Organization, London*, 2007.

[19] T. Manderbacka, N. Themelis, I. Bačkalov, E. Boulougouris, E. Eliopoulou, H. Hashimoto, D. Konovessis, J.-F. Leguen, M. M. González, C. A. Rodríguez *et al.*, "An overview of the current research on stability of ships and ocean vehicles: The stab2018 perspective," *Ocean Engineering*, vol. 186, p. 106090, 2019.

[20] M. Tompuri, P. Ruponen, M. Forss, and D. Lindroth, "Application of the second generation intact stability criteria in initial ship design," in *SNAME Maritime Convention*. SNAME, 2014, p. D011S001R003.

[21] J. Chung, D. M. Shin, W.-D. Kim, and B. Y. Moon, "Current status of the 2nd generation of intact stability: Investigation of the pure loss of stability and parametric roll mode," *Journal of Ocean Engineering and Technology*, vol. 34, no. 2, pp. 55–65, 2020.

[22] V. Belenky, C. Bassler, and K. Spyrou, "Development of second generation intact stability criteria," *Hydromechanics Department Report, Naval Surface Warfare Center Carderock Division-50-TR-2011/065*, 2011.

[23] M. Tompuri, P. Ruponen, and D. Lindroth, "On the consistency of the level 1 and 2 vulnerability criteria in the second generation intact stability," in *Proceedings of ISSW*, 2017, pp. 3–8.

[24] International Maritime Organization (IMO), "Interim guidelines on the second generation intact stability criteria," MSC.1/Circ.1627, International Maritime Organization, December 2020, adopted at the 102nd session of the Maritime Safety Committee (4–11 November 2020). [Online]. Available: https://wwwcdn.imo.org/localresources/en/OurWork/Safety/Documents/MSC.1-Circ.1627.pdf

[25] K. E. Marlantes, S. Kim, and L. A. Hurt, "Implementation of the IMO second generation intact stability guidelines," *Journal of Marine Science and Engineering*, vol. 10, no. 1, p. 41, 2021.

[26] H. Hashimoto and K. Furusho, "Influence of sea areas and season in navigation on the ship vulnerability to the parametric rolling failure mode," *Ocean Engineering*, vol. 266, p. 112714, 2022.

[27] G. Bulian and A. Orlandi, "Effect of environmental data uncertainty in the framework of second generation intact stability criteria," *Ocean Engineering*, vol. 253, p. 111253, 2022.

[28] N. Hogben, "Global wave statistical," *British Maritime Technology*, 1986.

[29] International Association of Classification Societies, "Recommendation no. 34 (rev.1) – standard wave data," International Association of Classification Societies (IACS), June 2000.

[30] H. N. Austefjord, G. de HAUTECLOCQUE, M. Johnson, and T. Zhu, "Update of wave statistics standards for classification rules," in *Advances in the Analysis and Design of Marine Structures*. CRC Press, 2023, pp. 43–52.

[31] G. de Hauteclocque, N. V. Maretic, and Q. Derbanne, "Hindcast based global wave statistics," *Applied Ocean Research*, vol. 130, p. 103438, 2023.

[32] W. Fujimoto, K. Ishibashi, and T. Zhu, "Analyzing AIS and wave hindcast data for global wave scatter diagrams with seasonality," *Ocean Engineering*, vol. 314, p. 119647, 2024.

[33] S. Mangalathu Raj, H. Enshaei, and N. Abdussamie, "Standard wave scatter table limitation for evaluating sgisc based on hindcast data analysis," *Applied Sciences*, vol. 13, no. 2, p. 1181, 2023.

[34] "Review of incidents resulting in loss of containers," MARIN (Maritime Research Institute Netherlands), Tech. Rep. 33039-1-SEA, May 2022, final Report. Available: https://www.marin.nl/en/jips/toptier.

[35] International Maritime Organization, "Explanatory notes to the interim guidelines on the second generation intact stability criteria," MSC.1/Circ.1652, International Maritime Organization (IMO), April 2023, approved at the 105th session of the Maritime Safety Committee. [Online]. Available: https://wwwcdn.imo.org/localresources/en/OurWork/Safety/Documents/MSC.1-Circ.1652%20-%20Explanatory%20Notes%20On%20The%20Second%20Generation%20Intact%20Stability%20Criteria%20(Secretariat).pdf

[36] K. Takeda, M. Akagi, and K. Ishibashi, "Introduction of "guidelines on preventive measures againts parametric rolling"," *ClassNK Technical Journal*, vol. 7, pp. 13–21, 2023.

[37] MAN Energy Solutions, "Propulsion trends in container vessels," MAN Energy Solutions, Tech. Rep., 2023, accessed: 16-May-2025. [Online]. Available:

https://www.man-es.com/docs/default-source/marine/tools/propulsion-trends-in-container-vessels.pdf?sfvrsn=c48bba16_12

[38] O. e. Moctar, V. Shigunov, and T. Zorn, "Duisburg test case: Post-panamax container ship for benchmarking," *Ship Technology Research*, vol. 59, no. 3, pp. 50–64, 2012.

[39] MAN Energy Solutions, "Propulsion trends in bulk carriers," MAN Energy Solutions, Tech. Rep., 2023, accessed: 16-May-2025. [Online]. Available: https://www.man-es.com/docs/default-source/document-sync/propulsion-trends-in-bulk-carriers-eng.pdf

[40] B. Jacobsen, "Propulsion Trends in Bulk Carriers," *Gazette–Royal Belgian Institute of Marine Engineers*, 2015, available online: https://gallois.be/ggmagazine_2015/gg_02_03_2015_64.pdf.

[41] K. Jivén, R. Parsmo, E. Fridell, J. Hansson, H. Lundström, P. Wimby, J. Burgren, K. Koosup Yum, and D. Stenersen, "Concept design and environmental analysis of a fuel cell ropax vessel-report in the hope (hydrogen fuel cells solutions in shipping in relation to other low carbon options) project," 2023.

[42] L. Gucma and J. Raczkowska, "An analysis of basic parameters of ro-pax ferries in the baltic sea as guidelines for its preliminary design," *Polish Maritime Research*, no. 3, pp. 44–53, 2018.

[43] R. Grin, "On empirical methods to predict the rolling period of ships," in *International Marine Design Conference*, 2024.

[44] International Maritime Organization, "Alternative Roll Period Formula to be used for the Second Generation Intact Stability Criteria, Submitted by Japan," MSC 108/INF.7, 2024, international Maritime Organization.

[45] P. Ruponen, E. Altintas, J. Matusiak, and T. Mikkola, "A practical approach for simplified operational guidance to avoid parametric roll resonance," *Ocean Engineering*, vol. 330, p. 121215, 2025.

[46] Japan Transport Safety Board, "Marine Accident Investigation Report: Container Ship ONE APUS (IMO No. 9806079)," Japan Transport Safety Board, Tokyo, Japan, Tech. Rep. MA2024-02, February 2024. [Online]. Available: https://jtsb.mlit.go.jp/eng-mar_report/2024/2022tk0001e.pdf

[47] U. Gunes, "Estimating bulk carriers' main engine power and emissions," *Brodogradnja: An International Journal of Naval Architecture and Ocean Engineering for Research and Development*, vol. 74, no. 1, pp. 85–98, 2023.

[48] International Association of Classification Societies (IACS), "Bulk carriers: Guidance and information on dry cargo loading and discharging to reduce the likelihood of over-stressing the hull structure," https://https://iacs.org.uk/resolutions/recommendations/41-60/rec-46-rev2-cln/, 2020, revision 2, January 2020.

[49] P. Kacprzak, "Stability evaluation during loading simulation of bulk carriers in the clarion-clipperton zone using a modified weather criterion," *80 Scientific Journals of the Maritime University of Szczecin*, no. 80, 2024.

[50] E. M. Bitner-Gregerse, C. G. Soares, and M. Vantorre, "Adverse weather conditions for ship manoeuvrability," *Transportation Research Procedia*, vol. 14, pp. 1631–1640, 2016.

[51] U. D. Nielsen and A. Ikonomakis, "Wave conditions encountered by ships—a report from a larger shipping company based on era5," *Ocean Engineering*, vol. 237, p. 109584, 2021.

[52] G. de Hauteclocque, T. Zhu, M. Johnson, H. Austefjord, and E. Bitner-Gregersen, "Assessment of global wave datasets for long term response of ships," in *International Conference on Offshore Mechanics and Arctic Engineering*, vol. 84324. American Society of Mechanical Engineers, 2020, p. V02AT02A026.

[53] H. N. Austefjord, G. de HAUTECLOCQUE, M. Johnson, and T. Zhu, "Update of wave statistics standards for classification rules," in *Advances in the Analysis and Design of Marine Structures*. CRC Press, 2023, pp. 43–52.

[54] International Maritime Organization (IMO), "Comments on the review of the North Atlantic wave data," MSC 108/19, Submitted by ICS, INTERTANKO, INTERCARGO and RINA, International Maritime Organization, London, December 2023.

[55] P. Kaluza, A. Kölzsch, M. T. Gastner, and B. Blasius, "The complex network of global cargo ship movements," *Journal of the Royal Society Interface*, vol. 7, no. 48, pp. 1093–1103, 2010.

[56] J. O'Callaghan. (2024) Red sea crisis: How global shipping is being rerouted out of danger. BBC Future. Accessed: 2025-04-23. [Online]. Available: https://www.bbc.com/future/article/20240119-red-sea-crisis-how-global-shipping-is-being-rerouted-out-of-danger

[57] European Transport Maps, "Roro and ferry operator map - european transport maps," 2024, accessed: 2025-04-22. [Online]. Available: https://www.europeantransportmaps.com/map/roro-ferry/operator

[58] Direct Ferries. (2024) Compare ferry routes - search all ferries. Accessed: 2025-04-23. [Online]. Available: https://www.directferries.com/routes.htm

[59] ASEAN Secretariat, "The feasibility study on the establishment of an asean roro shipping network and short sea shipping," ASEAN Secretariat, 2013, accessed: 2025-04-23. [Online]. Available: https://www.asean.org/wp-content/uploads/images/2013/economic/transport/EIJR13069_FR-Summary.pdf

[60] J. Liu, A. Meucci, Q. Liu, A. V. Babanin, D. Ierodiaconou, and I. R. Young, "The wave climate of bass strait and south-east australia," *Ocean Modelling*, vol. 172, p. 101980, 2022.

[61] WaveClimate.com. (2024) Waveclimate: Global offshore wave climate data and statistics. Accessed: 2025-04-23. [Online]. Available: http://www.waveclimate.com/

[62] NAPA Ltd., *NAPA Release 2024.2*, NAPA Ltd., 2024, Ship Design and Stability Analysis Software. [Online]. Available: https://www.napa.fi/napa-release-2024-2/

[63] V. Shigunov, O. El Moctar, H. Rathje, and A. Germanischer Lloyd, "Conditions of parametric rolling," in *Proceedings of the 10th International Conference on Stability of Ships and Ocean Vehicles*, 2009, p. 521.

A Wave Scatter Diagrams of All Studied Zones

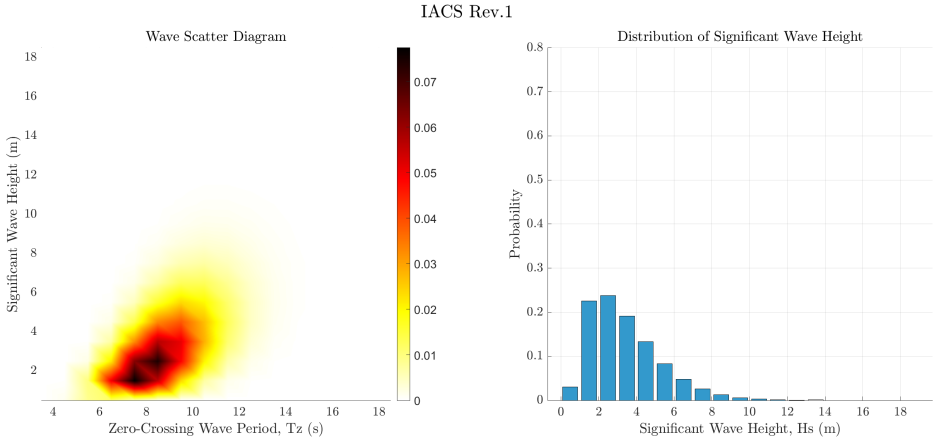

Figure A1: Wave scatter diagram and significant wave height probability for IACS Rev.1

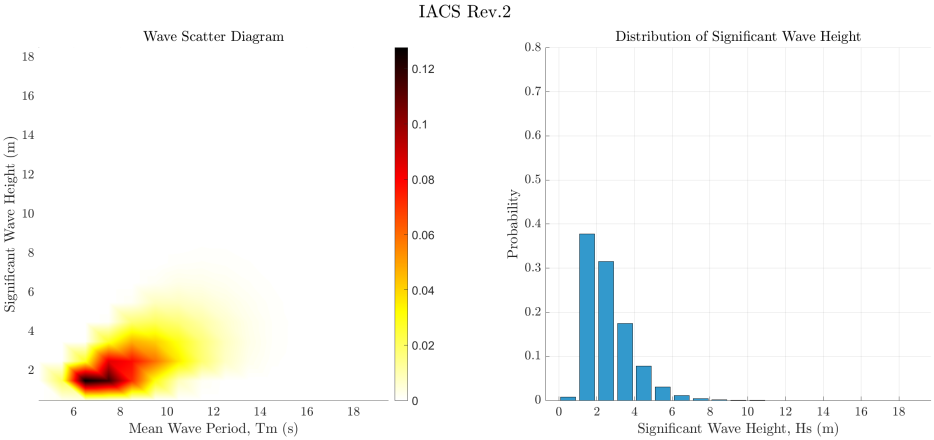

Figure A2: Wave scatter diagram and significant wave height probability for IACS Rev.2

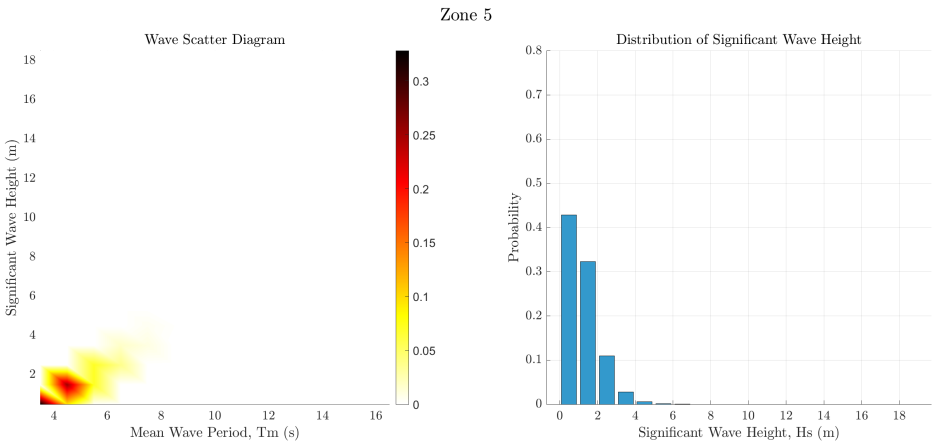

Figure A3: Wave scatter diagram and significant wave height probability for Zone 5.

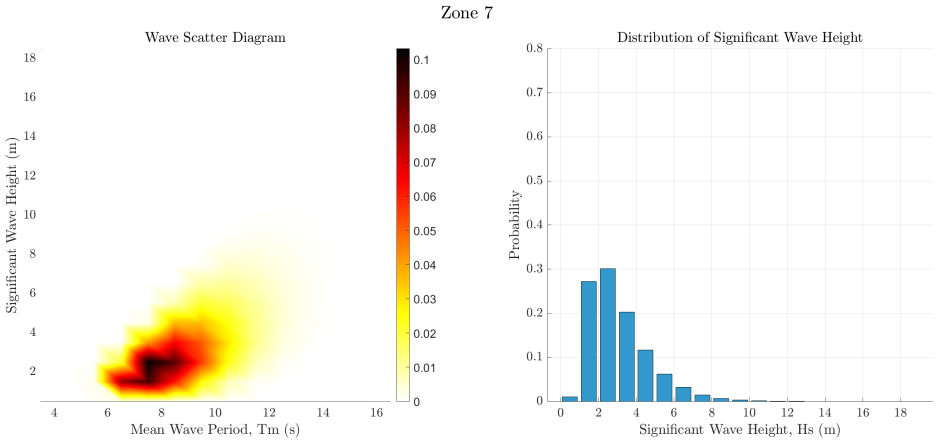

Figure A4: Wave scatter diagram and significant wave height probability for Zone 7.

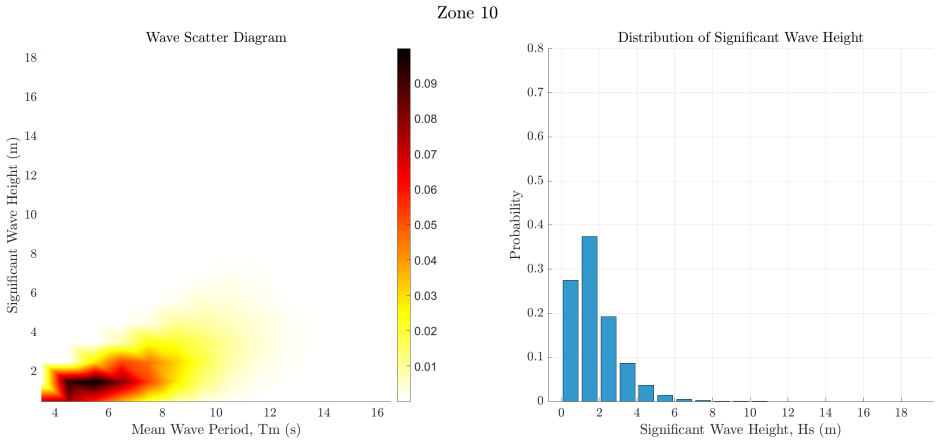

Figure A5: Wave scatter diagram and significant wave height probability for Zone 10.

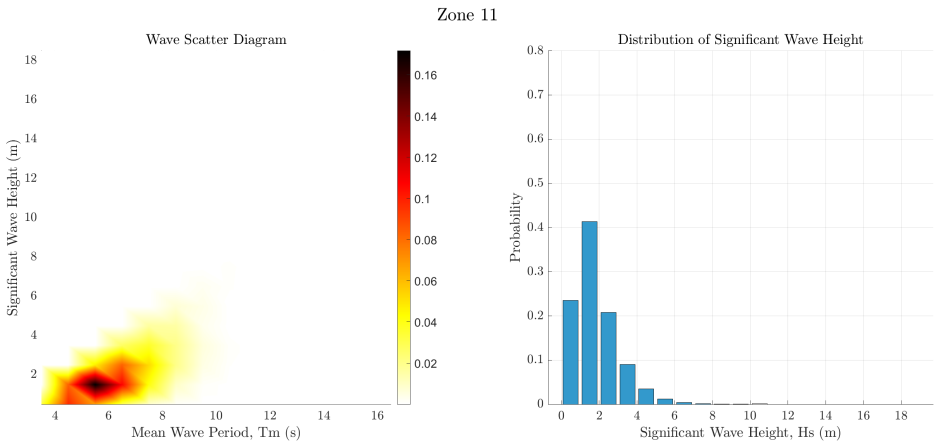

Figure A6: Wave scatter diagram and significant wave height probability for Zone 11.

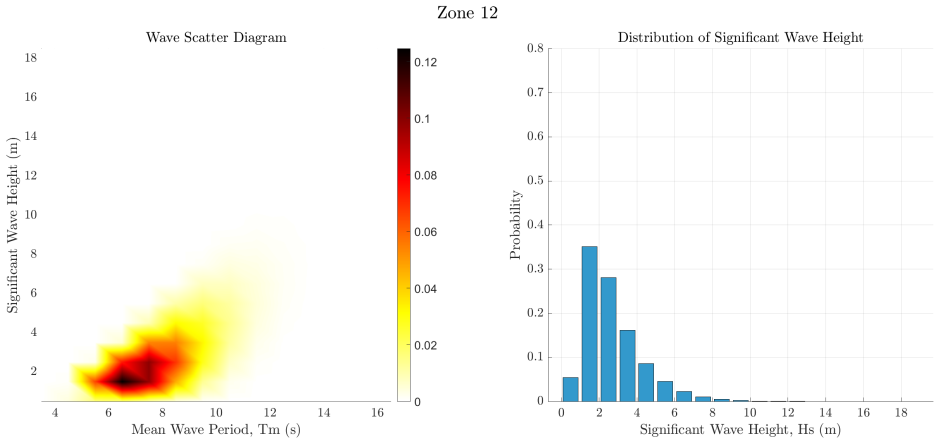

Figure A7: Wave scatter diagram and significant wave height probability for Zone 12.

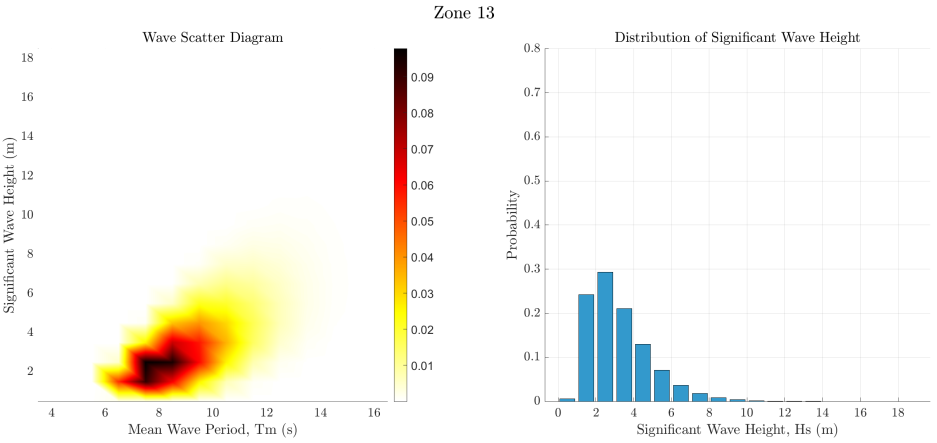

Figure A8: Wave scatter diagram and significant wave height probability for Zone 13.

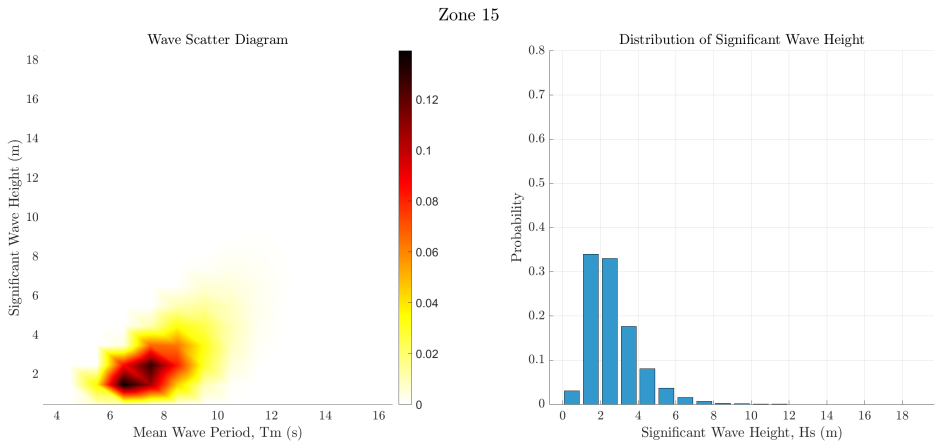

Figure A9: Wave scatter diagram and significant wave height probability for Zone 15.

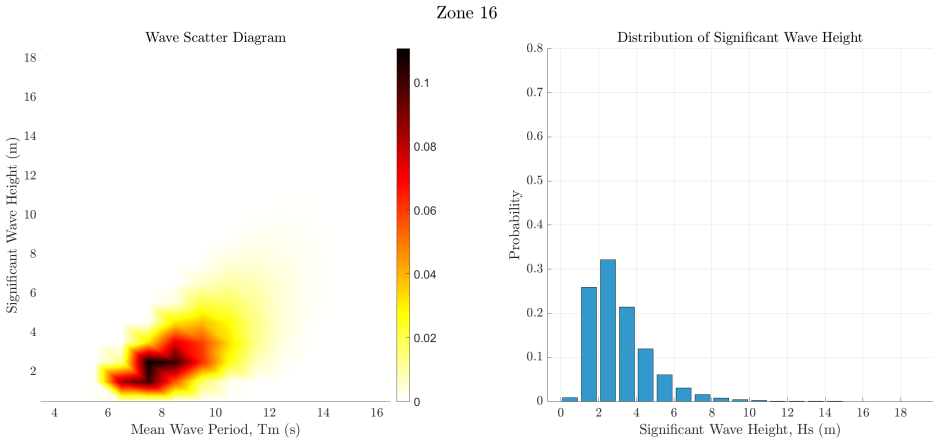

Figure A10: Wave scatter diagram and significant wave height probability for Zone 16.

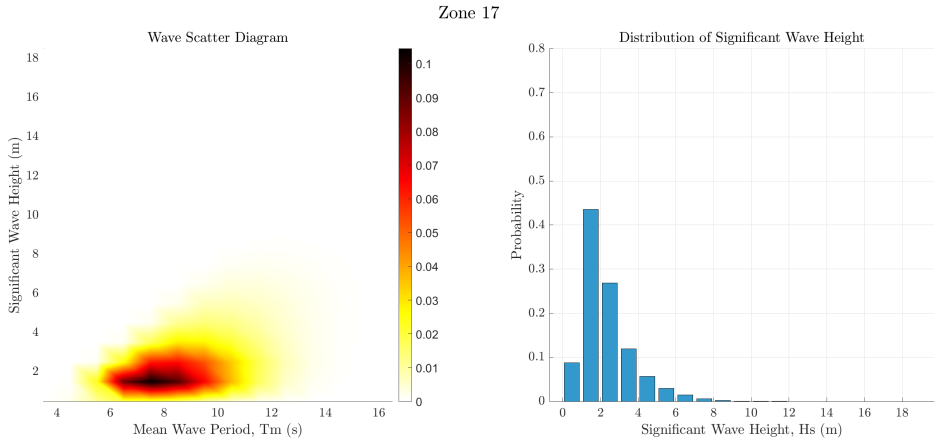

Figure A11: Wave scatter diagram and significant wave height probability for Zone 17.

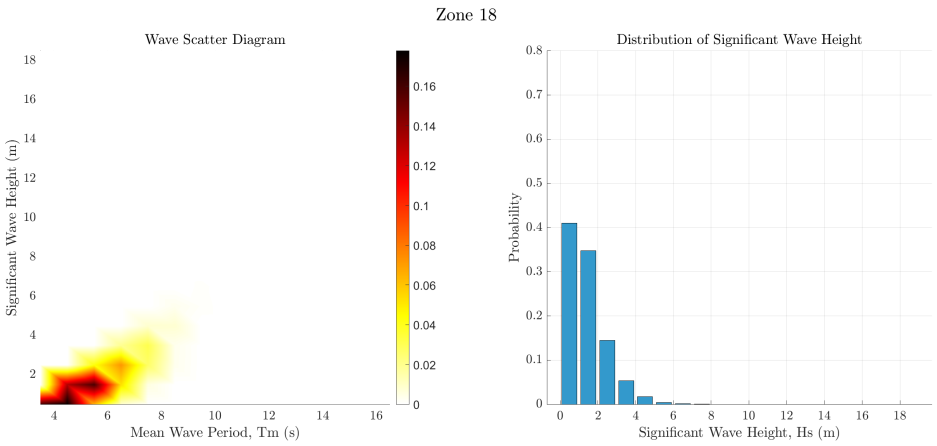

Figure A12: Wave scatter diagram and significant wave height probability for Zone 18.

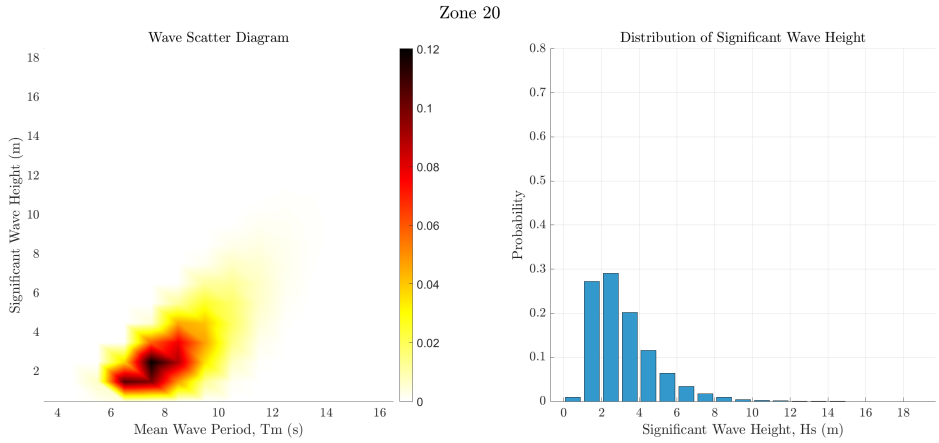

Figure A13: Wave scatter diagram and significant wave height probability for Zone 20.

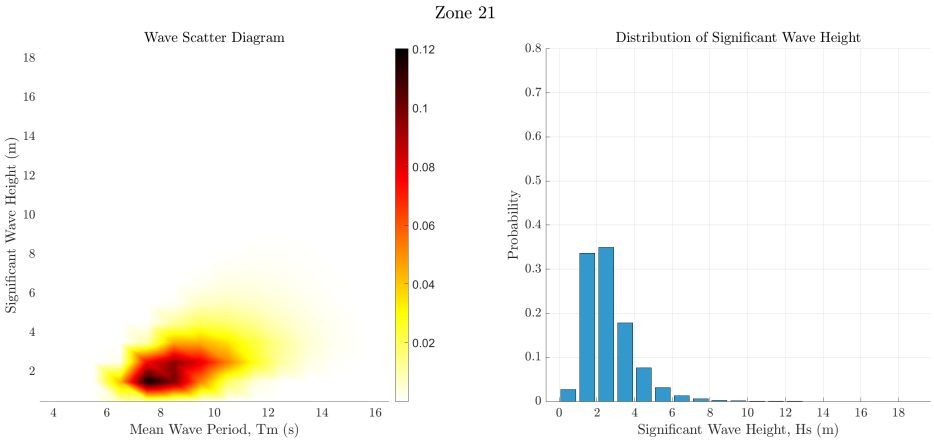

Figure A14: Wave scatter diagram and significant wave height probability for Zone 21.

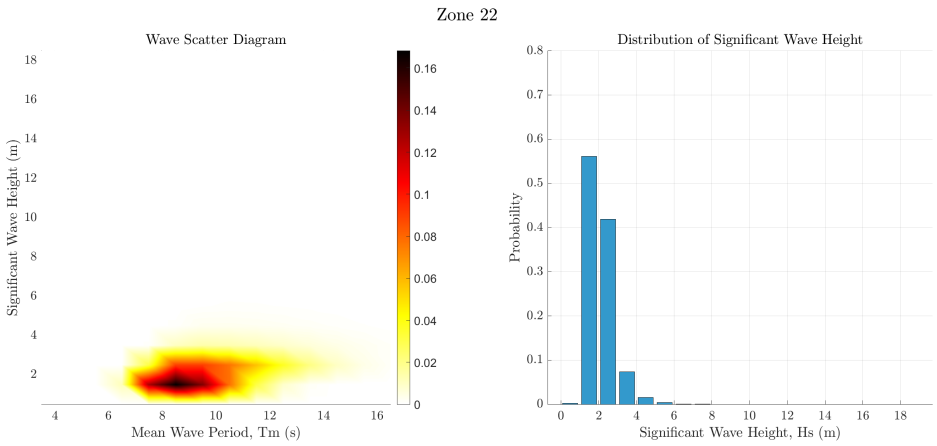

Figure A15: Wave scatter diagram and significant wave height probability for Zone 22.

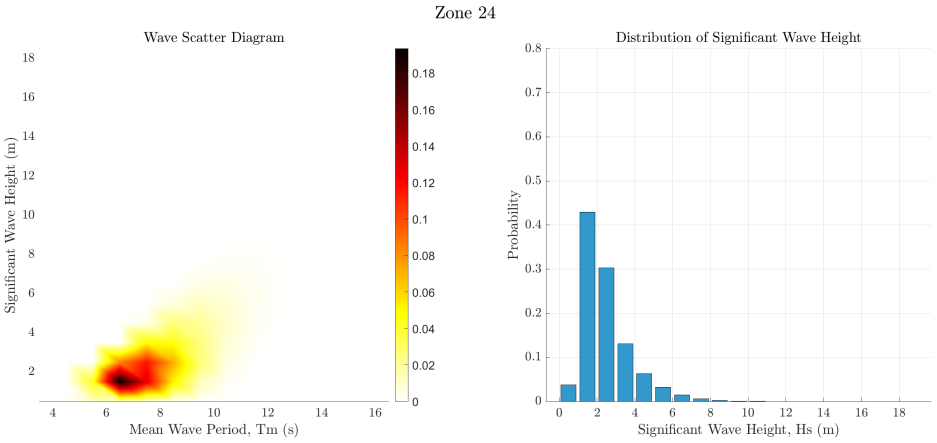

Figure A16: Wave scatter diagram and significant wave height probability for Zone 24.

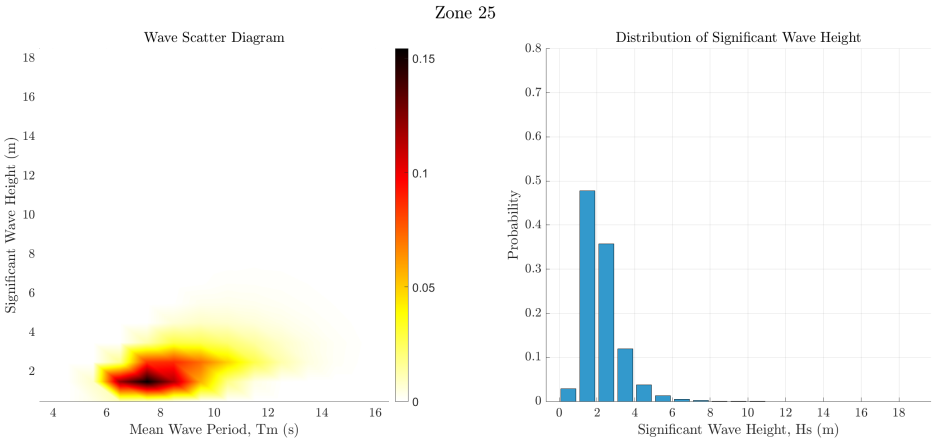

Figure A17: Wave scatter diagram and significant wave height probability for Zone 25.

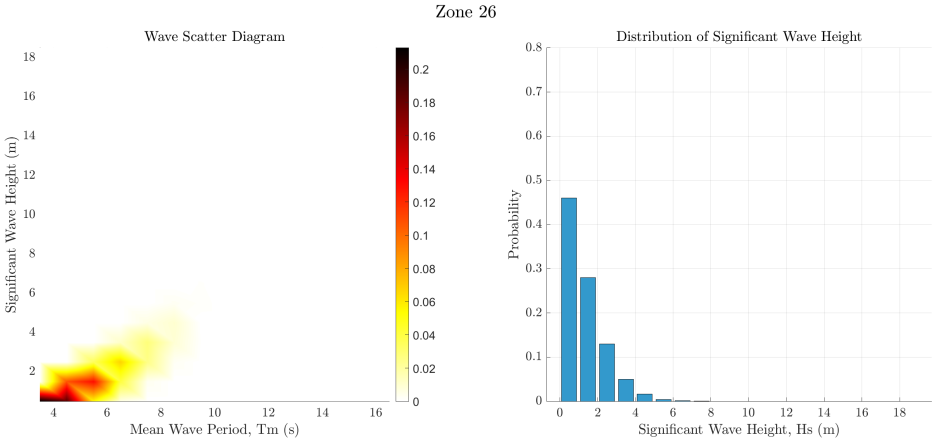

Figure A18: Wave scatter diagram and significant wave height probability for Zone 26.

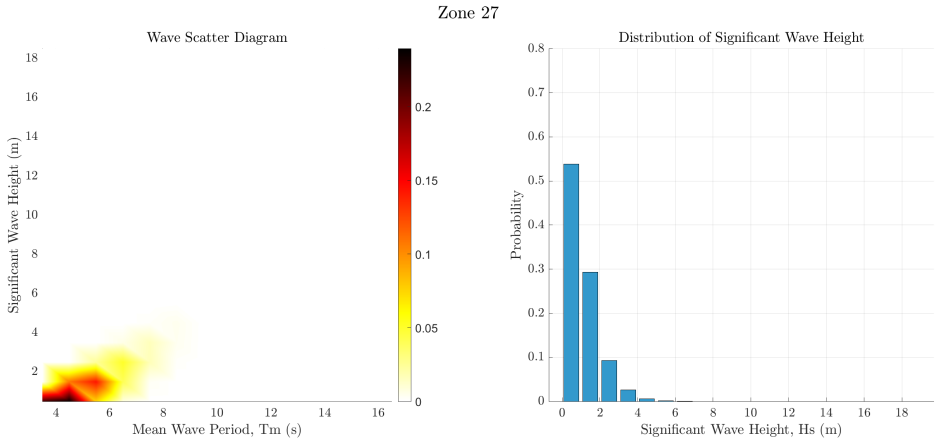

Figure A19: Wave scatter diagram and significant wave height probability for Zone 27.

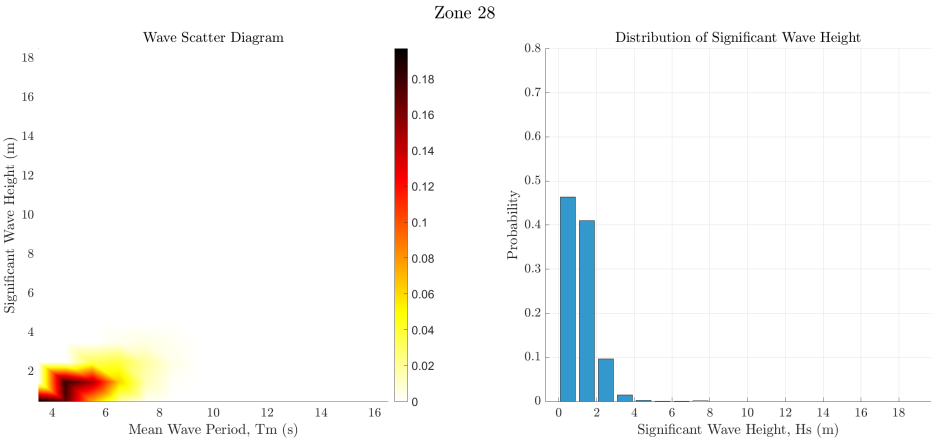

Figure A20: Wave scatter diagram and significant wave height probability for Zone 28.

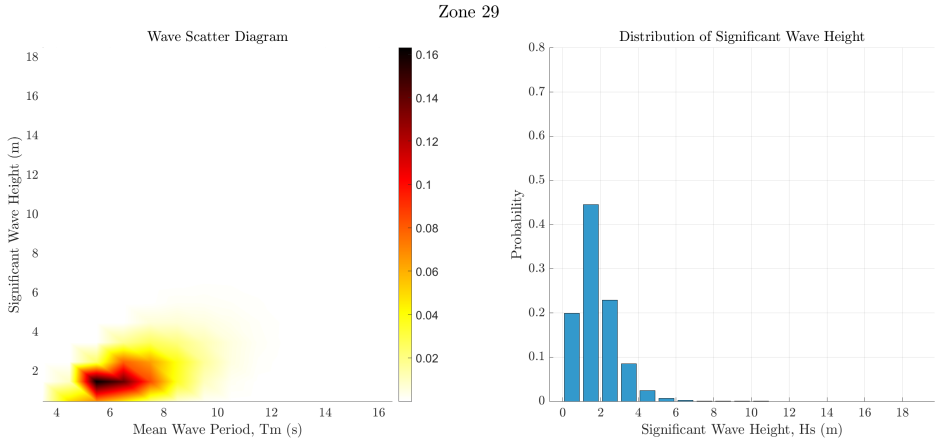

Figure A21: Wave scatter diagram and significant wave height probability for Zone 29.

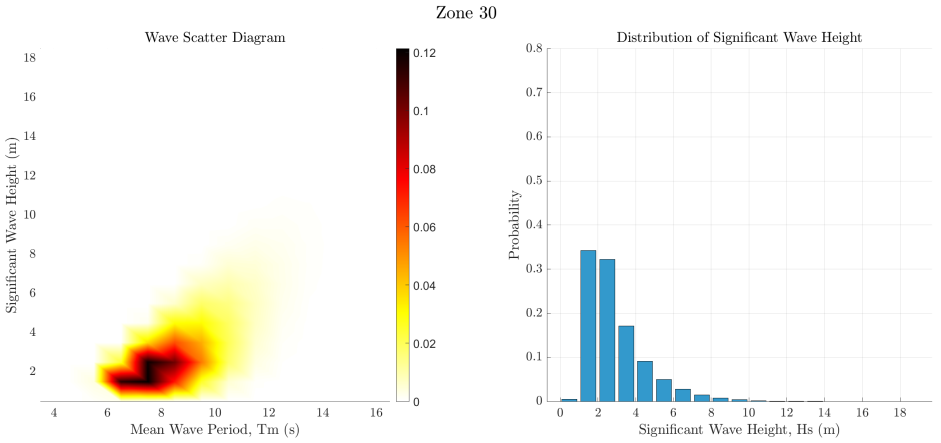

Figure A22: Wave scatter diagram and significant wave height probability for Zone 30.

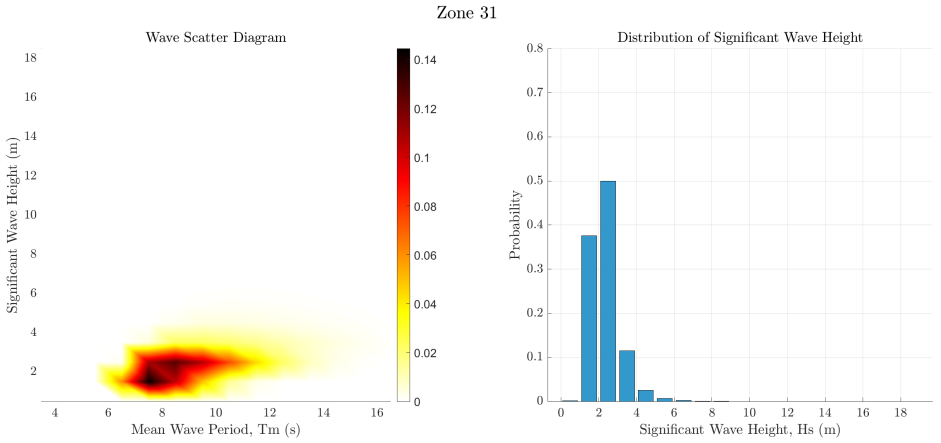

Figure A23: Wave scatter diagram and significant wave height probability for Zone 31.

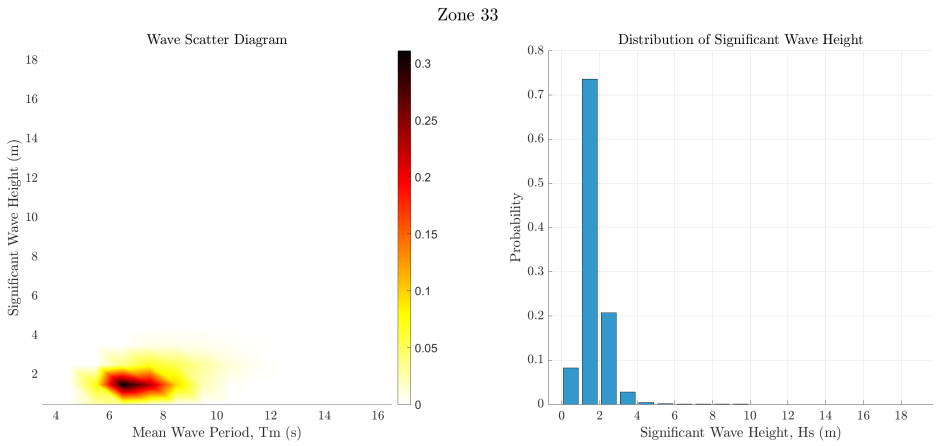

Figure A24: Wave scatter diagram and significant wave height probability for Zone 33.

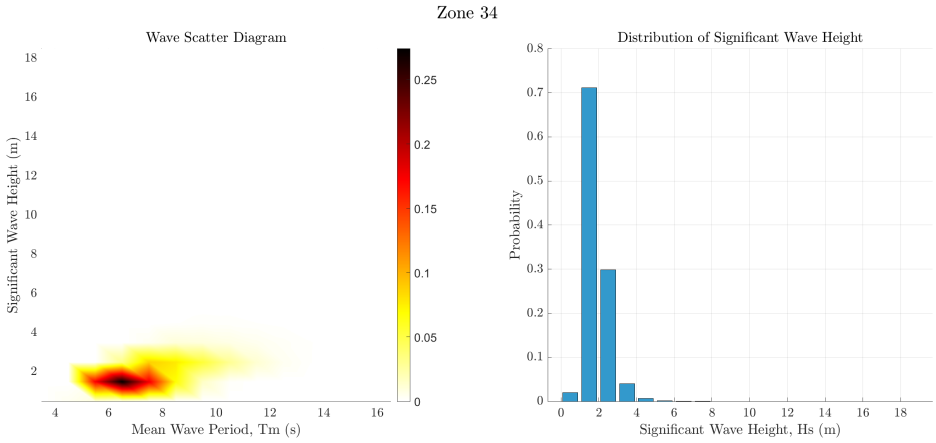

Figure A25: Wave scatter diagram and significant wave height probability for Zone 34.

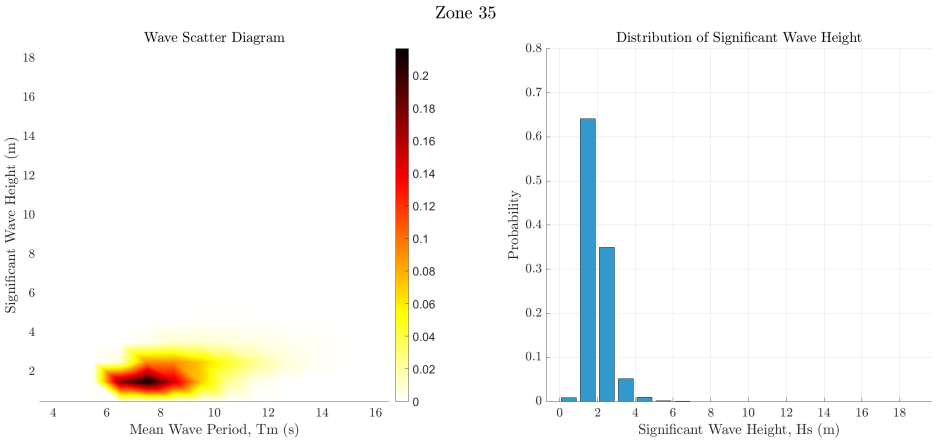

Figure A26: Wave scatter diagram and significant wave height probability for Zone 35.

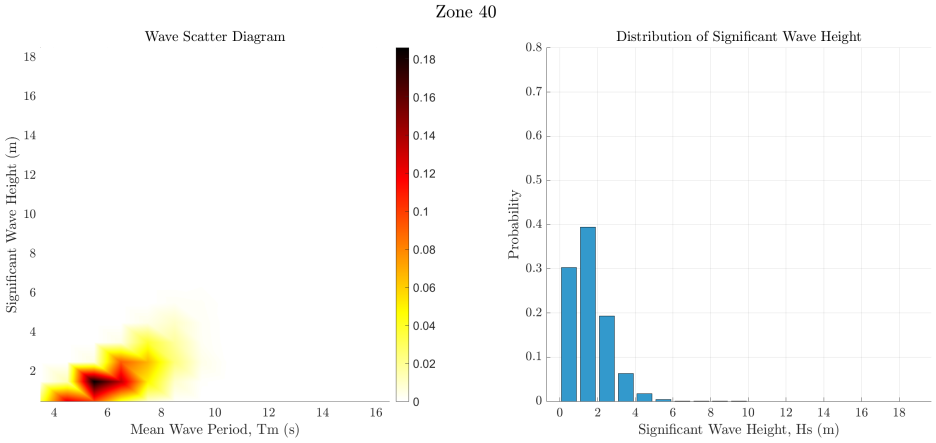

Figure A27: Wave scatter diagram and significant wave height probability for Zone 40.

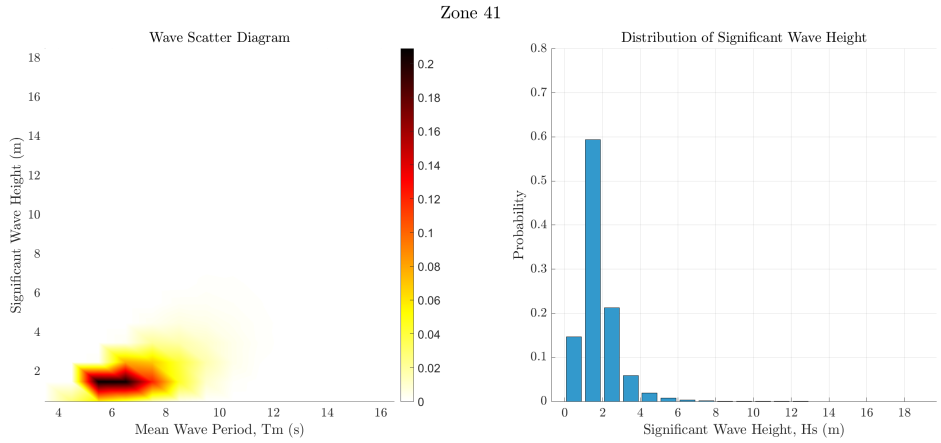

Figure A28: Wave scatter diagram and significant wave height probability for Zone 41.

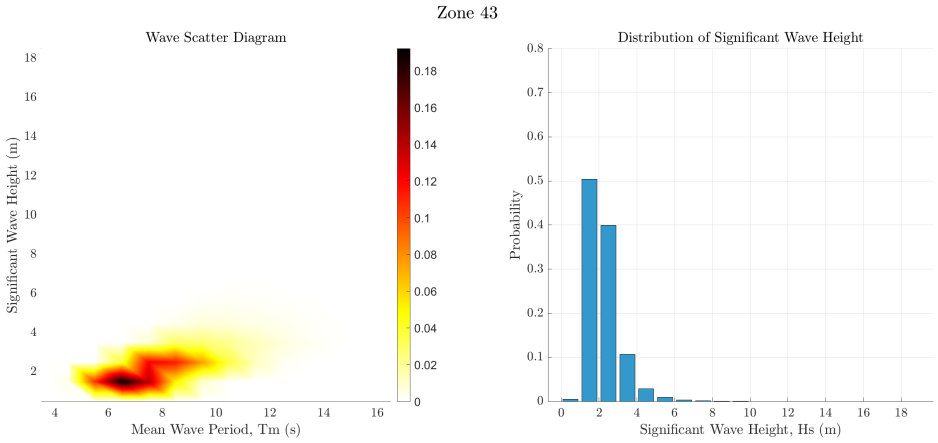

Figure A29: Wave scatter diagram and significant wave height probability for Zone 43.

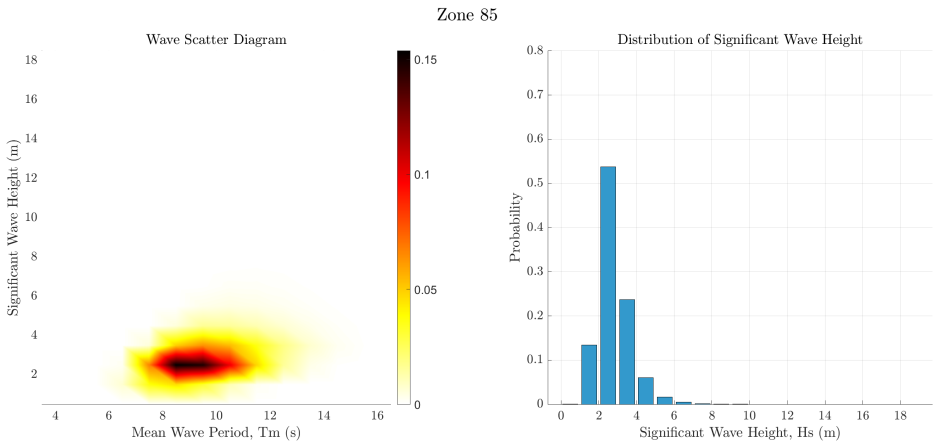

Figure A30: Wave scatter diagram and significant wave height probability for Zone 85.

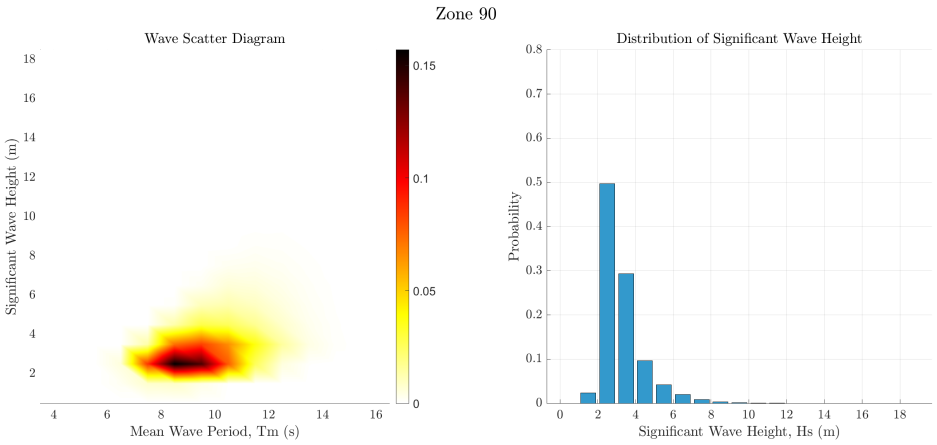

Figure A31: Wave scatter diagram and significant wave height probability for Zone 90.

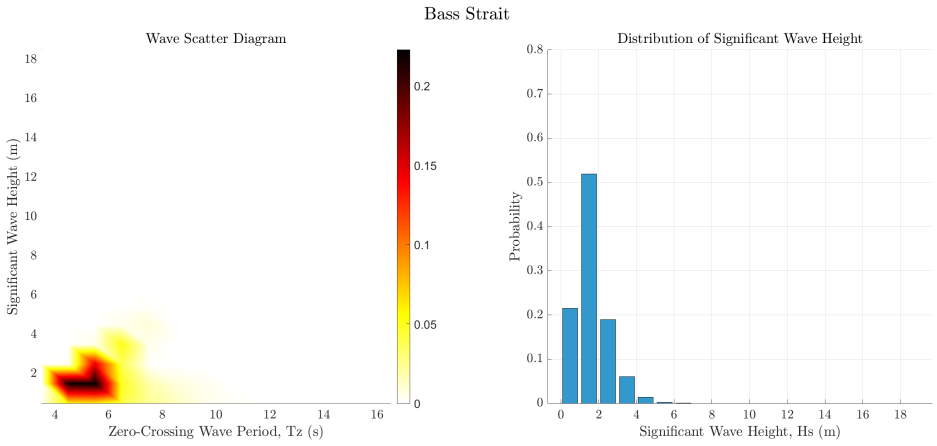

Figure A32: Wave scatter diagram and significant wave height probability for Bass Strait